

**Incorporation of Glycyl-L-Histidyl-L-lysine (GHK) with Metalized  
Halloysites for Tissue Regeneration**

By

Christopher Cameron Miller, M.S., B.S.

A Dissertation Presented in Partial Fulfillment  
of the Requirements of the Degree  
Doctor of Philosophy

COLLEGE OF APPLIED AND NATURAL SCIENCE  
LOUISIANA TECH UNIVERSITY

August 2021

LOUISIANA TECH UNIVERSITY

GRADUATE SCHOOL

June 15, 2021

Date of dissertation defense

We hereby recommend that the dissertation prepared by

**Christopher Miller**

---

entitled **Incorporation of Glycyl-L-Histidyl-L-lysine (GHK) with Metalized**

---

**Halloysites for Tissue Regeneration**

---

be accepted in partial fulfillment of the requirements for the degree of

**Doctor of Philosophy in Molecular Sciences and Nanotechnology**

---

---

Dr. David K. Mills  
Supervisor of Dissertation Research

*gergana nestorova*

---

Dr. Gergana Nestorova  
Head of Molecular Sciences and Nanotechnology

**Doctoral Committee Members:**

Dr. David K. Mills

Dr. Gergana Nestorova

Dr. Bryant Hollins

Dr. Rebecca Giorno-McConnell

Dr. Teresa Murray

**Approved:**

*Gary A. Kennedy*

---

Gary A. Kennedy  
Dean of Applied & Natural Sciences

**Approved:**

*Ramu Ramachandran*

---

Ramu Ramachandran  
Dean of the Graduate School

## Abstract

Human adipose stem cells (hASCs) provide a research tool for regenerative medicine in various capacities. There are major research needs for new therapies for bone-related diseases such as osteoporosis, osteomyelitis, and severe trauma. Human ASCs can self-renew for extended durations outside of the body and provide an ideal platform to study therapeutics for the formation of bone-specific modalities or wound healing applications.

Combining hASCs with nanomaterials is a growing area of research that requires additional studies. Halloysites (HNTs) are hollow aluminosilicate nanotubes with an exterior negative charge and a positively charged lumen. HNTs have demonstrated biocompatibility in cell and animal-based studies, with additional capabilities for vacuum loading of drugs and coating metal ions such as silver, zinc, strontium, and copper (mHNTs). Metal ions provide synergistic antimicrobial effects on prokaryotes, allowing healthy cells to form in infection risk areas. These unique properties allow a varying of methods to be developed in cell-based therapeutics at the tissue level.

The primary focus of my research is to investigate the therapeutic potential of metalized HNTs with a linked tripeptide known as GHK (glycyl-L-histidyl-L-lysine). GHK is known to be essential in the wound healing process. Ultimately, studying these interactions will lead to better bandages to be hemostatic, alleviate pain and inflammation, and cost-effectively possess antimicrobial features. Bone and wound analysis studies were conducted on hASCs after the incorporation of such nanoparticles. Results introducing GHK with metalized HNTs showed increased proliferation of hASCs, collagen production, and an increase in the genes *ki67* and *runx2*, a proliferation and bone marker, respectively. Strontium-coated HNTs increased osteochondral differentiation after analysis by phase-contrast imaging, gene expression, and unique morphological changes of hASCs exhibiting trabecular-like bone formations in culture.

Copper-coated HNTs coupled with GHK increased wound closure after artificial wound analysis, further validating gene expression and proliferation studies. Human ASCs were additionally encapsulated in alginate hydrogels with GHK and mHNTs that increased cell viability and collagen production, leading to differentiated fibroblast clusters within the hydrogel constructs. Given these results, expanding the use of mHNTs with GHK in animal wound healing studies can profoundly impact wound healing if incorporated into FDA-approved materials.

## **APPROVAL FOR SCHOLARLY DISSEMINATION**

The author grants to the Prescott Memorial Library of Louisiana Tech University the right to reproduce, by appropriate methods, upon request, any or all portions of this Dissertation. It is understood that “proper request” consists of the agreement, on the part of the requesting party, that said reproduction is for his personal use and that subsequent reproduction will not occur without written approval of the author of this Dissertation. Further, any portions of the Dissertation used in books, papers, and other works must be appropriately referenced to this Dissertation.

Finally, the author of this Dissertation reserves the right to publish freely, in the literature, at any time, any or all portions of this Dissertation.

Author \_\_\_\_\_

Date \_\_\_\_\_

## **DEDICATION**

This dissertation is dedicated to my late grandfather, Ellis Killgore, and my late great-uncle, Charles Killgore. Both men were former professors and scientists at Louisiana Tech University. Their memory, sacrifice, and love for science motivates and inspires me each day.

## TABLE OF CONTENTS

ABSTRACT.....	iii
APPROVAL FOR SCHOLARLY DISSEMINATION.....	iv
DEDICATION.....	v
LIST OF FIGURES .....	x
LIST OF TABLES.....	xvii
ACKNOWLEDGMENTS.....	xviii
CHAPTER 1 INTRODUCTION AND BACKGROUND.....	1
1.1 Regenerative Medicine.....	1
1.2 Human Adipose Stem cells for Tissue Regeneration.....	2
1.3 Biomaterials for Tissue Regeneration.....	4
1.4 Wound Healing Fundamentals.....	9
1.5 Tripeptides for Wound Healing Applications.....	11
1.6 Synthesizing Tripeptides.....	13
CHAPTER 2 WOUND HEALING, BONE REPAIR, AND REGENERATION.....	15
2.1 Improving Current Healing Capabilities.....	15
2.2 Bone Formation Processes.....	18
2.3 BMP Signaling Pathway.....	21
CHAPTER 3 Determining Expression of GHK and mHNTs with hASCs.....	26
3.1 Introduction.....	26
3.2 Materials & Methods.....	28
3.2.1 Particle Confirmation.....	28
3.2.1.1 Mass Spectrometry(MS).....	28
3.2.1.2 High performance Liquid Chromatography(HPLC).....	28
3.2.1.3 Scanning Electron Microscope(SEM).....	28
3.2.1.4 Energy Dispersion Spectroscopy(EDS).....	29

3.2.2 Generation of nanocomposites.....	28
3.2.3 Cell Culture Media.....	30
3.2.4 Cell Culture Growth.....	30
3.2.5 Immunofluorescent Live/Dead Staining.....	30
3.2.6 Gene Expression Analysis.....	31
3.2.6.1 RNA Extraction.....	31
3.2.6.2 RNA Quantification.....	32
3.2.6.3 cDNA Synthesis.....	32
3.2.6.4 RT-qPCR.....	32
3.2.7 Statistical Analysis.....	34
3.3 Results.....	34
3.3.1 Mass Spectrometry.....	34
3.3.2 HPLC.....	36
3.3.3 SEM and EDS.....	37
3.3.4 Live/Dead Analysis.....	47
3.3.5 Gene Expression.....	50
3.4 Discussion and Conclusion.....	58
3.4.1 Particle Formation and Analysis.....	58
3.4.2 Live/Dead Staining.....	59
3.4.3 Gene Expression.....	60
3.5 Future Studies.....	62
CHAPTER 4 DETERMINING MIGRATORY PATTERNS AND ARTIFICIAL WOUND ANALYSIS.....	64
4.1 Introduction.....	64
4.2 Materials and methods.....	66
4.2.1 Immunofluorescent Live/Dead Staining.....	66
4.2.2 Alizarin Red Stain.....	66
4.2.3 Scratch Assay.....	67
4.2.4 Proliferation Assay .....	67
4.2.5 Migratory assay.....	67

4.2.6 Picrosirius Red Stain.....	68
4.2.7 Antibacterial Testing.....	68
4.2.7.1 Muller-Hinton Broth.....	69
4.3 Results.....	69
4.3.1 Live/Dead SrHNTs.....	70
4.3.2 Alizarin Red Staining.....	72
4.3.3 Artificial Wound Closure.....	74
4.3.4 Proliferation Assay.....	75
4.3.5 Migratory Pattern Assay.....	77
4.3.6 Picrosirius Red Staining.....	77
4.3.7 Antibacterial Testing.....	79
4.4 Discussion and Conclusion.....	81
4.4.1 Live/Dead Assay.....	81
4.4.2 Alizarin Red Staining.....	81
4.4.3 Scratch Assay.....	82
4.4.4 Proliferation Assay.....	82
4.4.5 Cell Migration Pattern Assay.....	83
4.4.6 Picrosirius Red.....	83
4.4.7 Antibacterial Testing.....	84
4.5 Future Studies.....	85
CHAPTER 5 INVESTIGATING 3D MATRIX FOR TISSUE FORMATION.....	87
5.1 Introduction .....	87
5.2 Materials and Methods .....	88
5.2.1 Cell Microencapsulation.....	88
5.2.2 4K high resolution digital Imaging.....	89
5.2.3 Immunofluorescent live/dead staining.....	89
5.2.4 Picrosirius Red staining.....	89
5.3 Results.....	90
5.3.1 Hydrogel Characterization.....	90
5.3.2 Live/Dead Assay.....	93

5.3.3 Picrosirius Red Staining.....	100
5.4 Discussion and Conclusion.....	102
5.4.1 4K high resolution digital imaging.....	102
5.4.2 Live/Dead.....	103
5.4.3 Picrosirius Red Staining.....	103
5.5 Future Studies.....	104
BIBLIOGRAPHY.....	107

## List of Figures

- Figure 1-1.** FE-SEM Image of unmodified HNTs (Left), showing the structure of HNT (center) and a schematic Illustration of the chemical structure of HNTs (Right).....5
- Figure 1-2.** Graphic Illustration showing Cu deposition on the HNT surface and attachment of the GHK peptide.....6
- Figure 1-3.** Elasticities of different cell types, synthetic polymers, and a natural polymer.....8
- Figure 2-1.** Figure 2-1. A.) A hemostatic bandage incorporated with metalized halloysites and GHK tripeptides for wound healing applications. The bandage lines the dermal surface in open wounds, and multiple layers can be created to enhance hemostasis, pathogen resistance, and promote tissue formation. B.) Proposed GHK-Cu-HNT complex to incorporate into blow-spun or electro-spun fibers. C.) Blow-spun fibers created and analyzed by SEM (right) and a prototype bandage constructed (left).....16
- Figure 2-2.** A.) The proposed bandage solution would be used with FDA approved materials, metalized HNTs, tripeptides, and drastically improve upon leading competitors. B.) Chitosan and PLA that can be combined with metalized HNTs in blow-spinning methods. C.) PLA printed textiles can be infused with metalized HNTs, or drugs, and they can provide structural support in tissue damaged areas. ....18
- Figure 2-3.** The basic features of osteoblast organization, an osteon. During bone mineral transport, the process of mineral deposition produces acid. Exclusively during mineral transport, osteoblasts also transport hydroxyapatite-binding fluorescent molecules..... 21
- Figure 2-4.** Chemical structure of a BMP molecule before secretion out of the cell.....22
- Figure 2-5.** Schematic of the mechanistic process of the signaling cascade for BMP and its associated receptor..... 24
- Figure 3-1.** Mass spectrum of GHK. The parent peak to the far right indicates particle formation at a molecular weight of 341 g/mol.....34

- Figure 3-2.** Mass spectrum of GHK-Palmitic Acid. The parent peak to the far right indicates particle formation of 607 g/mol.....35
- Figure 3-3.** Mass spectrum of GHK-Steric Acid. The parent peak to the far right indicates particle formation at 579 g/mol.....35
- Figure 3-4.** High performance liquid chromatography spectrum of GHK giving a 98.74% purity level.....36
- Figure 3-5.** High performance liquid chromatography spectrum of GHK- palmitic acid giving a 98.0% purity level.....36
- Figure 3-6.** High performance liquid chromatography spectrum of GHK- Steric acid giving a 99.45% purity level.....37
- Figure 3-7.** Scanning electron microscopy of GHK-Stearic acid at 400x and coated with silver at 5 nanometer thickness. Congregated flaky layers can be seen throughout the image.....38
- Figure 3-8.** Scanning electron microscopy of GHKCuhNTs at 400x. The particles tend to clump together through charged interactions.....39
- Figure 3-9.** Scanning electron microscopy of GHK-palmitic acid at x100k and coated with silver at 5 nanometer thickness. The image contrast was still blurred after the coating process but spherical masses can be seen.....39
- Figure 3-10.** Scanning electron microscopy of GHK-stearic acid at x110k and coated with silver at 5 nanometer thickness. The image contrast was still blurred after the coating process but spherical masses can be seen.....40
- Figure 3-11.** Scanning electron microscopy of GHK at x100k and coated with silver at 5 nanometer thickness. The images contrast was still blurred after the coating process but spherical masses can be seen.....40
- Figure 3-12.** Scanning electron microscopy of GHK at 8000x and coated with silver at 5 nanometer thickness. Spiky projections were visualized after the coating process, suggesting GHK architecture was distorted.....41
- Figure 3-13.** Scanning electron microscopy of CuHNTs at x40k. Cylindrical nanoparticles were visualized throughout the sample.....41
- Figure 3-14.** Scanning electron microscopy of GHKCuhNTs at x80k. Cylindrical nanoparticles are visualized and what appears to be GHK covalently attached (indicated by arrow).....42

<b>Figure 3-15.</b> Scanning electron microscopy of GHKPCuHNTs at x80k. The blurred image cannot confirm the attachment of GHK with the CuHNTs.....	42
<b>Figure 3-16.</b> Electron dispersive X-ray spectroscopy confirming the presence of carbon and oxygen used within polymer tape of the EDS system.....	43
<b>Figure 3-17.</b> Electron dispersive X-ray spectroscopy confirming the presence of essential elements for amine and carboxyl groups for GHK. Slight peaks for fluorine were recorded.....	43
<b>Figure 3-18.</b> Electron dispersive X-ray spectroscopy confirming the presence of essential elements for amine and carboxyl groups for GHK. Slight peaks for chlorine were recorded.....	44
<b>Figure 3-19.</b> Electron dispersive X-ray spectroscopy confirming the presence of essential elements for amine and carboxyl groups for GHK. Slight peaks for fluorine were recorded.....	44
<b>Figure 3-20.</b> Electron dispersive X-ray spectroscopy confirming the presence of essential elements for amine and carboxyl groups along with copper and aluminosilicates in GHK/CuHNTs.....	45
<b>Figure 3-21.</b> Electron dispersive X-ray spectroscopy colored micrograph of CuHNTs. Carbon and oxygen are picked up from the polymer-based tape used within the EDS system.....	45
<b>Figure 3-22.</b> Electron dispersive X-ray spectroscopy confirming the presence of essential elements in CuHNTs.....	46
<b>Figure 3-23.</b> Immunofluorescent overlay images of GHK, GHK-P, GHK-S, and control group after 7 days in culture. Live nuclei are stained blue. Dead cell debris is stained green; n=3.....	48
<b>Figure 3-24.</b> Immunofluorescent overlay images of GHK, GHK-P, GHK-S, and control group after 14 days in culture. Live nuclei are stained blue. Dead cell debris is stained green; n=3.....	48
<b>Figure 3-25.</b> Immunofluorescent overlay images of GHK, GHK-P, GHK-S, and control group after 21 days in culture. Live nuclei are stained blue. Dead cell debris is stained green; n=3.....	49

**Figure 3-26.** Immunofluorescent overlay images of GHK, GHK-P, GHK-S, and control group after 28 days in culture. Live nuclei are stained blue. Dead cell debris is stained green; n=3.....49

**Figure 3-27.** Cell viability observed over the course of 28 days after nanomaterials were incorporated at 50 micromolar concentrations; n=3. Images were taken from 3 separate plates within the same region.....50

**Figure 3-28.** Phase contrast image of hASCs after 7 days in culture exposed to SrHNTs. Cell have attached and are migrating across the culture surface (note the long filopodia, red stars) Clusters of cells (red arrows) were also observed.....50

**Figure 3-29.** Increased expression of Ki67 after SrHNT Exposure for 7 days. Expression was normalized to *gapdh*.  $P < .05^*$ ; n=3. Error bars represent  $\pm$  standard error. NC denotes the negative control.....51

**Figure 3-30.** Increased expression of *Ki67* and *runx2* after SrHNT Exposure for 14 days. Expression was normalized to *gapdh*.  $P < .05^*$ ; n=3. Error bars represent  $\pm$  standard error. NC denotes the negative control.....52

**Figure 3-31.** No significant difference in *osteopontin* were observed after SrHNT exposure for 14 days. Expression was normalized to *gapdh*.  $P < .05^*$ ; n=3. Error bars represent  $\pm$  standard error. NC denotes the negative control.....52

**Figure 3-32.** Increased expression of *Ki67* after GHKCuHNT Exposure for 24 hours. Expression was normalized to *gapdh*.  $P < .05^*$ ; n=3. Error bars represent  $\pm$  standard error. NC denotes the negative control.....53

**Figure 3-33.** There was no significant impact on *runx2* after GHKCuHNT exposure for 24 hours. Expression was normalized to *gapdh*.  $P < .05^*$ ; n=3. Error bars represent  $\pm$  standard error. NC denotes the negative control.....53

**Figure 3-34.** An increased expression of *ki67* and decreased expression of *runx2* was observed after GHK exposure at 50 micromolar for 7 days. Expression was normalized to *gapdh*.  $P < 0.05^*$ ; n=3. Error bars represent  $\pm$  standard error. NC denotes the negative control.....54

**Figure 3-35.** Increased expression of *ki67* after GHK exposure at 50 micromolar was observed for 14 days.  $P < 0.05^*$ ; n=3. Expression was normalized to *gapdh*. Error bars represent  $\pm$  standard error. NC denotes the negative control.....54

**Figure 3-36.** Increased expression of *ki67* after GHK, GHKP, and GHKS exposure at 50 micromolar for 14 days.  $P < 0.05^*$ ; n=3. Expression was normalized to *gapdh*. Error bars represent  $\pm$  standard error. NC denotes the negative control.....55

**Figure 3-37.** A. decreased expression of *runx2* was observed after GHK, GHKP, GHKS exposure at 50 micromolar for 14 days.  $P < 0.05^*$ ;  $n=3$ . Expression was normalized to *gapdh*. Error bars represent  $\pm$  standard error. NC denotes the negative control.....55

**Figure 3-38.** Decreased expression of *runx2* after exposure to GHKS-CuHNT at 50 micromolar for 24 hours.  $P < 0.05^*$ ;  $n=3$ . Expression was normalized to *gapdh*. NC denotes the negative control.....56

**Figure 3-39.** Increased expression of *ki67* after exposure to GHKS-CuHNT at 50 micromolar.  $P < 0.05^*$ ;  $n=3$ . Expression was normalized to *gapdh*. NC denotes the negative control.....56

**Figure 3-40.** Increase in expression of *ki67* after exposure to GHKP-CuHNT at 50 micromolar.  $P < 0.05^*$ ;  $n=3$ . Expression was normalized to *gapdh*. NC denotes the negative control.....57

**Figure 3-41.** Increase in expression of *ki67* after exposure to GHKP-CuHNT at 50 micromolar.  $P < 0.05^*$ ;  $n=3$ . Expression was normalized to *gapdh*. NC denotes the negative control.....57

**Figure 4-1.** Left - 7 days after SrHNTs were added to hASCs at a 50 micromolar concentration. Live cells stained in blue. Dead cells are in green. Note. That there was some absorption of the dyes by the HNTs. 10x magnification. Right – cell clustering was observed and apparent internalization of the SrHNTs (dark colored areas) (phase contrast).....70

**Figure 4-2.** Left - Live dead stain 14 days after SrHNTs to hASCs were added at 50 micromolar concentration. 10x magnification for immunofluorescence and 4x bright field microscopy images display. SrHNTs were starting to be compacted denoted by the arrows. Live cells are stained in blue. Dead cells were stained green. Similar absorption of the dyes by HNTs was observed. Right – Cluster of cells and HNTs organized into a ‘trabecular like pattern (phase contrast).....70

**Figure 4-3.** left - Live dead stain 28 days after SrHNTs to hASCs were added at 50 micromolar concentration. 4x magnification for immunofluorescence and bright field microscopy. Live cells stained in blue. Dead cells in green. Some absorption of dyes by halloysite was observed. Clusters of SrHNTs can be seen and are denoted by arrows. Right – Trabecular like structures are more apparent (phase contrast).....71

**Figure 4-4.** Cell migration was observed over time with SrHNTs with hASCs after 28 days. The cell pattern manifested as trabecular-like structures (bottom left). Live cells are shown in blue. Dead cells are shown in green. Cell structures can be seen by the naked eye (top right).....71

**Figure 4-5.** Alizarin Red staining of each well after days 7, 14, 21, and 28 days exposed to GHKCuHNT, CuHNT, and SrHNT. A negative and positive control were used for comparison.....72

**Figure 4-6.** Scratch assay of controls compared to GHK from time 0 hour to 24 hours. A statistical analysis was carried out with a one-way ANOVA followed by Tukey post-hoc analysis.....74

**Figure 4-7.** Tripeptides incorporated at 50 micromolar concentrations. N=3 for all samples; P < 0.05\*; P < 0.01 \*\*; statistical analysis was carried out using a one-way ANOVA followed by Tukey post-hoc. NC denotes negative control and PC a positive control for comparison.....76

**Figure 4-8.** Proliferating hASCs over 24, 48, and 72 hours. 10, 20, 30, and 40 micromolar concentrations were used for GHK, GHKP, and GHKS. Grey bars indicate negative controls. Orange bars represent positive controls. N=3 for all samples; P < 0.05\*; statistical analysis was carried out with a one-way ANOVA followed by Tukey post-hoc.....76

**Figure 4-9.** Migratory assay measured after 24 hours. Nanoparticles were tested as a chemoattractant for cell migration through an 8-micron sized pored chamber. N=3 for all samples; P < 0.05\*; P < 0.01 \*\*; statistical analysis was carried out with a one-way ANOVA followed by Tukey post-hoc. Fluorescent intensity at 580, emission at 620.....77

**Figure 4-10.** Picrosirius red stain of hASCs microencapsulated at  $8.0 \times 10^8$  and grown over 28 days. Cell clusters formed and large deposits of collagen were distributed throughout the culture plates. Collagen fibers are stained in red. Control groups represented tissue culture plates that did not have nanoparticles incorporated.....78

**Figure 4-11.** Percent coverage of Picrosirius Red stain analyzed by ImageJ software. N=3 for all samples; P < 0.01 \*\*; statistical analysis was carried out with a one-way ANOVA followed by Tukey post-hoc. Error bars represent  $\pm$  standard error.....79

**Figure 4-12** CuHNTs and tripeptides incorporated at 500 micromolar in Mueller-Hinton broth for 72 hours with *S. aureus*. Optical density readings were taken at 0, 24, 48, and 72 hours. Optical density was taken at 630nm wavelength. Error bars represent  $\pm$  standard deviation (n=3).....80

**Figure 4-13.** CuHNTs and tripeptides incorporated at 500 micromolar in Mueller-Hinton broth for 72 hours with *E. coli*. Optical density readings were taken at 0, 24, 48, and 72 hours. Optical density was taken at 630nm wavelength. Error bars represent  $\pm$  standard deviation (n=3).....80

- Figure 4-14.** GPower calculations based off a one-way ANOVA for ethical use of nanoparticles combined into FDA approved materials.....86
- Figure 5-1.** (A) color brightfield of hydrogels approximately five millimeters in size at 20x after 24 hours. Pink color in part due to absorbed media. (B) 100x magnification of hydrogel (C) 500x magnification displaying crosslinking connections within hydrogel construct.....91
- Figure 5-2.** 2500X magnification displaying pores and crosslinking. The arrow indicates micropores. A 7000 VHX Keyence digital microscope was used to focus on the micropores and crosslinking of alginate and calcium.....92
- Figure 5-3.** Topography of hydrogels displaying valleys and peaks. 3D images were z-stacked using a 7000 VHX Keyence digital microscope. The color bar indicates the uneven surface and the presence of crosslinking over the surface.....92
- Figure 5-4.** Live dead Stain of microencapsulated hASCs over the course of 7 days. Live cells are stained blue. Dead cells are stained orange/red. Large cell clusters formed within the hydrogel system with no compromise in cell viability. The reading was performed on a Cytation 5 plate reader.....93
- Figure 5-5.** Live dead Stain of microencapsulated hASCs over the course of 14 days. Live cells are stained blue. Dead cells are stained orange/red. Large cell clusters formed within the hydrogel system with no compromise in cell viability. The reading was performed on a Cytation 5 plate reader.....95
- Figure 5-6.** Live dead Stain of microencapsulated hASCs over the course of 21 days. Live cells are stained blue. Dead cells are stained orange/red. Large cell clusters formed within the hydrogel system with no compromise in cell viability. The reading was performed on a Cytation 5 plate reader.....97
- Figure 5-7.** Live dead Stain of microencapsulated hASCs over the course of 28 days. Live cells are stained blue. Dead cells are stained orange/red. Large cell clusters formed within the hydrogel system with no compromise in cell viability. The reading was performed on a Cytation 5 plate reader.....99
- Figure 5-8.** Picosirius red stain of hASCs microencapsulated at  $8.0 \times 10^8$  and grown over 28 days. Cell clusters are formed and large deposits of collagen are distributed throughout the hydrogels and are stained in red.....102
- Figure 5-9.** Percent coverage of Picosirius Red stain analyzed by ImageJ software. N=3 for all samples;  $P < 0.05^*$ ;  $P < 0.01^{**}$ ; statistical analysis was carried out with a one-way ANOVA followed by Tukey post-hoc. NC denotes the negative control.....103

## List of Tables

<b><u>Table 3-1.</u></b> Oligonucleotide primers used in RT-PCR analysis.....	33
<b><u>Table 3-2.</u></b> Purity levels of GHK, GHK-palmitic acid, and GHK-steric acid after HPLC.....	35
<b><u>Table 3-3.</u></b> Elemental analysis confriming the presence of Carbon, oxygen, and nitrogen within GHK, GHK-Palmitic acid, and GHK-Stearic acid. Mass percentages and atom percentages are also given for each tripeptide. Larger amounts of Carbon are anticipated for GHKP and GHKS due to the extended fatty acid of palmitic acid and stearic acid conjugated to GHK, respectfully.....	46
<b><u>Table 4-1.</u></b> Wound closure area percentage after 24 hours. GHK, GHKP, and GHK-CuHNTs showed a significant increase in wound closure percentage using the wound analysis plugin for the ImageJ software.....	75

## **ACKNOWLEDGMENTS**

This work and dissertation is only possible because of the mentorship and encouragement of my advisor Dr. David K. Mills. I would also extend my gratitude to the members of my committee and lab mates who helped make this journey possible.

Thank you all so much. You all will live long in my mind.

## **CHAPTER 1**

### **INTRODUCTION AND BACKGROUND**

#### **1.1 Regenerative Medicine**

The ongoing need to standardize tissue regeneration capabilities is a pressing issue. According to Col. Brian Eastridge of the US Army Institute for Surgical Research, 90% of preventable deaths on the battlefield occur due to “bleed-outs” where the wounded service member dies from blood loss before reaching a medical facility<sup>1</sup>. Preventing deaths of this nature is due in part to limited supplies in high-risk areas, as well as the increased danger for transporting individuals under extreme duress. The introduction of advanced treatments outside of the clinic for extensive vascular damage in combat areas or for people without proper medical access is an area of interest that can be improved considerably. In developing countries, motor vehicle accidents, street crimes, improvised explosive devices, and industrial accidents are common ways civilians experience vascular injuries of the extremities. In Pakistan specifically, only 41% of 328 documented patients were doctors able to save their arm or leg; 5.48% lost their life<sup>2</sup>. The loss of limb for citizens in Pakistan was due to the prolonged absence of eight hours or more from healthcare facilities, leading to the deterioration of significant vessels or arterials in these advanced trauma areas. Evidence suggests that superior

military and civilian medical treatments are needed to stop otherwise preventable deaths from occurring due to excessive blood loss, pathogen exposure, and prevention of limb loss before transport to a medical facility.

## **1.2 Human Adipose Stem cells for Tissue Regeneration**

Human adipose stem cells (hASCs) provide a research tool for regenerative medicine to be utilized in various capacities. There is a critical research need for additional therapies for bone-related diseases such as osteoporosis, osteomyelitis, and severe trauma areas that can employ the ability of hASCs to differentiate into multiple tissue types such as bone, cartilage, and muscle<sup>3</sup>. Human ASCs can self-renew for extended durations outside of the body and provide an ideal cell source to study therapeutics for bone-specific treatment modalities and other connective tissue disorders. Understanding the dynamic nature of hASCs for bone tissue formation provides a platform for future clinicians to take advantage of hASCs for many connective tissue pathologies.

Human ASCs are abundant and easily accessible in adipose tissue, providing less invasive procedures than other mesenchymal stem cell populations, such as bone marrow stem cells (BMSCs). Not only this, much larger yields of hASCs can be isolated and collected from fat tissue at 250,000 cells per gram, compared to only 50,000 cells per gram of aspirated bone marrow<sup>4,5,6</sup>. Adipose tissue is often disposed of from surgical procedures too, and the fat tissue remains viable for up to 24 hours at room temperature, making it an ideal cell source. Moreover, adipose tissue can easily be acquired through needle biopsy and liposuction procedures. Conventional surface

markers for defining hASCs through flow cytometry are CD73, CD90, CD105 positive and CD14, CD19, CD34, CD45 negative<sup>7</sup>. The increased cell number per gram and the accessibility of fat tissue are two key components that support hASCs application in tissue regeneration studies over BMSCs.

Additionally, hASCs remain viable in cell culture for extended periods in a variety of cellular mediums. The ability of hASCs to be passaged significantly more times than other stem cell sources without fear of genetic malformations is another critical characteristic they possess<sup>8,9,10</sup>. Moreover, when cryopreserved, hASCs are well maintained, allowing researchers to study epigenetic factors including force, elasticity, and genome editing<sup>4</sup>. All of these reasons make hASCs the ideal cellular source for tissue regeneration studies long-term.

As with other stem cell populations, hASCs are vulnerable to environmental pressures acting on them, such as temperature, pressure, microenvironment, and bioactive components<sup>11</sup>. Thus, understanding how hASCs respond to extracellular cues experienced in the body is crucial for optimizing their use in clinical settings. However, mimicking how hASCs respond in the body remains increasingly difficult as hASCs respond to several environmental cues such as sheer pressure/force, biochemical, and substrate adhesion. Directed differentiation and self-renewal processes experienced in the body are difficult to mimic simultaneously and achieve in lab-based experiments<sup>12,13</sup>. However, if we can discover the roles environmental forces and mechanisms of biochemical cues' play in differentiation and proliferation, hASCs remain an ideal candidate for degenerative bone conditions and areas of extreme trauma. For

instance, osteoporosis affects postmenopausal women, where bones weaken significantly over time. In these cases, bone weakening gives rise to broken bones, fractures, and complications due to infection experienced at an older age<sup>14</sup>.

Human ASCs can be utilized and implanted in patients to stimulate formation of new, healthy bone tissue. There are growth factors secreted by hASCs, such as FGF-2 and VEGF, that stimulate angiogenesis through ligand stimulation of enzyme-linked receptor tyrosine kinases (RTK) and directly relate to the formation of healthy bone tissue or other cell lineages<sup>2,15</sup>. FGF-2 and VEGF secreted factors also direct stem cell movement, acting as signaling molecules for immune cells in the wound healing process. Considering the exosome profile existing in the extracellular matrix is essential to note in future studies for characterizing how hASCs or other immune cells in tissue-damaged areas respond by the introduction of biochemical nanomaterials. Understanding how the environment impacts hASCs and their ability to aid in tissue repair will alleviate bone-related pathologies or advance wound healing applications and so needs further study.

### **1.3 Biomaterials for Tissue Regeneration**

Biomaterials have a variety of applications in medicine, including drug delivery, pharmacokinetics, and tissue engineering. Biomaterials are especially useful in biological systems because they do not provoke an immune response and are biodegradable. Combining a cell source with a biomaterial tells a researcher how cells adhere, proliferate, and what genes are influenced by external cues. In particular, biomaterials'

ability to be functionalized to mimic mechanical strength, degradation rate, and cellular adhesion of natural tissues provides a helpful scaffold for differentiation studies<sup>10,16,17</sup>. While biomaterials can be diverse, they can provide a 3D scaffold that better mimics the ECM of the body than traditional culture dishes<sup>18</sup>. Culture dishes grow cells in a 2D environment that do not accurately represent physiological conditions. The 3D scaffold of biomaterials allows researchers to better characterize how cells respond to specified environmental cues.

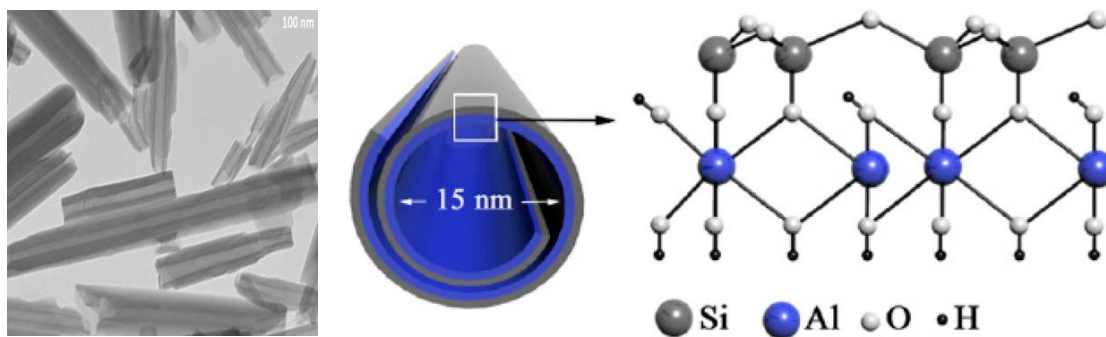


**Figure 1-1.** FE-SEM Image of unmodified HNTs (Left), showing the structure of HNT (center) and a schematic illustration of the chemical structure of HNTs (Right)<sup>19</sup>.

Combinational methods of hASCs with nanomaterials are a growing area of research needing additional studies. Halloysites (HNTs) are hollow alumina silicate nanotubes with an exterior negative charge and lumen positively charged<sup>20</sup>. These nanoparticles range between 100-900 nanometers, while the lumen spans roughly 20 nanometers across. **Figure 1-1** illustrates the chemical nature of HNTs and their cylindrical structure by SEM imaging. HNTs have demonstrated biocompatibility in cell and animal-based studies, with additional capabilities for vacuum loading of drugs and coating metal ions such as silver, zinc, strontium, and copper (mHNTs)<sup>21,22,23</sup>. Vacuum loading drugs into mHNTs provide a significant increase to synergistic antimicrobial

effects on prokaryotes, allowing healthy cell growth in infection risk areas<sup>23,24,25</sup>. **Figure 1-2** demonstrates an HNT-copper complex combined with GHK, along with additional capabilities of vacuum loaded drugs. Furthermore, with antimicrobial properties established, the interactions of nanomaterials with cellular machinery have vast capabilities for promoting healthy tissue formation. The increased surface area to volume ratio at the nanoscale exponentially grows, drastically increasing cellular interactions to cell surface receptors. In addition, the antimicrobial attributes of mHNTs and their biocompatibility provide unique properties for varying methods to be developed in cell-based therapeutics at the tissue level. First, however, various studies must be performed to understand how genes and proteins interact in the tissue formation process with mHNTs. Studying these effects at the molecular level will increase the therapeutic potential for patients.

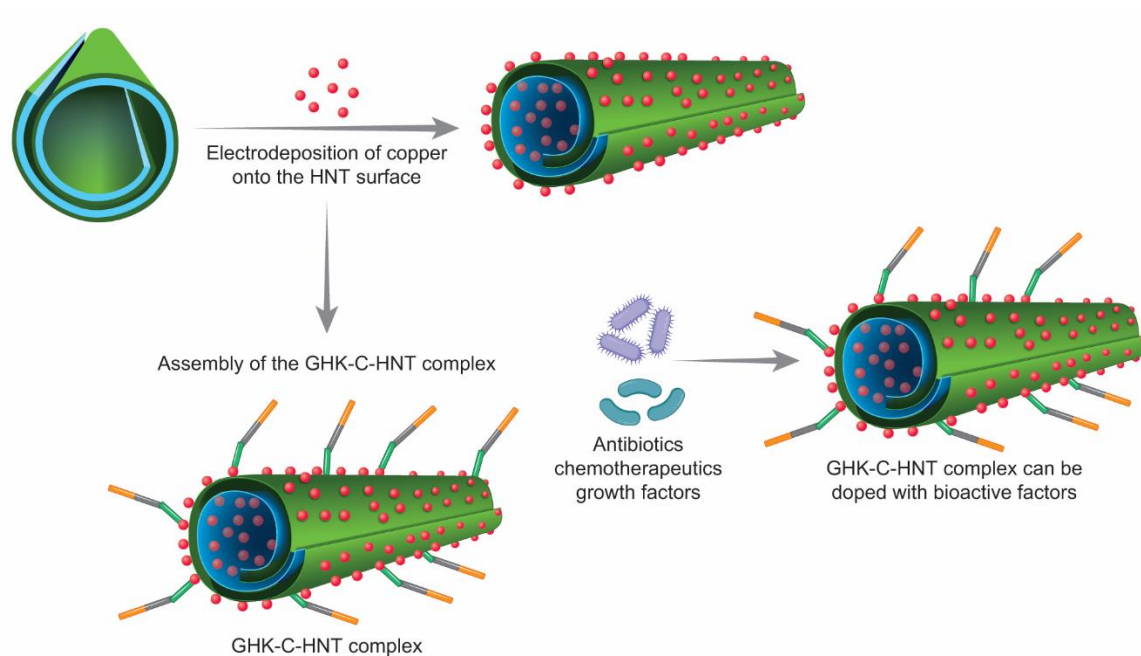


**Figure 1-2.** Graphic Illustration showing Cu deposition on the HNT surface and attachment of the GHK peptide<sup>19</sup>.

Though many different compounds and scaffolds are currently being tested, hydrogels incorporated with crosslinking polymers, or other nanomaterials, are useful to consider for supportive cellular scaffolds. Polyacrylic acid (PAA), polyethylene oxide (PEO), and polyethylene glycol (PEG) are commonly used synthetic polymers. At the same time, fibrin, collagen, alginate, and agarose are natural polymers useful for the creating this support system<sup>16,26,27</sup>. Hydrogels designed for tissue engineering applications absorb water, remain highly hydrophilic, and are structurally similar to the ECM<sup>28</sup>. Thus, the surface of hydrogels can be manipulated while still providing a solid network for cellular attachment or to encapsulate cells for 3D culture studies<sup>29</sup>. Hydrogels also promote gas exchange, prevent nutrient depletion, and readily allow for the diffusion of macromolecules<sup>30</sup>.

However, it remains uncertain as to how the insertion of grooves, depressions, or notches on hydrogels' surface influences cell fate. Furthermore, how other small, naturally occurring biological molecules modulate differentiation has been observed through nanosilicates attached to hydrogels facilitating osteogenesis without the need for bone induction media. The bone induction properties of nanosilicates have led to an intriguing observation regarding how important external cues are in the osteogenesis of hASCs<sup>31</sup>. Additional studies have used nanofibrous mats of chitosan in combination with cyclodextrin hydrogels for wound healing applications and hemostatic potential, leading to increased absorbable capabilities<sup>32</sup>. However, regardless of the materials used within hydrogel constructs, the varied surface of hydrogels has yet to be optimized, and how it impacts cellular attachment, self-renewal, or differentiation.

Elasticity, or rigidity, of biomaterials, is another critical component to consider when designing a valuable biomaterial for directed differentiation. Each tissue type has a corresponding elasticity measured in Pascals (Pa) or kilopascals (kPa). For example, bone tissue is much more rigid. It produces a higher value for elasticity in the range of 40-50 kPa compared to fat and neural tissue corresponding to values under 10 kPa

(Figure 1-3).

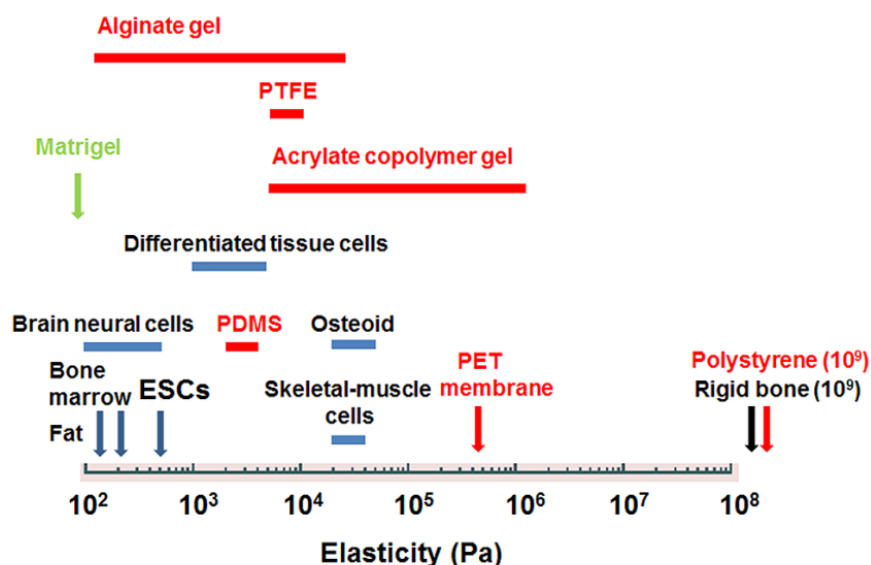


**Figure 1-3.** Elasticities of different cell types, synthetic polymers, and a natural polymer<sup>26,33</sup>.

This biomechanical component of tissue is helpful to analyze as studies suggest that matching the hydrogel elasticity with the elasticity of the desired tissue type greatly influences differentiation and self-renewal processes<sup>34,35</sup>. Human cells grown on hydrogels closely related to its elastic modulus displayed a significant rise of engrafted cells and lineage-specific markers compared to a standard cell culture dish<sup>35</sup>. Utilizing biomaterials will identify the importance of the elastic modulus for influencing stem cell fate.

## 1.4 Wound Healing Fundamentals

The wound healing process is a complex process due to inflammatory markers, immune cells, chemotaxis, and supporting cellular growth. The healing cascade relies initially on inflammatory processes to recruit immune cells and stop blood flow through hemostatic interactions<sup>36</sup>. Hemorrhage is a leading cause of traumatic injuries seen throughout the world, leading to a total cost of 671 billion within the United States as of 2013<sup>32</sup>. Other complications aside from hemorrhage can occur, and preventing sepsis and promoting cellular growth is essential before a wound can adequately heal. Moreover, while typically associated with clotting, aggregation and activation of platelets promote deposition of extracellular matrix-like transforming growth factor  $\beta$ , platelet-derived growth factor, fibroblast growth factor, and vascular endothelial growth factor<sup>37</sup>. The secretion of growth factors is essential for the wound repair process to recruit immune cells, mesenchymal stem cells, fibroblasts and stimulate cell differentiation<sup>38,39</sup>.

However, the process and timing of subsequent factors are poorly understood, and mechanisms to understand or speed up the process are essential for chronic and advanced wound trauma. The wound healing process occurs in four stages that drive healthy tissue formation over time, including hemostasis, inflammation, proliferation, and remodeling. Hemostasis occurs in primary and secondary phases. Primary hemostasis is the initial response in open wound systems to restrict blood loss and bleed outs. However, the wound healing process is slow activating, so the transcription-independent pathway is essential in the first few minutes following injury. Calcium ion

waves build along the wound edge, propagating toward the center of the wound. The damaged cells in the area immediately release chemokines for the stimulation of immune cells by G-coupled receptors<sup>39</sup>.

The primary hemostatic response is divided into four additional phases: vasoconstriction, platelet adhesion, platelet activation, and platelet aggregation. Vasoconstriction and vasospasms occur instantaneously, triggering an initial response whenever there is significant vessel injury. Vasospasm of the blood vessels induces vasoconstriction, and in turn, mediates the release of a potent vasoconstrictor known as endothelin-1, which is secreted by damaged endothelium. In addition, the damaged endothelium releases several other factors in the hemostatic process, such as Willebrand factor (vWF) and inflammatory mediators, along with the TF-FVIIa complex, which acts as a blood coagulant activating an important receptor known as tissue factor (TF)<sup>40</sup>. The secreted factors by the damaged endothelium start mechanistic action of primary hemostasis, leading to platelet adhesion, activation, and aggregation.

Platelet adhesion is the process by which platelets attach to the exposed subendothelial tissue to form a platelet plug with each other through a tightly packed integrin network linking other platelets in the area<sup>39</sup>. Platelets are secreted by megakaryocytes residing in bone marrow, and after secretion, platelets traverse through vascular sinuses of marrow to enter the bloodstream<sup>41</sup>. As platelets begin to adhere to damaged tissue sites, additional platelet activation is mediated through G-protein coupled receptors (GPCRs) on the platelet's surface via thrombin by two mechanisms. First, thrombin directly activates platelets via proteolytic cleavage by

binding the protease-activated receptor. Second, thrombin additionally activates platelet granule release, including serotonin, platelet-activating factor, and Adenosine Diphosphate (ADP)<sup>42</sup>. ADP is an essential physiological mediator that is specifically stored within platelets and only released upon vascular injury. When ADP is released, it binds to two important GPCRs known as P2Y1 and P2Y12 along the platelet membranes<sup>43</sup>. P2Y1 induces the pseudopod shape change and aids in platelet response aggregation. Mice deficient in P2Y1 and P2Y12 exhibit longer bleed times as well as impaired aggregation of platelets at wound sites<sup>44</sup>. The platelet aggregates formed in the system are composed of type III collagen, fibrin, and other glycoproteins to stimulate the release of additional cytokines, promoting angiogenesis. Ultimately, primary hemostasis allows the culmination of a weak platelet plug to temporarily protect from hemorrhage until further stabilization of fibrinogen to fibrin via thrombin occurs.

### **1.5 Tripeptides for Wound Healing Applications**

Incorporating small molecules into an open wound system can aid in recovery, both for suppressing pain management and speed of wound recovery<sup>45</sup>. GHK (glycyl-L-histidyl-L-lysine) is a naturally occurring tripeptide found in all mammals and a significant component of type 1 and many other collagens. GHK is released into damaged tissues after hydrolysis of collagen by collagenases or actively secreted by fibroblasts. It is theorized to be a feedback signal for fibroblast activation and synthesis of a reparative extracellular matrix<sup>46</sup>. Furthermore, over time, circulating levels of GHK in the bloodstream drop from 200 ng/mL to 80 ng/mL in elderly patients, causing

increased problems related to wound healing, cartilage degradation, and wrinkle formation<sup>47,48</sup>. GHK is known to have many physiological properties and interact with genes and proteins involved in skin repair, inflammation, pain, stress, and anxiety<sup>45</sup>. For example, transforming Growth Factor Pathway-Beta (TGF-B) and Integrin-Beta 1 pathways were stimulated by injections of GHK-Cu in mouse and rat studies that reduced aggression or pain, along with improved healing of ischemic wounds<sup>45,47</sup>. GHK-Cu was also found to stimulate basal epidermal cells, markedly increasing integrin expression and p63 expression<sup>47</sup>. Furthermore, because GHK is a potent chelator, it binds with high affinity to metal ions such as copper, zinc, or silver through covalent bonding of free nitrogen groups within the crystal structure of the GHK molecule. Thus, the metal ions act as transport vesicles to avoid protease activity and aid in the tissue repair system.

Incorporating GHK with biomaterials is another area to explore. For example, GHK-Cu complexes in 3D extracellular cryogels accelerated cytokine secretion profiles of VEGF and members of the Interleukin family for immune homing of human umbilical vein endothelial cells<sup>49</sup>. The rise in growth factor secretion and immune homing of GHK-Cu in cryogels suggests the importance of tripeptides, particularly GHK, in the healing process. The secretion profiles also suggest that tripeptides could increase wound site recovery in chronic wound patients or everyday scrapes and burns.

Although GHK appears to be an ideal molecule to use in wound repair, a significant challenge is to prevent degradation of GHK after incorporation into an open wound. GHK can further be functionalized with fatty acids, such as stearic acid and

palmitic acid, that increase its absorption capabilities and prevents degradation of the tripeptide by protease activity in open wounds<sup>47,48</sup>. Both stearic and palmitic acid are among the most common saturated fatty acids consumed in the western diet and could aid in preventing GHK degradation, thus promoting tissue regeneration<sup>50</sup>. Palmitic acid conjugated peptides increase cell permeability while stabilizing peptide delivery to cells. Modifying peptides with fatty acids can substantially improve their pharmacokinetics, increasing the affinity of binding to MHC class II and T-cell receptors. For example, Liraglutide, a peptide drug for treating type 2 diabetes, has a fatty acid attached, extending the half-life by 11–15 hours, and drug delivery methods with palmitic acid-conjugated exendin-4 markedly prolonged circulation of the amino acid complex in diabetic murine studies<sup>51</sup>. The stearic acid-modified peptide is resistant to degradation mediated by thrombin and trypsin, significantly increasing the half-life and anticoagulant activity<sup>52</sup>. Peptides conjugated with fatty acid have the potential to prolong the half-life in the circulation, increase cell penetration, or impact antibacterial activity. Advanced nanoparticle delivery and layer-by-layer assembly are major research areas and need additional studies to enhance wound healing processes.

## **1.6 Synthesizing Tripeptides**

Synthesis of peptide chains has been around for several decades, with advancements directed towards developing therapeutic potential in cell-based systems. The research need for producing particular proteins or amino acid chains is highly relevant to studying metabolic functions, pharmacokinetic properties, and tissue engineering approaches<sup>51,53</sup>. There are two common ways to form amino acids

depending on the insoluble nature of the protecting group and the direction of the synthesis. Solid-phase synthesis uses an insoluble protecting resin, while solution-phase synthesis uses a soluble protecting resin<sup>51</sup>. Protecting groups are essential during the formation process for side chains not to be developed, markedly decreasing purity levels. Tertbutyloxycarbonyl (Boc)/benzyl (Bzl) strategy and 9-fluorenylmethoxycarbonyl (Fmoc)/tert-butyl (t-Bu) strategy are the two most common approaches for the development of peptide chains. The latter, Fmoc, is the ideal strategy for the solid-phase peptide synthesis due to the nature of Boc as a protecting compound. Boc often produces alterations to peptide bonding or side chains after repetitive treatment of trifluoroacetic acid to remove Boc as the protecting group during peptide synthesis, so the desired choice for solid-phase synthesis with high purity levels is generally Fmoc<sup>54</sup>.

The peptides can further be built in a layer-by-layer addition through lipidation methods to improve receptor binding, half-life in circulation, plasma stability in open wounds, and physiochemical properties<sup>55,56</sup>. The presence of the fatty acid of varying links can have large changes in cellular interactions and ultimately the interactions of genes and proteins within the cell. Palmitoyl esterification of serine or cysteine can easily be accomplished in trifluoroacetic acid (TFA) solvent for conjugating palmitoyl group to the peptide chain<sup>57</sup>. Lipidation methods are attractive strategies for peptides, proteins, and other small molecules for an enhanced effect in cellular response pathways.

## CHAPTER 2

### WOUND HEALING, BONE REPAIR, AND REGENERATION

#### 2.1 Improving Current Healing Capabilities

Deploying a nanotechnology-enabled, multi-functional hemostatic bandage made from FDA-approved materials and fabricated with additive manufacturing techniques can drastically improve how we repair wounds from the onset. The use of tripeptides, like GHK, can potentially impact lives while increasing our knowledge of the nanomaterial influence on hASCs. **Figure 2-1** illustrates how FDA approved materials can be combined with our biologically active nanoparticle combined with GHK and CuHNTs. The proposed design is aimed to be hemostatic, alleviate infection, promote tissue growth, and ease pain and inflammation on skin surfaces. The clinical use of hASCs is an area of research with potential therapeutic use for various pathologies related to connective tissue, making it an ideal model to study cellular interactions for the formation of dermal layers. However, more research needs to be performed to optimize the clinical potential of bioactive based nanomaterials and directed differentiation of hASCs for wound trauma. Therefore, understanding how nanomaterials combined with biological molecules dictate gene expression and influence cell fate are essential factors for considering tissue engineering models associated with hASCs.

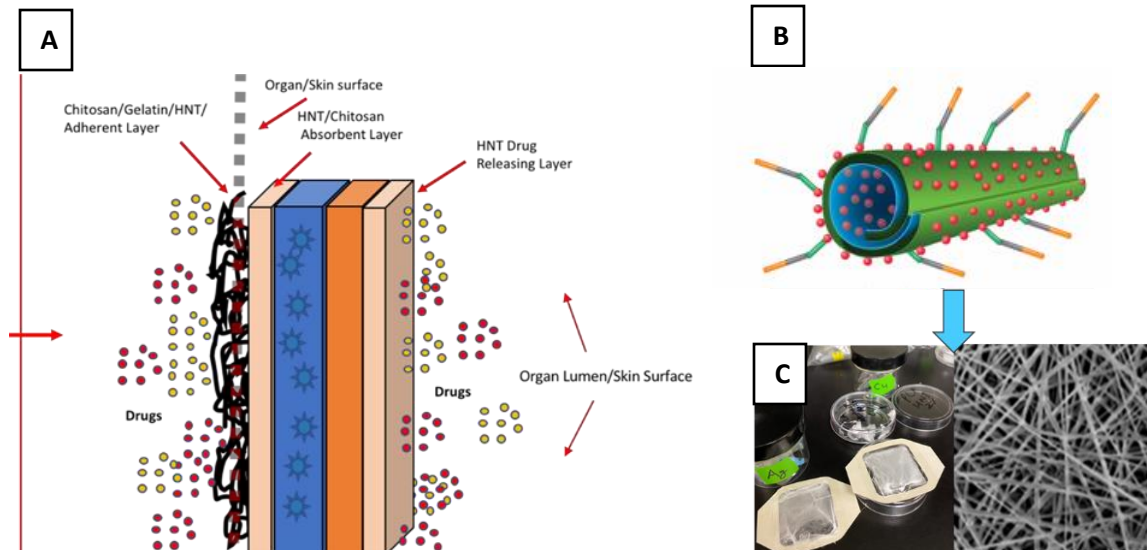


**Figure 2-1.** A.) A hemostatic bandage incorporated with metalized halloysites and GHK tripeptides for wound healing applications. The bandage lines the dermal surface in open wounds, and multiple layers can be created to enhance hemostasis, pathogen resistance, and promote tissue formation. B.) Proposed GHK-Cu-HNT complex to incorporate into blow-spun or electro-spun fibers. C.) Blow-spun fibers created and analyzed by SEM (right) and a prototype bandage constructed (left).

Current bandage components do not incorporate advanced nanocomposite therapies for stimulation of healthy cell growth, infection control, or tissue regeneration. Skin grafts are generally used for large scale scrapes or burns<sup>58</sup>. The United States government currently employs the “QuickClot” bandage to rapidly promote hemostasis during battlefield-induced injuries. The components of QuickClot comprise nanomaterials similar in nature to halloysites, known as kaolin, for enhanced coagulant properties and stimulation of platelets in open wound systems<sup>59,60,61,62</sup>. While the kaolin improves bandage materials comprised in gauze, the materials do not provide synergistic activities for type I and type III collagen formation or antimicrobial properties. Deploying bandages in countries without proper medical access or for warfighters in isolated combat areas remains of interest to prevent septic conditions,

ultimately save lives in the process. In addition, the wound repair process in the elderly population slows in epidermal areas, infection rates increase, and complications arise in diabetic wounds<sup>63</sup>. My studies will incorporate advancements in current bandage components to prevent infection, alleviate pain and inflammation, and speed recovery time. Using hASCs, combined with metalized halloysites and tripeptides, will provide needed and novel bandage capabilities that provide insight into stimulating trauma areas in many different populations.

My research aims to fill gaps associated with nanocomposites' biological relevance for wound healing applications while better understanding the nature of stem cells and mHNTs. Gene expression analysis, wound healing assays, and immunofluorescent techniques will be used to identify the cellular effects of our nanocomposites on hASCs. Understanding and optimizing conditions to differentiate hASCs could provide an ideal cell population to generate different tissues for patients suffering from genetic abnormalities, severe trauma, deficiencies, or bone decay. The proposed research on incorporating tripeptides with metalized halloysites will offer new wound healing applications after additional studies on animals and humans. Future research on animals and humans must identify how our functional components can substantially increase the current bandage capabilities. Our specialized nanoparticles can easily be incorporated into FDA-approved materials like PLA, chitosan, or cotton indicated in **Figure 2-2**. With this technology and additional studies, we are confident that improving current bandages is possible in the near future.

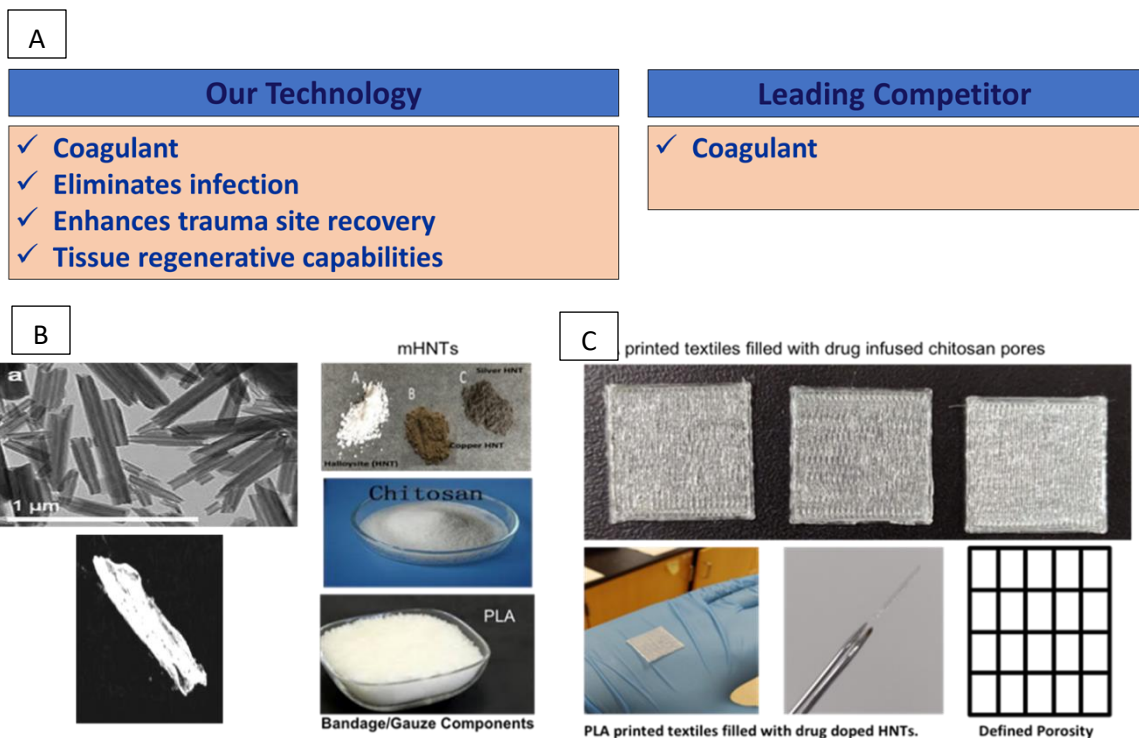


**Figure 2-2.** A.) The proposed bandage solution would be used with FDA approved materials, metalized HNTs, tripeptides, and drastically improve upon leading competitors. B.) Chitosan and PLA that can be combined with metalized HNTs in blow-spinning methods. C.) PLA printed textiles can be infused with metalized HNTs, or drugs, and they can provide structural support in tissue damaged areas.

## 2.2 Bone Formation Processes

The complexities of the bone formation process extend through multiple mechanistic processes from secreted polypeptides in conical signaling pathways within the transforming growth factor-beta family or bone morphogenetic pathways<sup>64,65</sup>. Furthermore, the similarities between bone and wound healing run parallel because coagulation and inflammatory phases occur similar to those seen in disrupted skin, requiring identical molecules associated in these pathways with frequent crosstalk in trauma-induced areas given the similar regions and tissue types.

When bone tissue is damaged, a fracture hematoma is replaced by a soft or fibrous callous as BMSCs are stimulated to form preosteoblasts. Intramembranous ossification occurs on the border of the fracture site where signaling molecules BMP-2 and RANKL stimulate osteoblast formation<sup>65</sup>. After initial soft tissues are formed, hard callus formation follows in 3 to 4 months, giving way for possible injuries to occur or infection to grow if the union of the fracture is not met<sup>66</sup>. If the fracture union is established, the endochondral ossification establishes a bony bridge to stabilize the fracture and prevent micromotion centrally. Hard callus formation is followed by bony remodeling through osteoclast activity stimulated by ion exchange of strontium to differentiate MSCs into osteogenic lineages<sup>67</sup>, wherein woven bone is replaced by lamellar bone, similar to the process of exchanging the web of type III collagen for type I collagen in the skin.

The dynamic process of bone formation requires several steps to take place over many months in severe bone injuries, often leading to non-union of fracture sites. In non-union fractures, surgical intervention with autogenous bone from the iliac crest represents the “gold standard.” Other methods such as low-intensity pulsed ultrasounds, titanium rods/screws implants, and extracorporeal shockwave therapy exist as well <sup>66</sup>. However, complications of additional surgeries, infection, pain, scarring, and daily trips to therapy clinics provide problematic scenarios.

There are 3 primary cell types that influence the environmental landscape for bone formation. BMSC-derived osteoblasts along the basolateral surface interact with the bone mineralization process, further directing downstream cell differentiation

processes. Osteoid, the first matrix produced, is comprised mainly of collagen and calcium phosphate<sup>68</sup>. Through alkaline phosphatase (ALP) activity on the osteoblast surface, hydrolyzed hydroxyapatite crystals of the non-mineralized bone matrix fuse to mineralize the osteoid, forming the bone matrix. **Figure 2-3** highlights the integrated ALP action taking place along the surface of an osteoblast to form healthy bone tissue with hydroxyapatite crystals in an acidic environment. While ALP exists in several other tissues in different isoforms, it is imperative in early bone formation processes. Runx2 is another bone marker directly involved early in determining an osteoblast's functional characteristics. It acts as a transcription factor that stimulates downstream targets such as fibroblast growth factor receptor (*fgfr2-3*), essential for proliferation and differentiation of osteoblasts<sup>69,70</sup>. Mice deficient in *runx2* inhibited downstream atypical expression of *fgfr2-3*, leading to abnormal proliferation of osteoblast progenitors in the calvariae and mandibles<sup>69</sup>. The osteoblast performs various functions in osteogenic repair, homeostasis of the bone matrix, and downstream differentiation, so ALP and Runx2 execute proper communication pathways early in bone formation.

Osteoclasts are a second primary cell type within the bone matrix required for health maintenance. The osteoclast primarily acts to resorb bone tissue that is damaged or in the process of dying so that osteoblasts can lay down the additional mineralized bone matrix. Several diseases are related to abnormal osteoclast activity, such as osteoporosis, osteopetrosis, Paget's disease, and rheumatoid arthritis<sup>71</sup>. Therefore, the dynamic process of osteoclast and osteoblast activity needs to be finely balanced to promote proper bone growth, especially in damaged tissue areas.

The last primary cell type residing within bone is the osteocyte that comprises 90-95% of the total cell population within bone tissues<sup>14</sup>. The osteocyte forms many extended constituents protruding from the cell body forming junctions with other neighboring cells within the canaliculi. Osteocytes mainly act as sensory cells whenever mechanical or chemical strains of the osteon are endured, acting as a feedback loop to activate osteoblast and osteoclast activity.

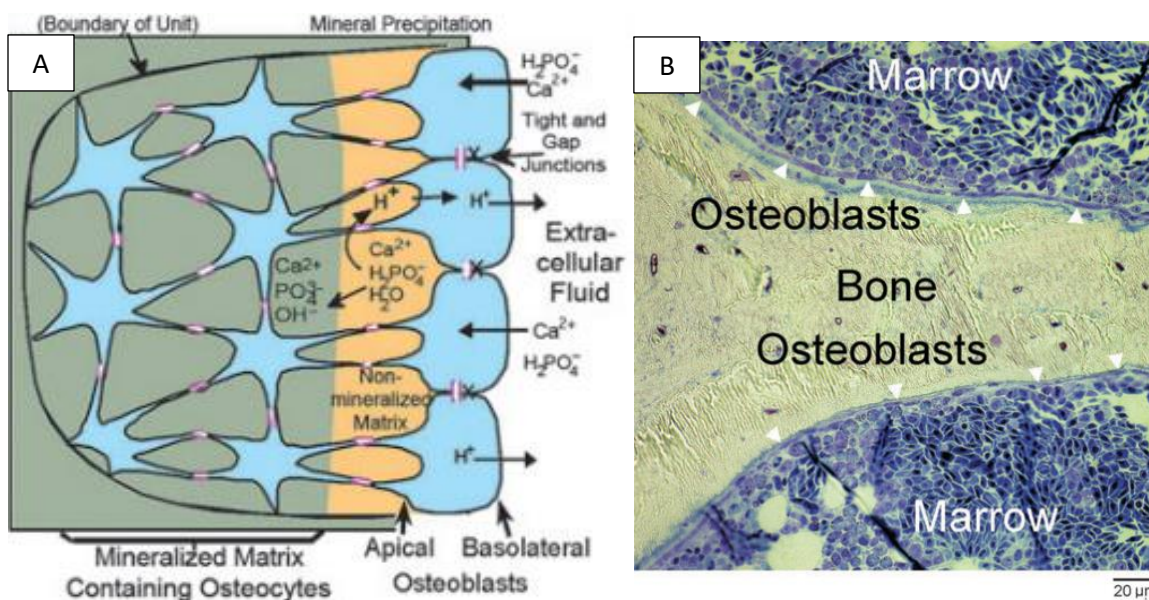


**Figure 2-3.** A.) The basic features of osteoblast organization, an osteon. During bone mineral transport, the process of mineral deposition produces acid. Exclusively during mineral transport, osteoblasts also transport hydroxyapatite-binding fluorescent molecules B.) A low-power view showing the continuity of bone-lining osteoblasts (white arrows) and well-preserved marrow; dark regions are developing red blood cells<sup>72</sup>.

### 2.3 BMP Signaling pathway

The cascade of events that occur with the introduction of Bone Morphogenetic Proteins (BMPs) in cellular development and subsequent metabolic pathways is complex. However, this process must thoroughly be understood so future therapies can be provided for gene therapy interventions and targeted molecular therapies are

designed properly. BMPs allow for many essential biological processes to function like bone formation, cell growth, and differentiation. For example, without BMP-2 or BMP4-4 protein complexes, the body would not thrive and maintain homeostasis. BMP-2 and BMP-4 are two closely related members of the TGF-Beta superfamily<sup>73</sup>. The TGF-Beta superfamily comprises many different proteins that exist within the body handling many different bodily functions. Regulation of cell growth, proliferation, differentiation, adhesion, migration, and apoptosis are all processes controlled by this superfamily of proteins<sup>74</sup>. Other proteins in the TGF-Beta family include activins/inhibins, growth differentiation factors, and Glial Derived Neurotrophic Factors<sup>75</sup>. All BMP molecules share a distinct feature on the C-terminus end; this region contains seven cysteine residues<sup>75</sup>. The BMP family can be further classified into subclasses. Subclass A includes BMP-2 and BMP-4 due to the 80% homology seen between the two proteins. They are also 92% identical on the carboxyl-terminal regions in regards to their amino acid sequence<sup>76</sup>.

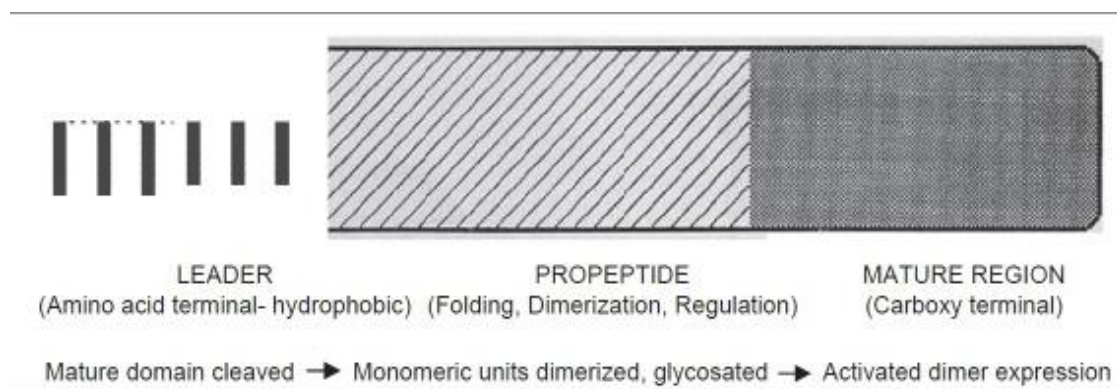


**Figure 2-4.** Chemical structure of a BMP molecule before secretion out of the cell<sup>76</sup>

The homology seen between BMP-2 and BMP-4 is something to note. This indicates similar functions for each of these two proteins recognized as factors to induce

differentiation. In the absence of BMP-4, BMP-2 can compensate for resolving the cascade of events temporarily, and experiments performed with mice demonstrated this situation as gastrulation of embryos does not usually occur in the absence of BMP-4. Furthermore, BMP-2 overlaps BMP-4 localization sites in the heart, amnion, and allantois due to the protein homology. This can help induce further development than expected in embryos if BMP-4 is absent or dysfunctional<sup>76</sup>. BMP-2's involvement would be anticipated to replace BMP-4 as the genetic sequence allows the system to temporarily rely on BMP-2 until an adequate supply of BMP-4 can be used once again, as this was the case in experiments performed. BMP-4 was removed from an embryo *in vitro* to see its effects on embryogenesis and the ability to maintain homeostasis. Most embryos did not survive past one week, but some embryos did survive past this stage when BMP-2 was overexpressed. In overexpressed cases, BMP-2 needed to be up-regulated as BMP-2 would still need to perform the normal functions it associates with, such as preserving functional characteristics of the amnion, gut, and heart<sup>77</sup>. The developing embryos still ended in a fatality in the absence of BMP-4, though, suggesting that BMP-2 cannot sustain all of the functions of BMP-4 long term.

The actual BMP signaling cascade starts with an initial precursor molecule inside the cell's cytoplasm before secretion of the mature BMP molecule can occur. The pre-protein consists of a signal peptide, propeptide domain, and a mature peptide sequence on the carboxy-terminal (**Figure 2-4**)<sup>75</sup>. Once a signal generates a need for BMPs, the signal peptide of the BMP is cleaved to start the secretion process. The BMP molecule undergoes glycosylation and dimerization of the propeptide domain and mature peptide

sequence. The propeptide domain is cleaved after the glycosylation and dimerization but before secretion out of the cell. Thus, a conformational change occurs after secretion to form the newly created BMP ready to be used by cellular mechanisms throughout the body. The mature BMP is derived from the carboxy-terminal region as a heterodimer or a homodimer <sup>75</sup>.

**Figure 2-5** represents the BMP pathway with a cell surface receptor that initiates signaling transduction of transcription factors including NKX2-5, ATF-2, MEF2C, HAND2, and MYOCD, along with the Smad complex within the cytoplasm.

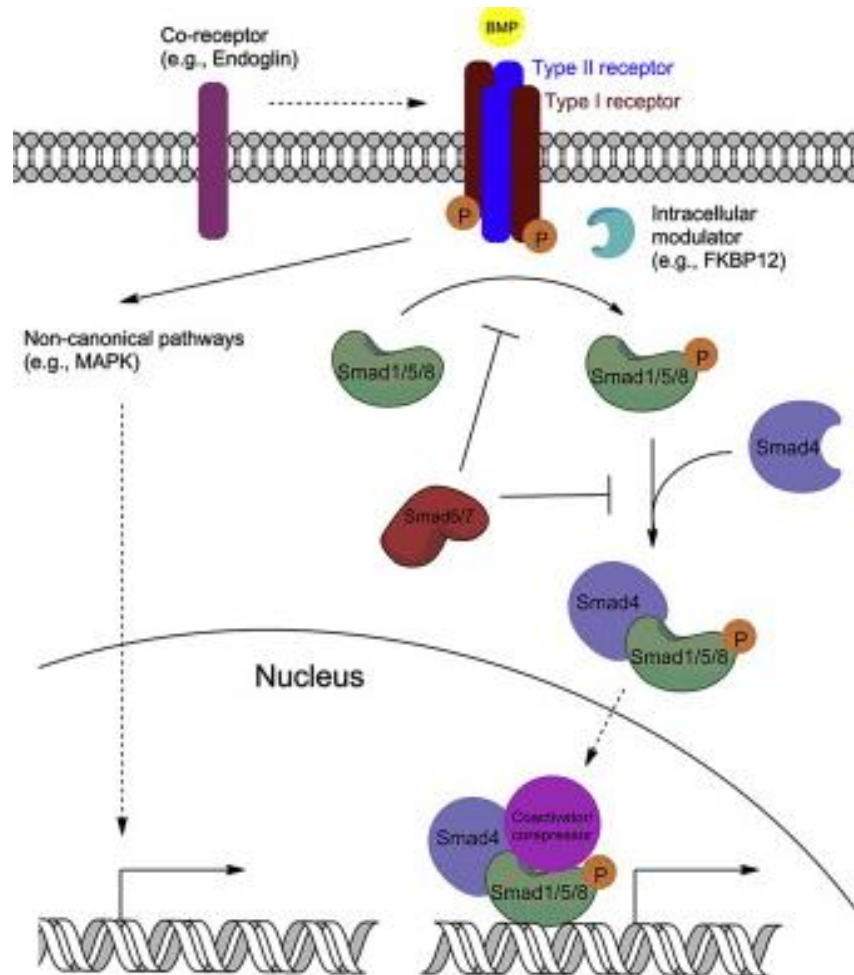


**Figure 2-5.** Schematic of the mechanistic process of the signaling cascade for BMP and its associated receptor<sup>73</sup>.

BMPs first bind to cell surface receptors based on the BMP molecule, where a signal complex initiates the process. BMP-2 and BMP-4 bind to type I (ALK3 and 6) receptors, while BMP-6 and BMP7 bind to type II receptors (BMPR-2, ActR-2A, ActR-2B). Moreover, when a BMP molecule binds to its particular receptor, the event signals a close-by type I or type II receptor to be phosphorylated, creating a high-energy complex of Smad proteins within the cytoplasm. Smad protein complex act as a signal transducer within the cytoplasm to activate a transcriptional response within the nucleus<sup>75</sup>. Several Smad proteins exist in different locations throughout the body, forming unique complexes dependent on the type of BMP bound to the cell's receptor. Generally, Smad-1, Smad-5, and Smad-8 form heteromeric complexes with Smad-4 within these activated complexes. Smad-6 and Smad-7 proteins act as inhibitors to the system if overexpression occurs<sup>75</sup>. Other modulators such as Noggin exist outside the cell and bind to the receptor without a BMP molecule. The BMP signaling cascade directly impacts the differentiation process into osteogenic lineages and is essential for healthy tissue formation in trauma-induced areas.

## **Chapter 3**

### **DETERMINING EXPRESSION OF GHK AND MHNTS WITH HASCS**

#### **3.1 Introduction**

While the capacity for the use of hASCs in tissue engineering shows promise, the influence of GHK conjugated tripeptides on their proliferation and osteogenesis has not been characterized with metalized halloysites. Nanomaterials have shown great promise to influence a stem cell's capacity to grow and differentiate, so combining metalized halloysites with tripeptides will increase our knowledge for wound healing applications. In addition, developing enhanced therapies for the use of stem cells for regenerative medicine can advance nanomaterial capabilities. This leads to a better understanding of manipulating and using the cells for tissue engineering and other clinical purposes.

Glycyl-L-Histidyl-L-lysine (GHK), GHK-palmitic acid (GHKP) and GHK-stearic acid (GHKS) were incorporated into stem cell cultures at the desired concentration of 50 micromolar to determine the impact on hASCs proliferation and gene expression profiles. The nanoparticles were characterized through mass spectroscopy, purified by

high-performance liquid chromatography, and further characterized with electron dispersion spectroscopy (EDS) and scanning electron microscopy (SEM).

We hypothesized that hASCs would differentiate into a fibroblast morphology after incorporating tripeptides and CuHNTs, and osteogenic potential will decrease after CuHNTs and tripeptides are applied to cell-based cultures. SrHNTs will develop and stimulate bone markers in gene expression due to strontium being a synergistic metal ion for osteoclast activity. Exploring the role of GHK with metalized halloysites has significant implications to stimulate pathways in hASCs for the formation of different tissues. The qualitative and quantitative results will lead to a better understanding of gene expression during the differentiation and proliferation process of hASCs.

The influence of biomaterials on stem cell fate will be evaluated using metalized halloysites and metalized halloysite composites incorporated with GHK, GHKP, and GHKS. GHK has a high affinity for copper in nature, and previous lab members have demonstrated the ability to metalize halloysites with copper (CuHNTs). GHK, GHKP, and GHKS were mixed at a 1:1 ratio with CuHNTs in dry powder and incubated overnight, upon being placed in ultrapure water at 8°C before added to *in vitro* models with hASCs. The experimental design was evaluated through particle confirmation-based assays followed by live-dead and gene expression analysis.

## 3.2 Materials & Methods

### 3.2.1 Particle Confirmation

#### 3.2.1.1 *Mass Spectrometry (MS)*

Tripeptides GHK, GHKP, and GHKS were formed from solid-phase synthesis by LifeTien LLC, confirmed through MS by LifeTien LLC, and shipped overnight (Lifetien.com)

#### 3.2.1.2 *High performance Liquid Chromatography (HPLC)*

Reverse phase HPLC purified the tripeptides and then were shipped by LifeTien LLC overnight (Lifetien.com). The tripeptides were processed through a polar mobile phase and a non-polar hydrophobic stationary phase. The non-polar phase utilizes Carbon 18 molecules attached to a silica substrate. This allows a wide range of molecules to be purified.

#### 3.2.1.3 *Scanning Electron Microscope (SEM)*

The tripeptides were imaged with SEM to better visualize the particles at the nanoscale and confirm the presence of attachment of the tripeptide to metalized halloysites. 0.1 g of each nanoparticle was loaded onto a metal disc that was coated with a carbon-polymer tape to anchor down the samples. Tripeptides were coated with a 5-nanometer silver layer using a sputter prior to visualization to enhance contrast. The samples were then loaded into the vacuum chamber for analysis. Measurements were taken at x400, x8k, x40k, x80k, and x100k.

#### 3.2.1.4 Energy Dispersion Spectroscopy (EDS)

The mHNTs and tripeptides were analyzed with EDS to confirm the presence of essential elements in the CuHNTs and tripeptides. 0.1 g of each nanoparticle was loaded onto a metal disc that was coated with a carbon-polymer tape to anchor down the samples. The samples were then loaded into the vacuum chamber for analysis.

#### 3.2.2 Generation of nanocomposites

A non-sacrificial standard two-electrode electrolysis setup was assembled consisting of two platinum-coated titanium mesh electrodes acting as a reversible cathode and anode. The electrodes were gently cleaned using silicon carbide abrasive papers and ultrasonicated in distilled water for 10 minutes to remove any surface contamination. The electrodes were held parallel at a 2-inch distance and connected to a DC power source (VWR Accupower 500 electrophoresis power supply).

An ultrasonicated colloidal solution of 700 mL of 5mM CuSO<sub>4</sub> (Sargent-Welch Cat. # WLC3649T) and 350 mg HNT (Aldrich Cat. #MKCF6902) were dispersed in the electrolysis vessel (1000 mL VWR borosilicate glass beaker) and continuously stirred using a magnetic stir bar to reduce electrophoretic buildup and precipitate formation at the working electrode. A temperature of 85°C was maintained during the duration of the electrolysis process. The 20V charge was applied in 5-minute intervals, after which the polarity was reversed. This process continued for a total of six 5-minute cycles for a total of 30 minutes.

The supernatant was decanted and washed with deionized water three times. The solution was centrifuged at 2000 rpm for 5min with water to separate mHNTs from

the unreacted NPs. The supernatant was removed. The unreacted NPs collect on top of the dense pellet after centrifugation and were removed. The mHNTs were then dried at 37°C and stored overnight until combined with GHK, GHKP, or GHKS.

The influence of biomaterials on stem cell fate was evaluated with metalized halloysite composites incorporated with GHK. GHK has a high affinity for copper in nature, so GHK, GHKP, and GHKS were mixed at a 1:1 ratio with CuHNTs in dry powder form, vortexed for 15 seconds, and incubated overnight. The particles were then added to ultrapure water at 8°C. The particles were added to tissue culture plates ranging from 10-50 µM at physiological pH up to 28 days.

### 3.2.3 Cell Culture Media

400 mL of Dulbecco's Modification Eagle's Medium (DMEM) (R&D Cat. #M22650) with 4.5 g/L glucose, L-glutamine, sodium pyruvate was combined with 47.5 mL of fetal bovine serum (FBS)(Neuromics Cat. #FBS002) and 5 mL of penicillin streptomycin solution (Corning Cat. #25815001). The solution was then filtered with a 100-nm vacuum filtration system. The solution was labeled and placed into the refrigerator for storage until ready to use.

### 3.2.4 Cell Culture Growth

ScienCell human adipose-derived stem cells (Cat. #7510) were used as a cell source for this study. Cells were thawed from liquid nitrogen and grown on a 15 cm tissue culture plate to expand the working cell population in an incubator a 37°C and 5% CO<sub>2</sub>. After reaching 90% confluency, cells were passaged for further expansion and experimental studies. First, media was removed, and 3 mL of 0.25% trypsinEDTA (R&D

Cat. #B81210) was added for 3 minutes. The plate was gently tapped and shook to detach remaining cells in the tissue culture plate. 7 mL of media was added to the plate to suspend the cells throughout the media and dilute the trypsin. The cells were spun down at 1500 rpms for 8 minutes and the trypsinEDTA/media solution was aspirated. The cell pellet was resuspended in 10 mL of media upon the cells were being counted on an automated cell counter (Cellometer).

### 3.2.5 Immunofluorescent Live/Dead Staining

The live nucleus was stained blue by using a fluorescent tag that binds to A-T rich regions in the nuclear DNA, known as Hoechst 33342 (2'-[4-ethoxyphenyl]-5-[4-methyl-1-piperazinyl]-2,5'-bi-1H-benzimidazole)(Cat. #A020A). Excitation and emission at 360/460 nanometers. Dead cells were probed with EasyProbes propidium iodide for red at excitation and emission 535/620 or EasyProbes Green at 490/520 (Cat. #A020B). The reading was performed on a Cytation 5 plate reader and cells were counted using the plate reader and ImageJ software.

### 3.2.6 Gene Expression Analysis

#### 3.2.6.1 *RNA Extraction*

Gene expression analysis was performed on samples for 1, 2, 3, 7, and 14 days. RNA was extracted on 6cm tissue culture plates using 500 microliters Trizol (Invitrogen Cat. #15596026). The cells were incubated for 5 minutes upon a cell scraper being used to collect the tissue. The mixture was placed in an Eppendorf tube with 100 microliters of chloroform (Aldrich Cat. #SHBG1013V) and inverted 15 times over two minutes. The samples were then centrifuged at 15,000g for 15 minutes. The tube contents were

separated into 3 distinct layers. The RNA was carefully extracted from the top, transparent layer and avoided the thick mucus middle and bottom phenol layer. The supernatant was added to an Eppendorf with 25 micrograms of glycogen (Roche Cat. #34990920) and 100 microliters of 99% propanol (Cat. #SHBL3018). The supernatant was centrifuged again at 12,000g for 10 minutes. The pellet was then located on the hinge side of the Eppendorf tube and the solution aspirated. The pellet was resuspended in 75% propanol and centrifuged at 7500g for 5 minutes. The solution was again aspirated, leaving only the remaining pellet to air dry. After the pellet became clear, 50 microliters of RNase free water diluted the RNA for storage at -80°C.

#### 3.2.6.2 *RNA Quantification*

The nanodrop plate of the Cytation 5 plate reader was used to quantify the extracted RNA. Two microliters of water were first placed on the nanodrop to filter out the nuclease-free water in which the RNA is suspended. After the machine was blanked, two microliters of the RNA sample were added in duplicate, and the values were averaged to give concentration levels. The reading provided values in nanograms per microliter and a 260/280 reading for RNA purity levels. In general, a value between 2.0-2.1 is considered to be pure RNA.

#### 3.2.6.3 *cDNA Synthesis*

The cDNA synthesis was carried out immediately following RNA quantification. In total, 1 microgram of RNA was used to reverse transcribe the quantified RNA using a cDNA synthesis kit (ABM Cat. #G452). Synthesis was carried out using a Quantstudio3. The cDNA was stored overnight at -20°C.

### 3.2.6.4 RT-qPCR

Gene expression analysis was performed using a QuantaStudio3 fluorescent 96 well imager. Primers were designed for *gapdh*, *runx2*, *ki67*, and *osteopontin* using the primer blast function at <https://www.ncbi.nlm.nih.gov/>. Each well contained 4 microliters RNase free water, 4 microliters of Sybergreen (BioRad Cat. #64356402), 0.5 forward primer, 0.5 reverse primer, and 1 microliter of cDNA. A total of 50 nanograms of cDNA was used per reaction. A melt curve was also performed to indicate, if any, inadequate primer sequences.

**Table 3-1.** Oligonucleotide primers used in RT-PCR analysis

<p><i>Runt-related transcription factor (runx2)</i>            GCGGTGCAAACCTTCTCCAG (forward)            TGCTTGCAGCCTTAAATGACTC (reverse)</p>
<p><i>Osteopontin (opn)</i>            AAGCAGCTTTACAACAATACCCA (forward)            GACTTACTTGGGAAGGGTCTGTGG (reverse)</p>
<p><i>Marker of proliferation (ki67)</i>            CTTTGGGTGCGACTTGACGA (forward)            ACAACTCTTCCACTGGGACG (reverse)</p>
<p><i>Glyceraldehyde 3-phosphate dehydrogenase (GAPDH)</i>            ACCACAGTCCATGCCATCAC (forward)            TCCACCACCCTGTTGCTGTA (reverse)</p>

### 3.2.7 Statistical Analysis

Statistical analysis was performed using the Microsoft Excel Analysis plugin and online software sources at [https://astatsa.com/OneWay\\_Anova\\_with\\_TukeyHSD/](https://astatsa.com/OneWay_Anova_with_TukeyHSD/). All experiments were done in triplicate and with one-way analysis of variance (ANOVA) with  $p < 0.05$  as the significance level for statistical analysis and all the results were reported as mean  $\pm$  standard error ( $p < 0.05$ ,  $n=3$ ), unless otherwise specified.

## 3.3 Results

### 3.3.1 Mass Spectrometry

Mass spectrometry evaluated particle size before being received from LifeTien LLC. Parent Peaks at the far right of each spectrum indicate the molecular weight of GHK, GHKP, and GHKS in **Figures 3-1** to **Figure 3-3**. Results indicate confirmation of each tripeptide formed. Purity levels, chemical formula, and theoretical values of each tripeptide are listed in **Table 3-2**. All tripeptides were above 98% pure after analysis by high performance liquid chromatography.

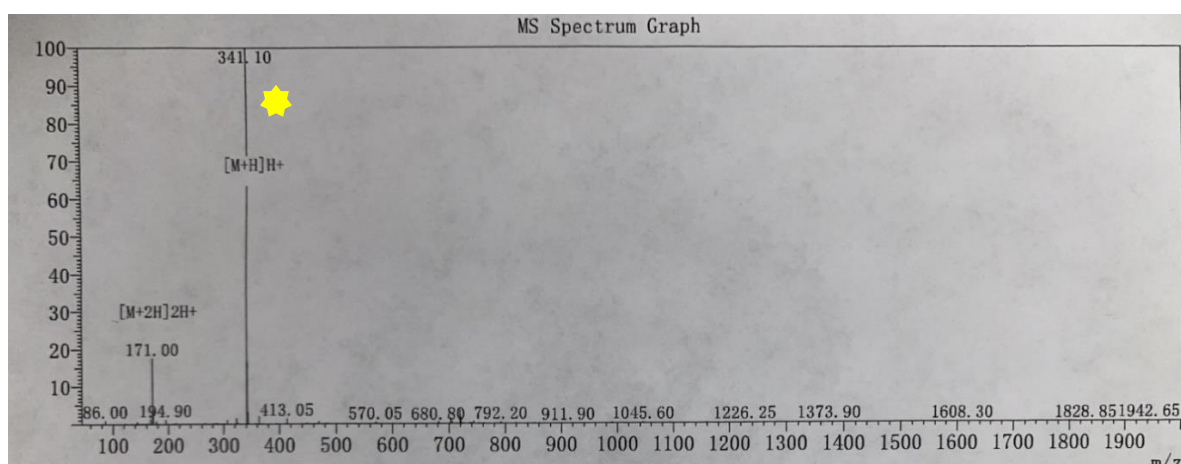


**Figure 3-1.** Mass spectrum of GHK. The parent peak to the far right (yellow star) indicates particle formation at a molecular weight of 341 g/mol.

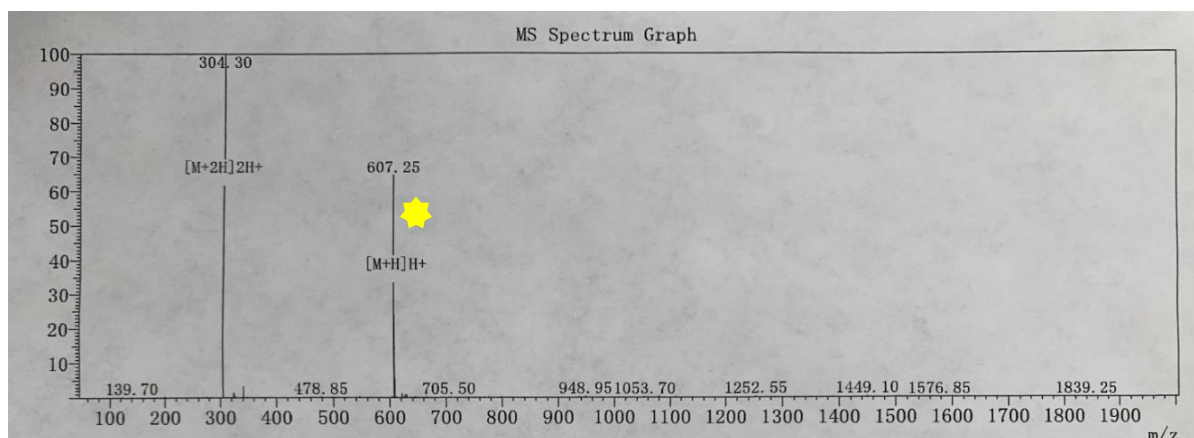


**Figure 3-2.** Mass spectrum of GHK-Palmitic Acid. The parent peak to the far right (yellow star) indicates particle formation of 607 g/mol.

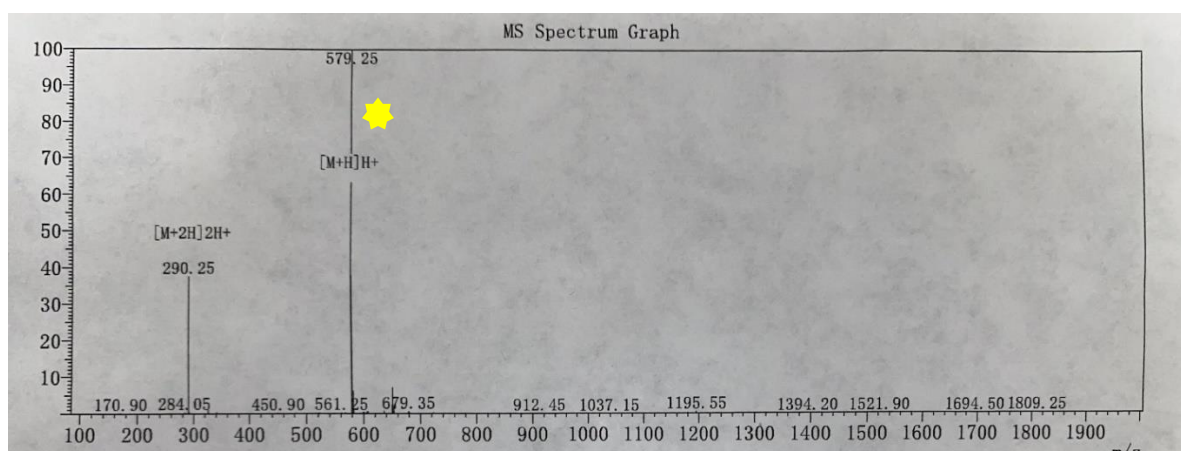


**Figure 3-3.** Mass spectrum of GHK-Steric Acid. The parent peak to the far right (yellow star) indicates particle formation at 579 g/mol.

**Table 3-2.** Purity levels of GHK, GHK-palmitic acid, and GHK-steric acid after HPLC.

Tripeptide	Purity	Formula	M.W.
GHK	98.74 %	C <sub>14</sub> -H <sub>24</sub> -N <sub>6</sub> -O <sub>4</sub>	340.1
GHK-P	98 %	C <sub>30</sub> -H <sub>54</sub> -N <sub>6</sub> -O <sub>5</sub>	578.25
GHK-S	99.45 %	C <sub>32</sub> -H <sub>58</sub> -N <sub>6</sub> -O <sub>5</sub>	606.6

### 3.3.2 HPLC

After MS was performed, reverse-phase high performance liquid chromatography (HPLC) was used to purify the tripeptides at levels greater than 98%, also indicated in **Table 3-2** (performed by LifeTien LLC). The spectrums in **Figures 3-4** to **3-6** designate a steady baseline with large peaks in the projected area over time. The area under the curve indicates the concentration of each tripeptide.

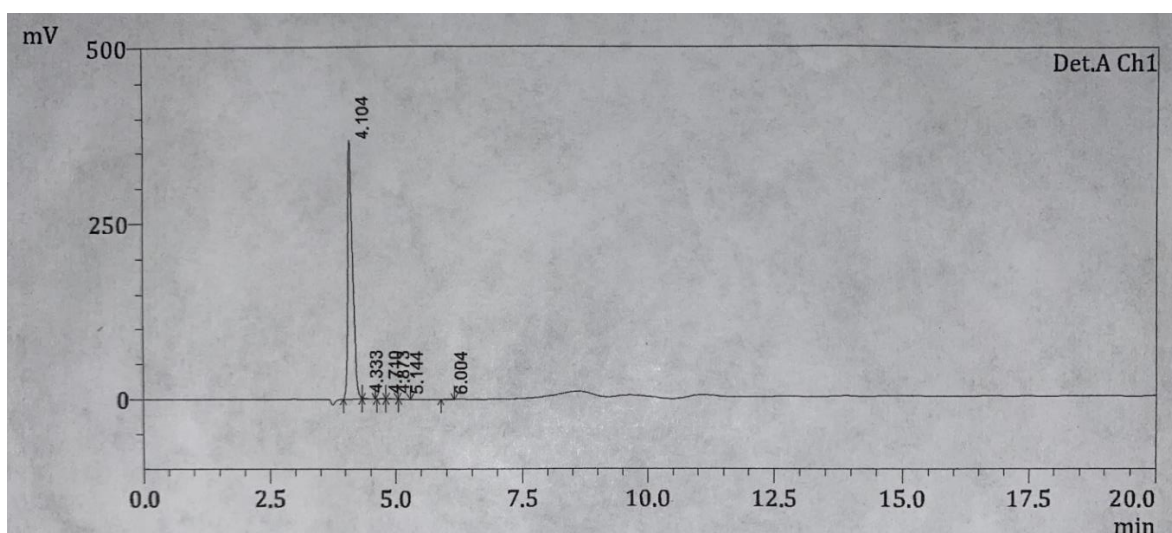


**Figure 3-4.** High performance liquid chromatography spectrum of GHK giving a 98.74% purity level.

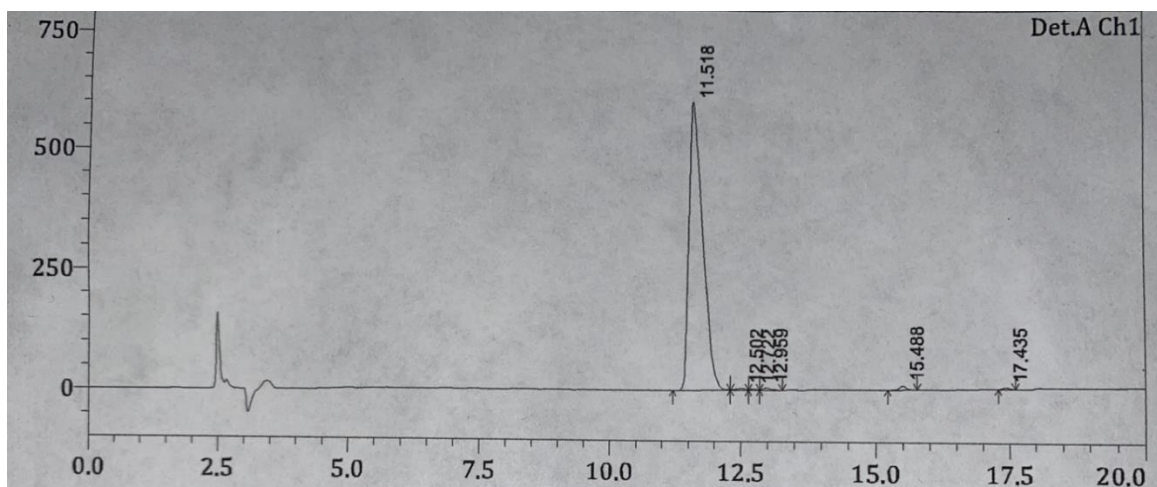


**Figure 3-5.** High performance liquid chromatography spectrum of GHK- palmitic acid giving a 98.0% purity level.

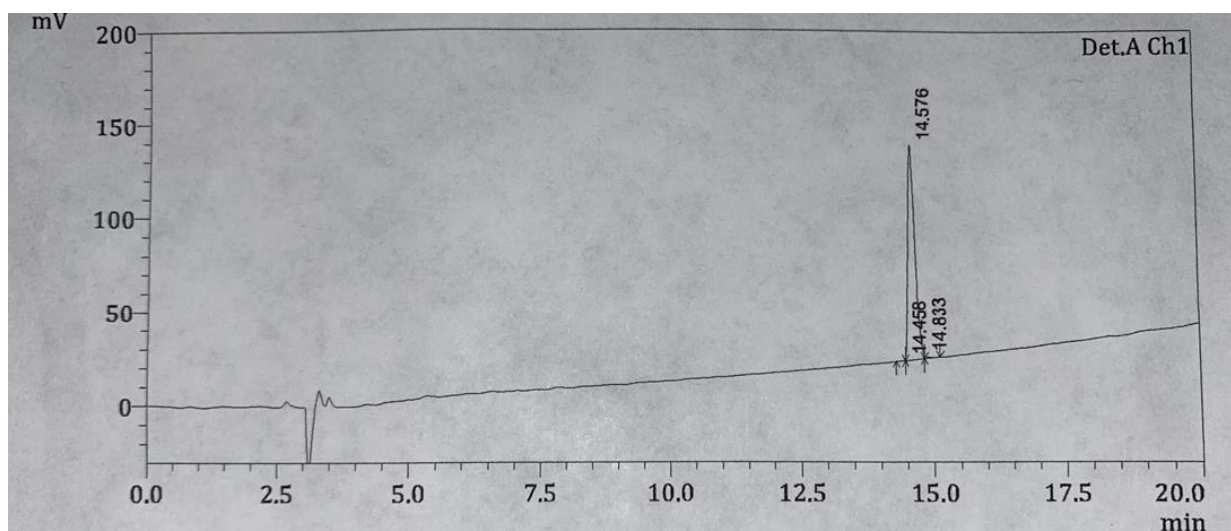


**Figure 3-6.** High performance liquid chromatography spectrum of GHK- Steric acid giving a 99.45% purity level.

### 3.3.3 SEM and EDS

SEM provided a visual representation of each nanoparticle. While SEM can help visualize particles at the micron and nano scales, analyzing biological molecules remains challenging because of the high energy beams produced by the apparatus. Coating biological molecules with thin layers of metal ions allows for better contrast to be generated by SEM<sup>78,79</sup>. However, coatings often distort molecules, especially biological molecules and amide bonds holding together amino acid sequences, as seen with GHK in **Figure 3-12**. The architecture of GHK produced abnormal spiky formations after being coated in silver with a 5-nanometer layer thick coating. GHKP and GHKS produced blurred images when getting down to the nano-level (**Figures 3-9 and 3-10**) but congregated flaky layers can be seen at the micron level for GHKS in **Figure 3-7**. The CuHNTs were identified as cylindrical nanotubes as expected from previous work done in the BioMorPH lab indicated in **Figure 3-13**, and when GHK was combined with

CuHNTs (**Figure 3-14**), spherical fragments can be seen attached to the surface of the CuHNTs indicating that GHK has reacted with the copper surface.

EDS confirmed essential elements of carbon, nitrogen, and oxygen within the tripeptide formations in **Table 3-3**, and **Figures 3-16** to **3-22** represent the spectral analysis of each tripeptide, CuHNTs, and GHKCuHNTs. **Figure 3-16** displays how the polymer tape, used to anchor down the nanomaterials, is comprised of carbon and oxygen. This is important to note because **Figure 3-21** and **3-22** shows carbon and oxygen displayed with the CuHNTs at high levels. Carbon and oxygen should not be observed with the CuHNTs.

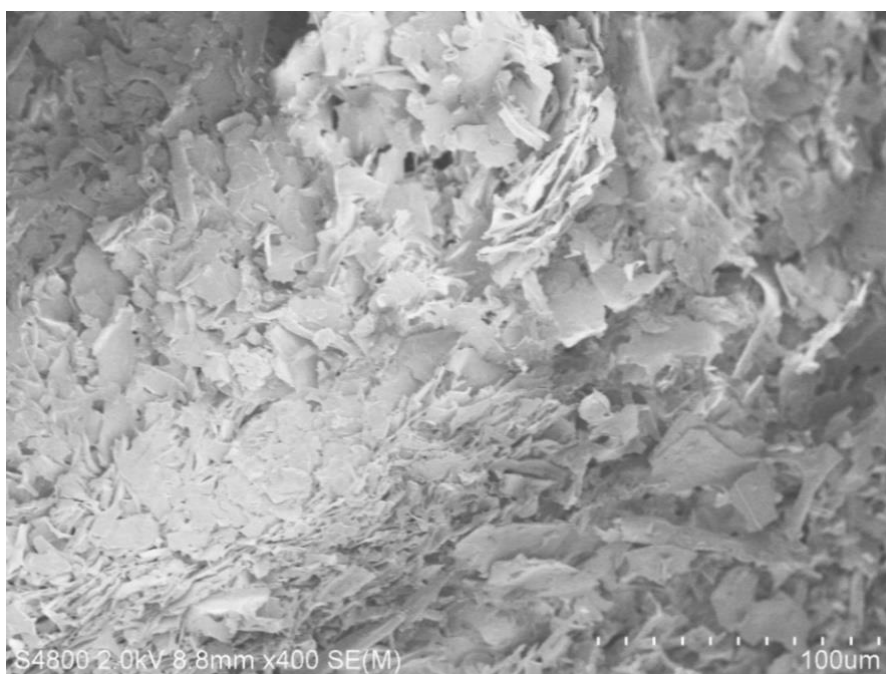


**Figure 3-7.** Scanning electron microscopy of GHK-Stearic acid at 400x and coated with silver at 5 nanometer thickness. Congregated flaky layers can be seen throughout the image.

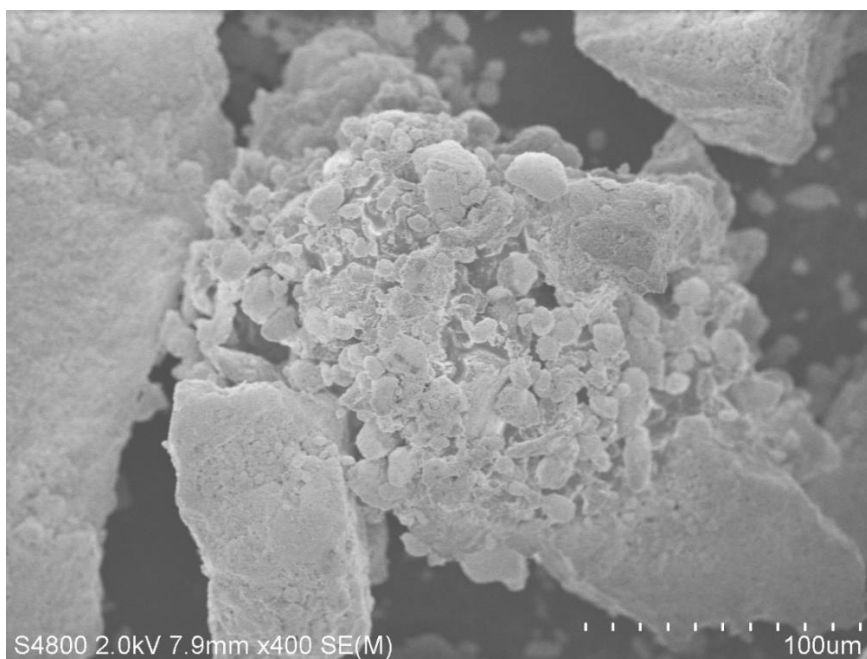


**Figure 3-8.** Scanning electron microscopy of GHKCuHNTs at 400x. The particles tend to clump together through charged interactions.

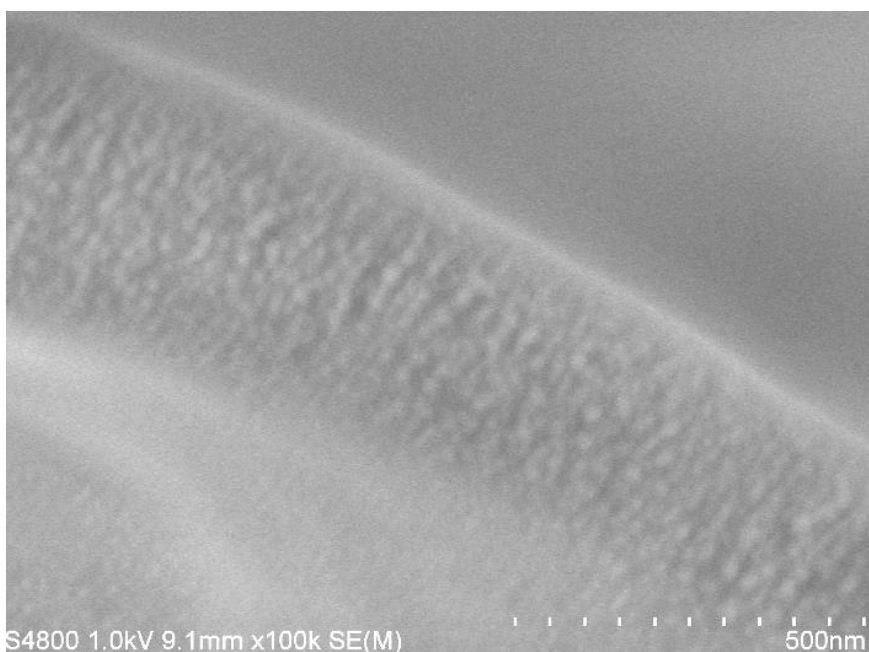


**Figure 3-9.** Scanning electron microscopy of GHK-palmitic acid at x100k and coated with silver at 5 nanometer thickness. The image contrast was still blurred after the coating process but spherical masses can be seen.

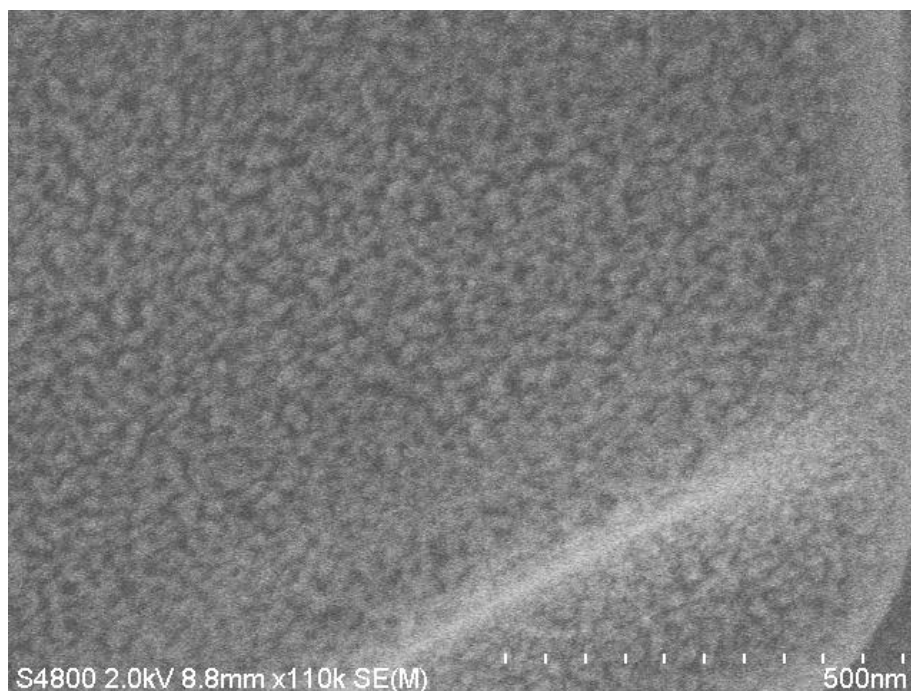


**Figure 3-10.** Scanning electron microscopy of GHK-stearic acid at x110k and coated with silver at 5 nanometer thickness. The image contrast was still blurred after the coating process but spherical masses can be seen.

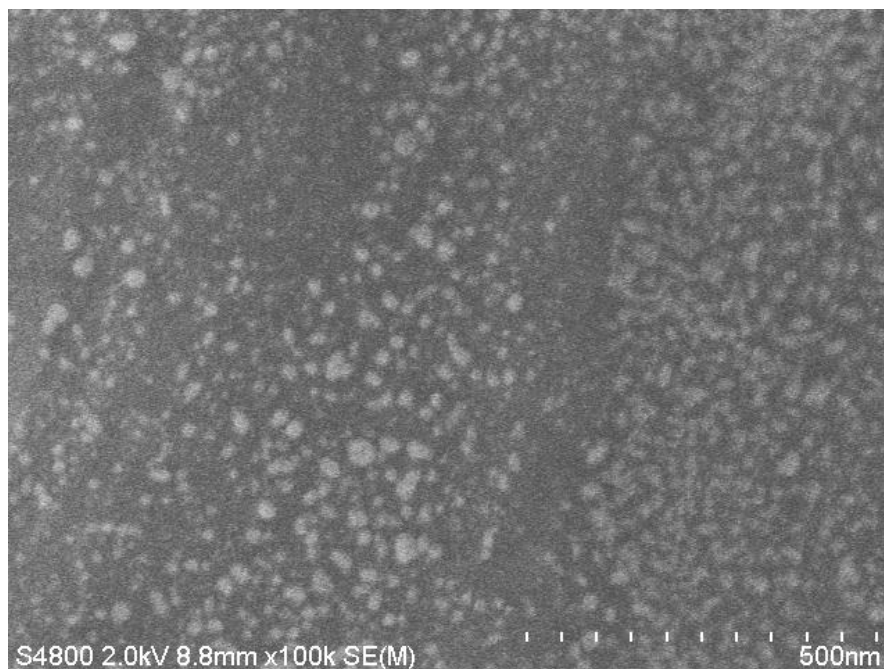


**Figure 3-11.** Scanning electron microscopy of GHK at x100k and coated with silver at 5 nanometer thickness. The images contrast was still blurred after the coating process but spherical masses can be seen.

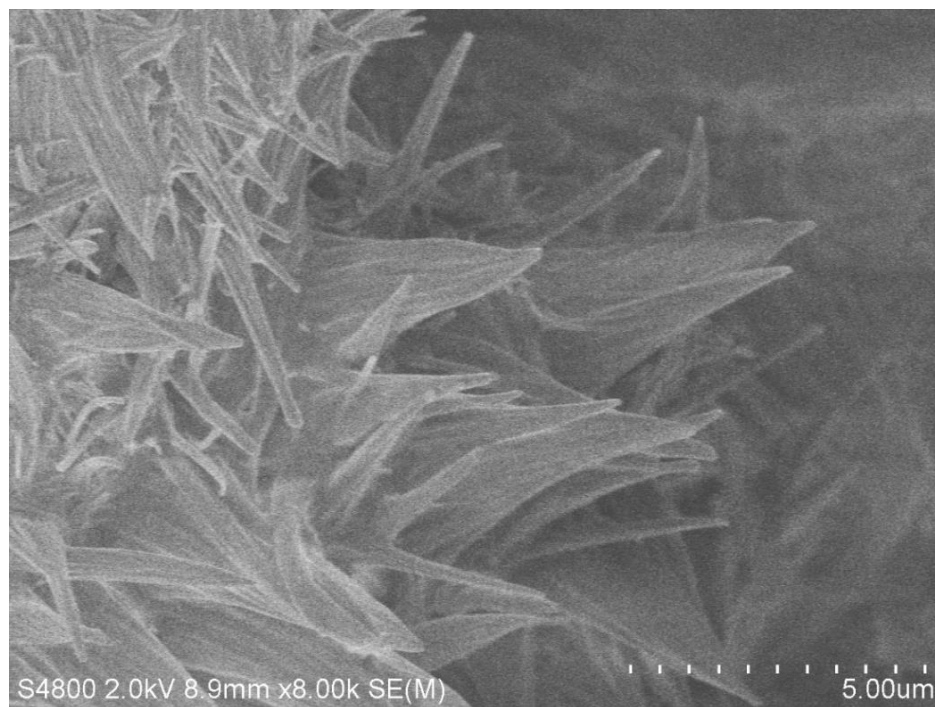


**Figure 3-12.** Scanning electron microscopy of GHK at 8000x and coated with silver at 5 nanometer thickness. Spiky projections were visualized after the coating process, suggesting GHK architecture was distorted.

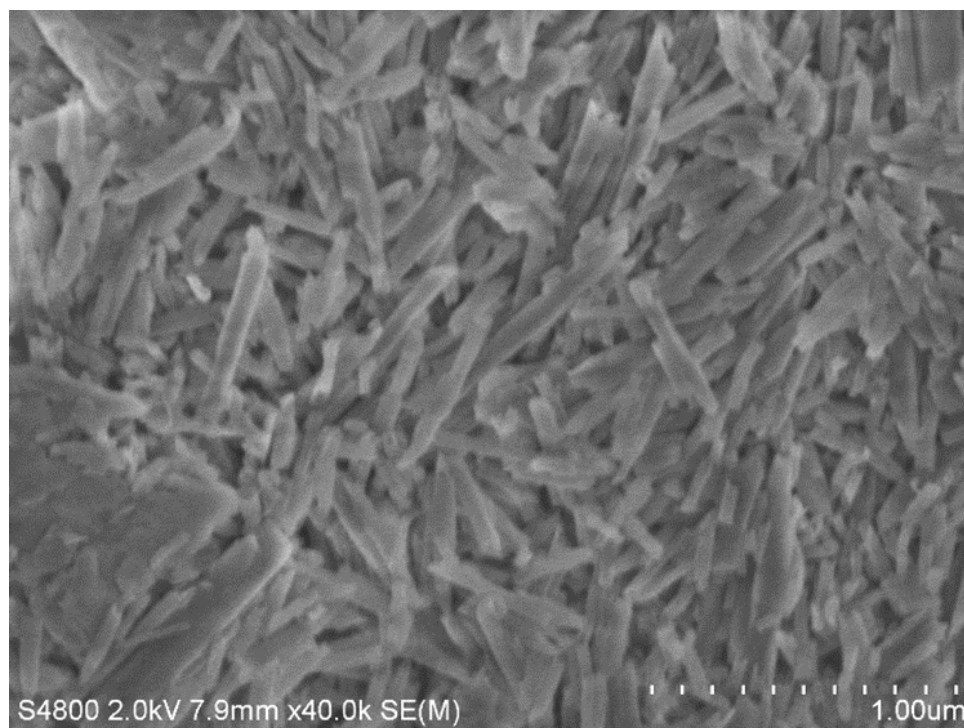


**Figure 3-13.** Scanning electron microscopy of CuHNTs at x40k. Cylindrical nanoparticles were visualized throughout the sample.

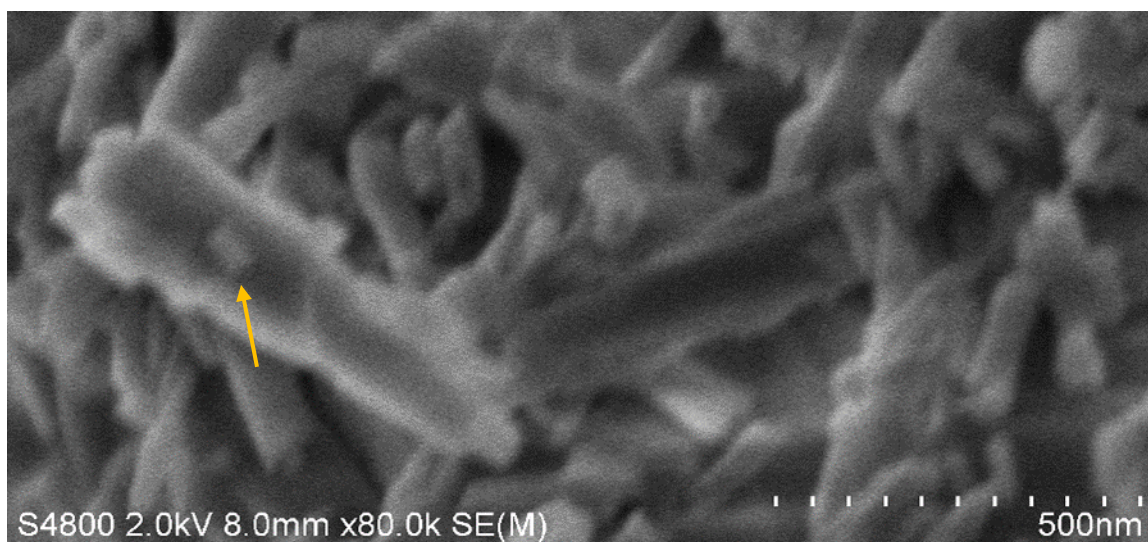


**Figure 3-14.** Scanning electron microscopy of GHKCuHNTs at x80k. Cylindrical nanoparticles are visualized and what appears to be GHK covalently attached (indicated by arrow).

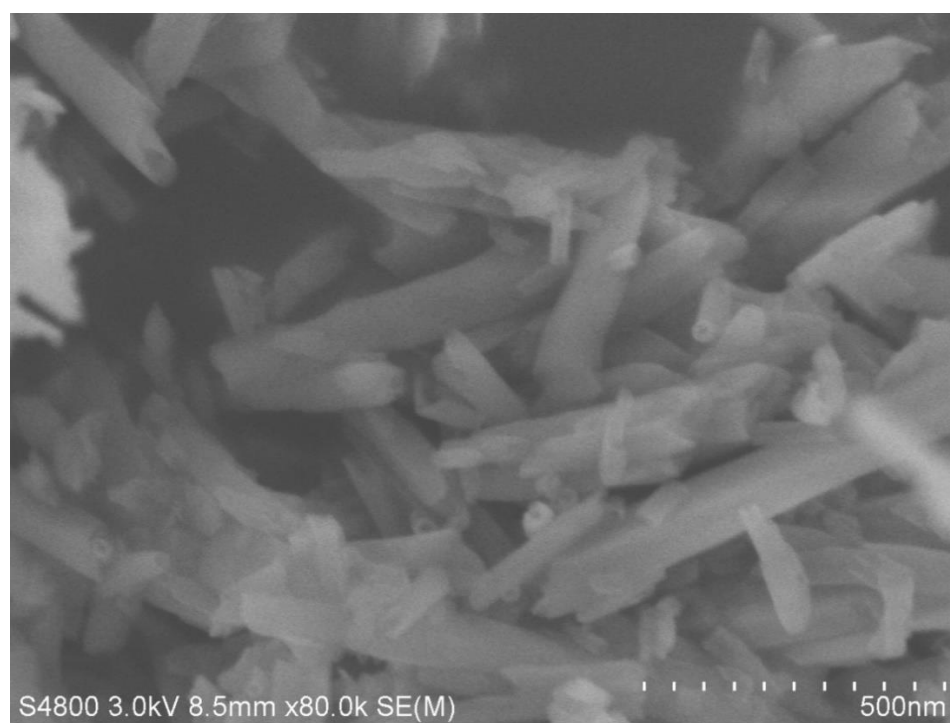


**Figure 3-15.** Scanning electron microscopy of GHKPCuHNTs at x80k. The blurred image cannot confirm the attachment of GHKP with the CuHNTs.

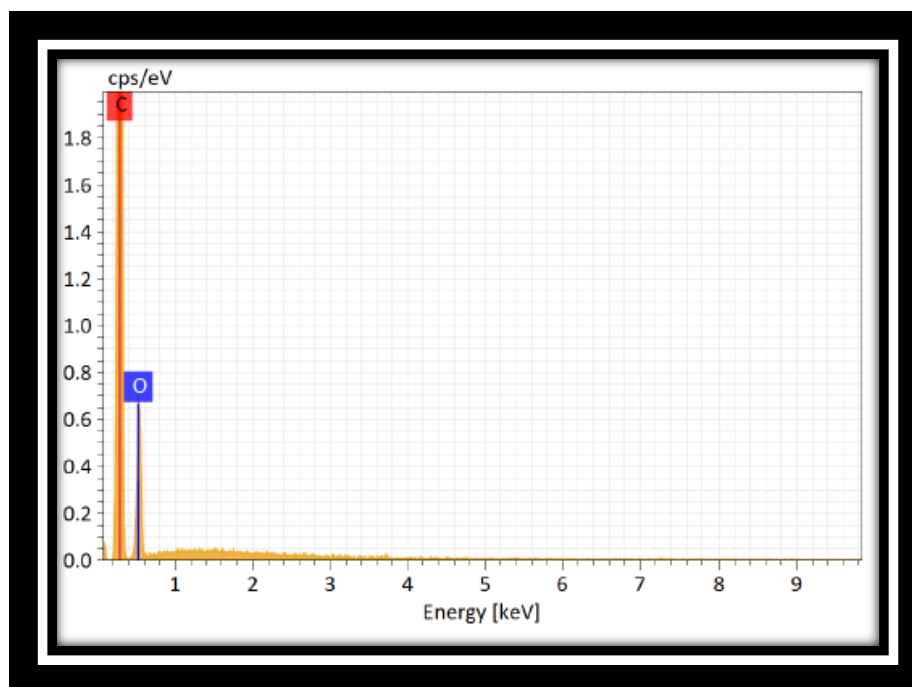


**Figure 3-16.** Electron dispersive X-ray spectroscopy confirming the presence of carbon and oxygen used within polymer tape of the EDS system.

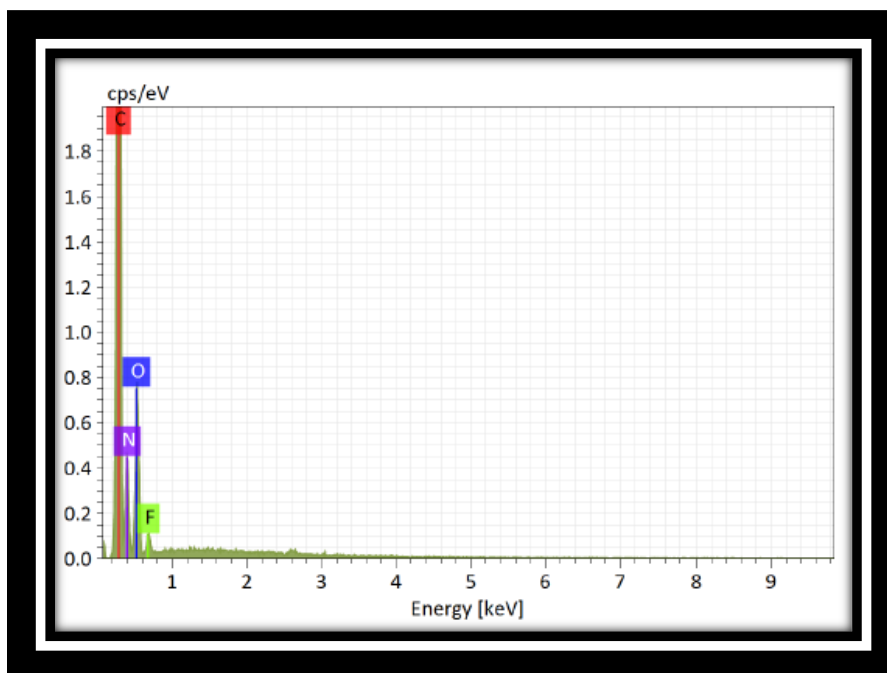


**Figure 3-17.** Electron dispersive X-ray spectroscopy confirming the presence of essential elements for amine and carboxyl groups for GHK. Slight peaks for fluorine were recorded.

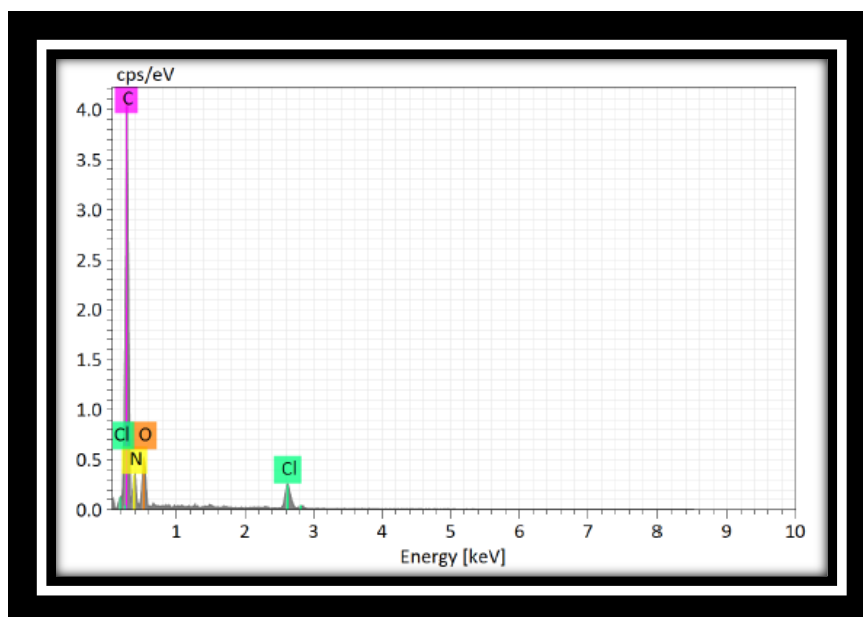


**Figure 3-18.** Electron dispersive X-ray spectroscopy confirming the presence of essential elements for amine and carboxyl groups for GHKP. Slight peaks for chlorine were recorded.

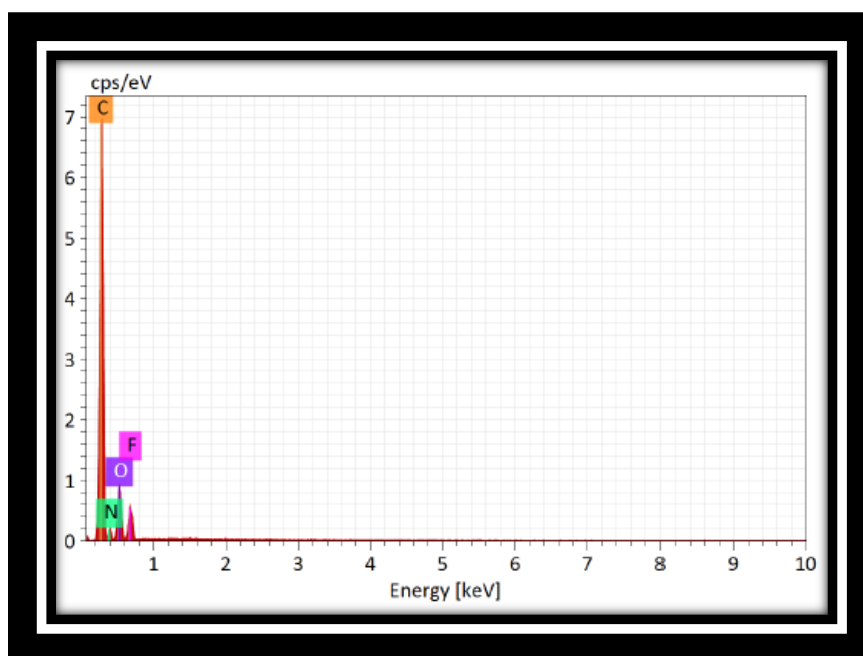


**Figure 3-19.** Electron dispersive X-ray spectroscopy confirming the presence of essential elements for amine and carboxyl groups for GHKS. Slight peaks for fluorine were recorded.

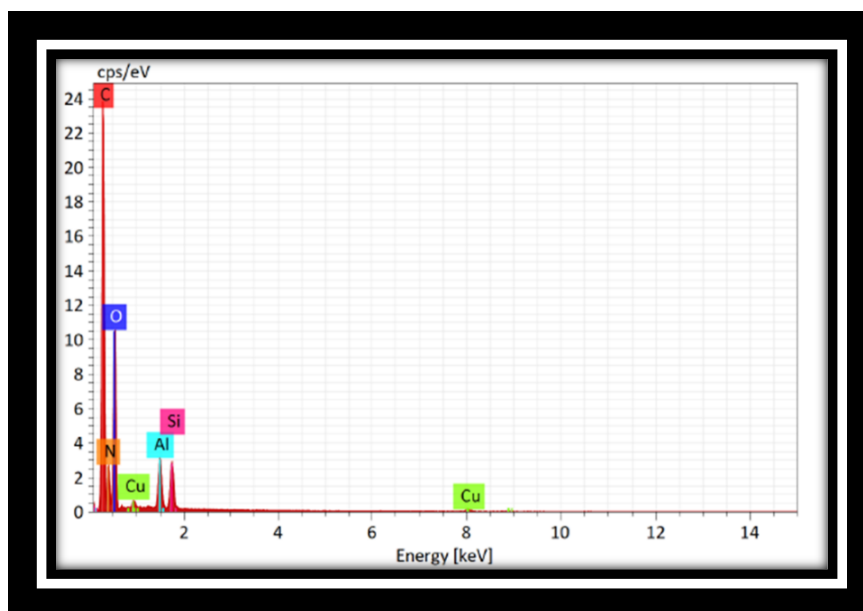


**Figure 3-20.** Electron dispersive X-ray spectroscopy confirming the presence of essential elements for amine and carboxyl groups along with copper and aluminosilicates in GHK/CuHNTs.

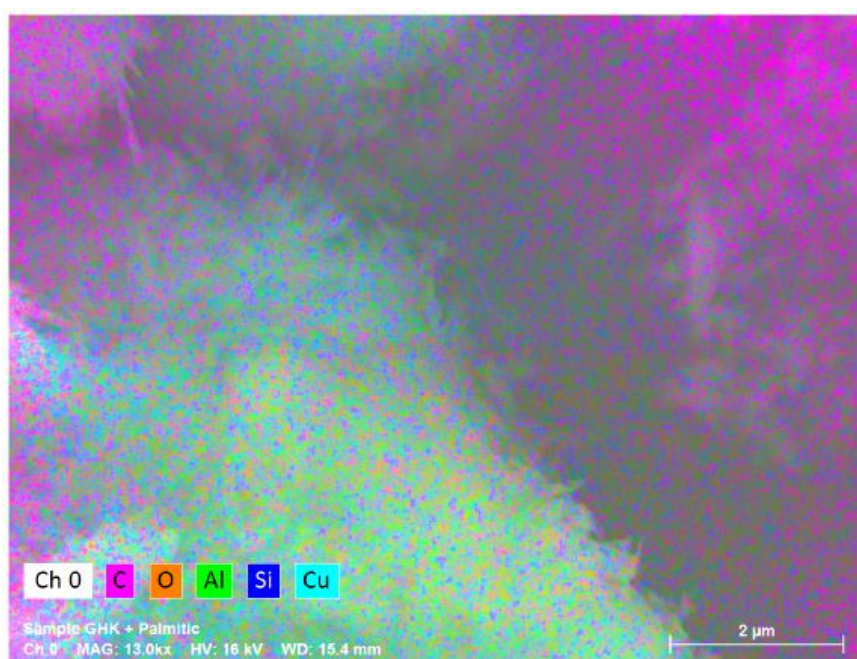


**Figure 3-21.** Electron dispersive X-ray spectroscopy colored micrograph of CuHNTs. Carbon and oxygen are picked up from the polymer-based tape used within the EDS system.

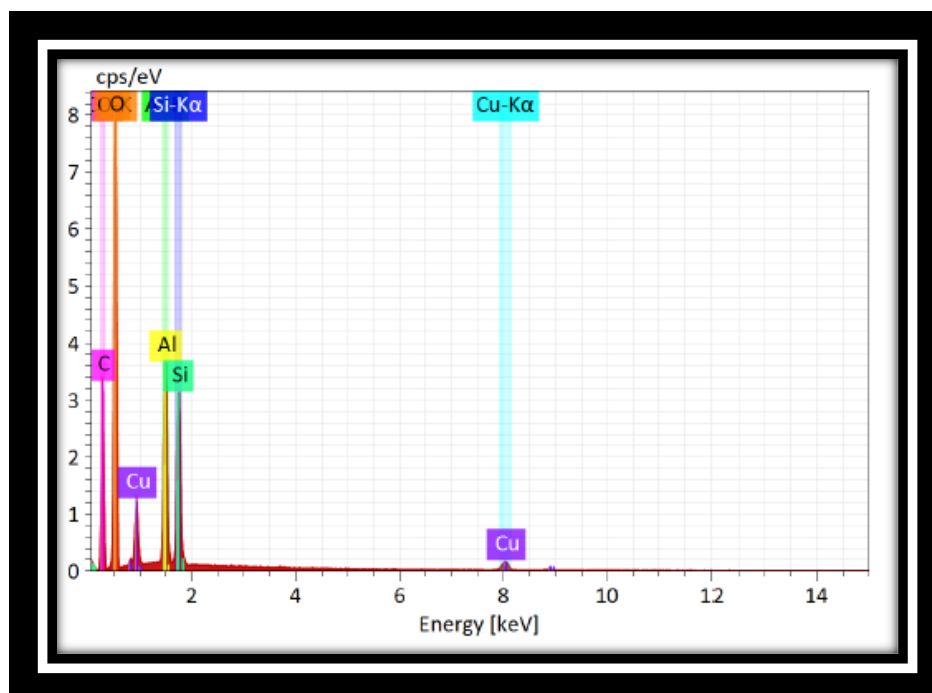


**Figure 3-22.** Electron dispersive X-ray spectroscopy confirming the presence of essential elements in CuHNTs.

**Table 3-3.** Elemental analysis confirming the presence of Carbon, oxygen, and nitrogen within GHK, GHK-Palmitic acid, and GHK-Stearic acid. Mass percentages and atom percentages are also given for each tripeptide. Larger amounts of Carbon are anticipated for GHKP and GHKS due to the extended fatty acid of palmitic acid and stearic acid conjugated to GHK, respectively.

Tripeptide	Element	Atomic #	Mass %	Atom %
GHK	Carbon	6	42.69	49.63
	Oxygen	8	24.63	21.49
	Nitrogen	7	18.58	18.52
GHKP	Carbon	6	65.67	67.11
	Oxygen	8	18.25	14.02
	Nitrogen	7	16.02	14.06
GHKS	Carbon	6	52.85	60.16
	Oxygen	8	21.73	18.57
	Nitrogen	7	11.61	11.34

### 3.3.4 Live/Dead Analysis

After characterization of each nanoparticle by EDS and SEM, a live/dead fluorescent stain, in biological triplicates, was performed to ensure that hASCs remained viable in culture after the nanomaterials were incorporated. Measurements were taken in the same region of each tissue culture plate. Media was changed every 3 days with the insertion of GHK, GHKP, or GHKS, along with combinations of SrHNTs or CuHNTs. Control samples did not have incorporated tripeptides or metalized HNTs and were grown in DMEM, 15% FBS, and 1% pen/strep only.

Cell viability-based assays with hASCs confirmed that 50 micromolar concentrations over a 28-day growth period for incorporated metalized halloysites and halloysites with tripeptides created ideal conditions for cellular growth and attachment. In addition, cell viability remained above 90% for all samples after immunofluorescent imaging and cell counting using a Cytation 5 cell imaging plate reader as indicated in **Figures 3-23 to 3-27**. Phase contrast imaging in **Figure 3-28** further confirms cellular attachment of SrHNTs with hASCs as indicated by the arrows within the figure. Large cellular clusters firmly attach around the SrHNTs with long filopodia also observed throughout the phase contrast image, suggesting that the hASCs are migrating across the culture plate.

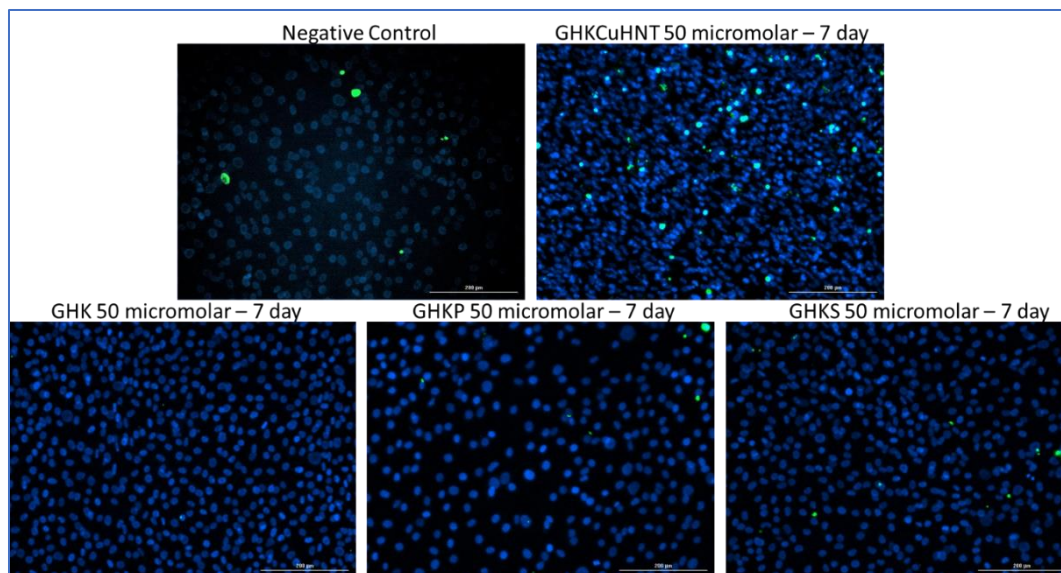


**Figure 3-23.** Immunofluorescent overlay images of GHK, GHK-P, GHK-S, and control group after 7 days in culture. Live nuclei are stained blue. Dead cell debris is stained green; n=3.

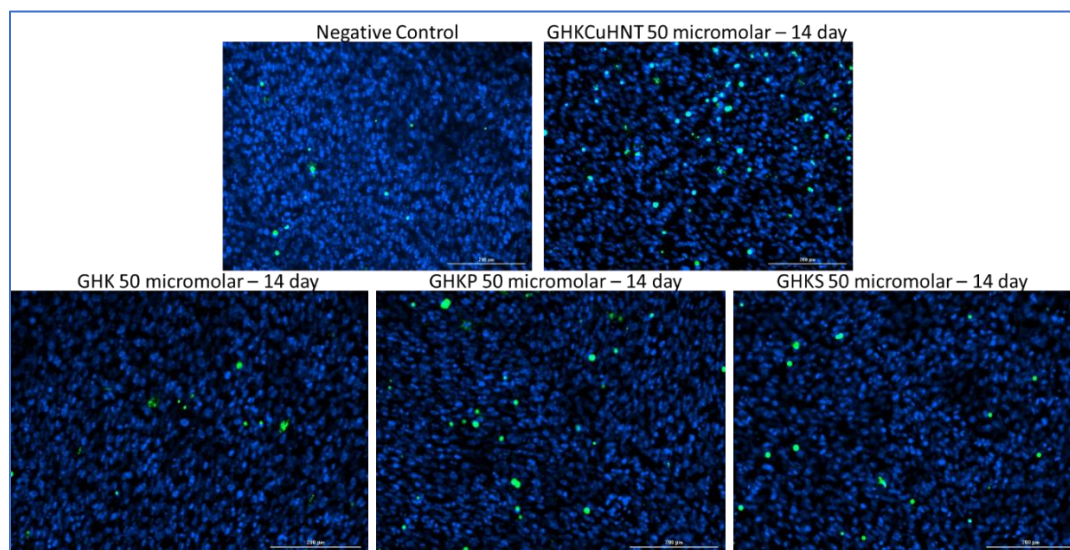


**Figure 3-24.** Immunofluorescent overlay images of GHK, GHK-P, GHK-S, and control group after 14 days in culture. Live nuclei are stained blue. Dead cell debris is stained green; n=3.

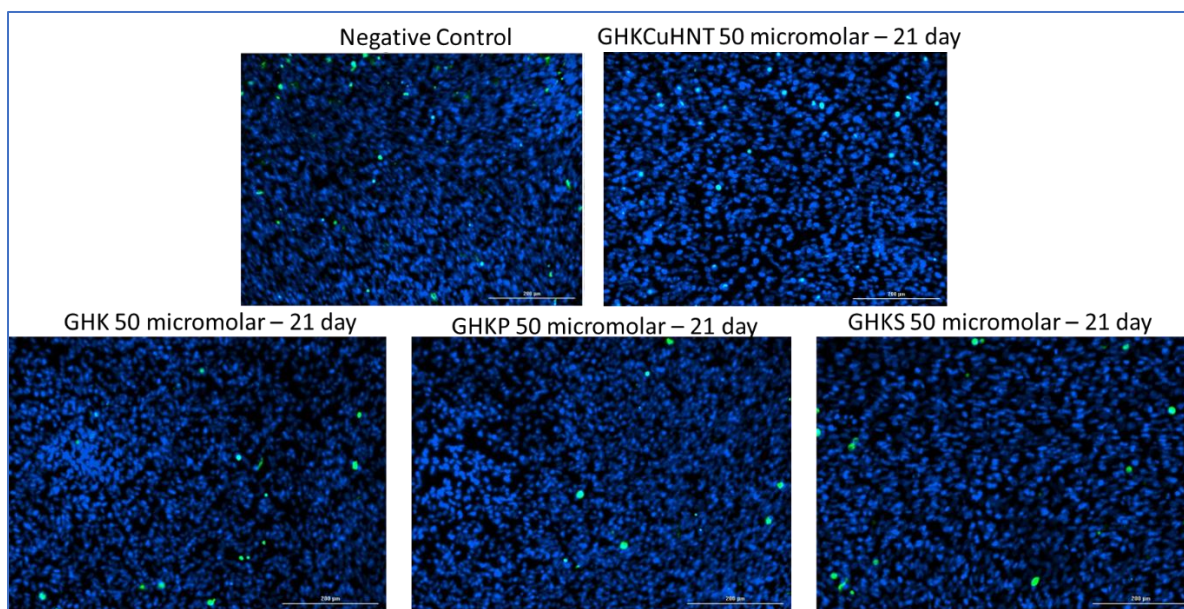


**Figure 3-25.** Immunofluorescent overlay images of GHK, GHK-P, GHK-S, and control group after 21 days in culture. Live nuclei are stained blue. Dead cell debris is stained green; n=3.

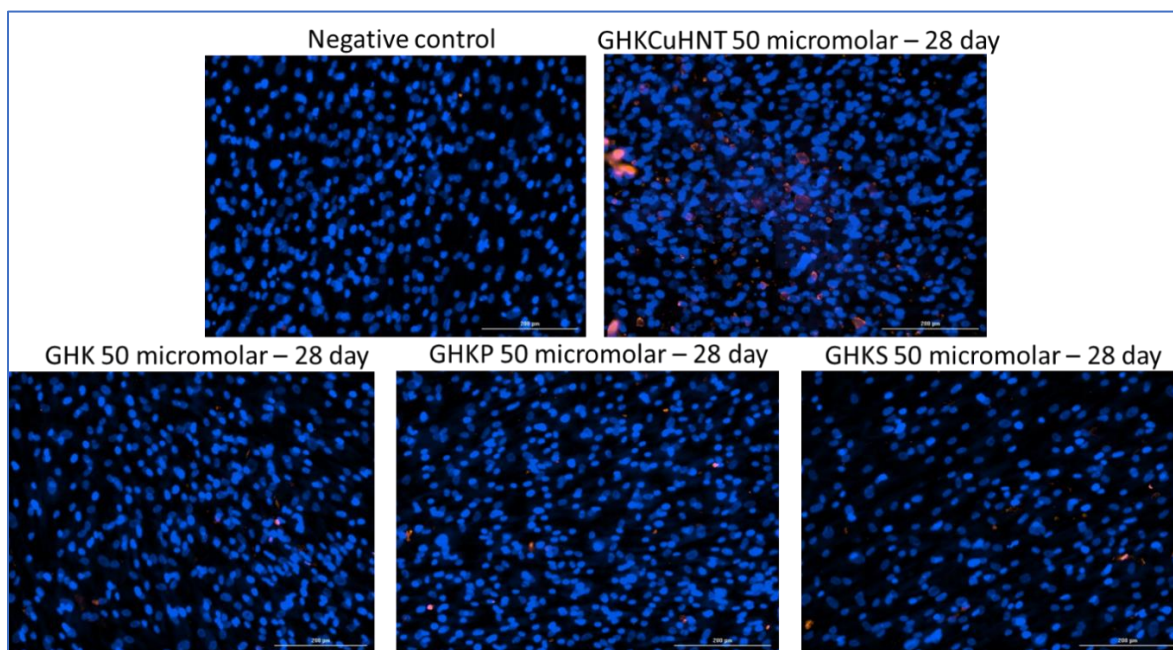


**Figure 3-26.** Immunofluorescent overlay images of GHK, GHK-P, GHK-S, and control group after 28 days in culture. Live nuclei are stained blue. Dead cell debris is stained green; n=3.

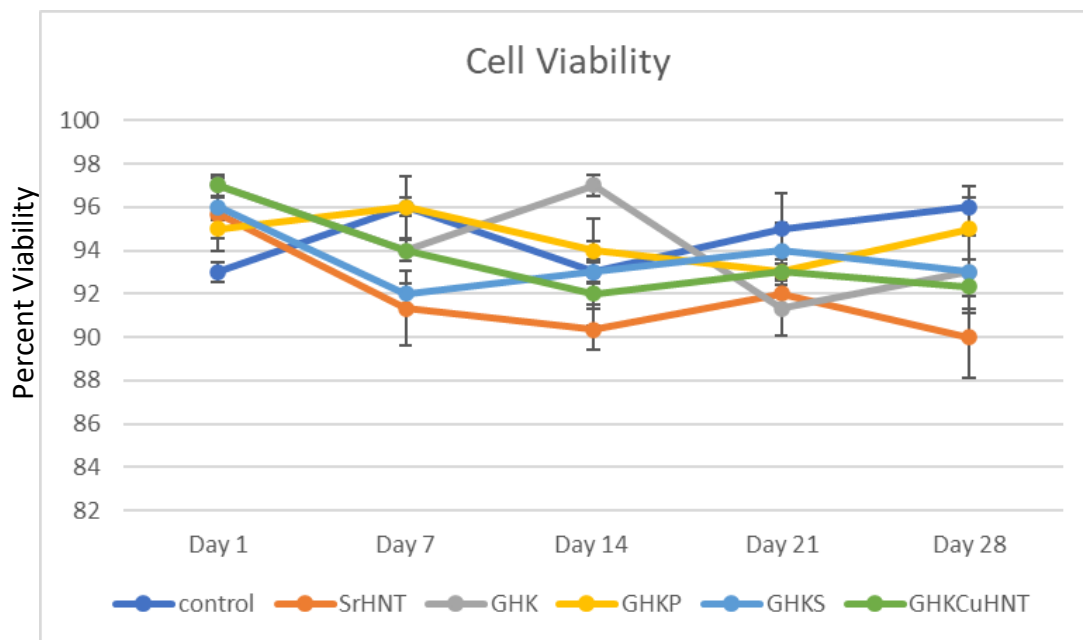


**Figure 3-27.** Cell viability observed over the course of 28 days after nanomaterials were incorporated at 50 micromolar concentrations; n=3. Images were taken from 3 separate plates within the same region.

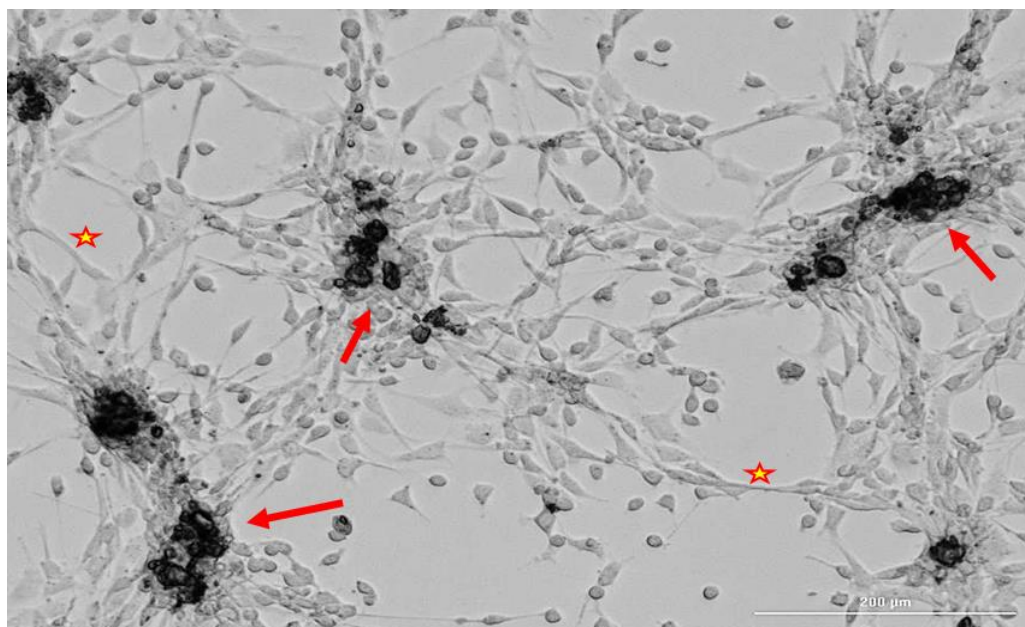


**Figure 3-28.** Phase contrast image of hASCs after 7 days in culture exposed to SrHNTs. Cells have attached and are migrating across the culture surface (note the long filopodia, red stars) clusters of cells (red arrows) were also observed.

### 3.3.5 Gene Expression

The impact of GHK was quantitatively assessed through quantitative reverse transcriptase-polymerase chain reaction (qRT-PCR). RNA was extracted using TRIzol, followed by the synthesis of cDNA. Evaluation carried out by qRT-PCR assessed mRNA expression from each sample collected, and *gapdh* served as the loading control to ensure that mRNA concentration is consistent for each sample. *Ki67* is a gene specifically transcribed in proliferation only, giving us a good indication of increased or decreased proliferation with SrHNTs, GHK, GHKP, GHKS, and CuHNTs incorporated with each tripeptide. The marker *runx2* is a transcription factor necessary early in bone differentiation and was used to assess if the nanomaterials enhanced the process of bone formation. Osteopontin is associated with osteoclast attachment to the mineralized bone matrix, and this is a late-stage considered marker in bone cell differentiation. Results for gene expression are displayed in **Figures 3-29 to 3-41**.

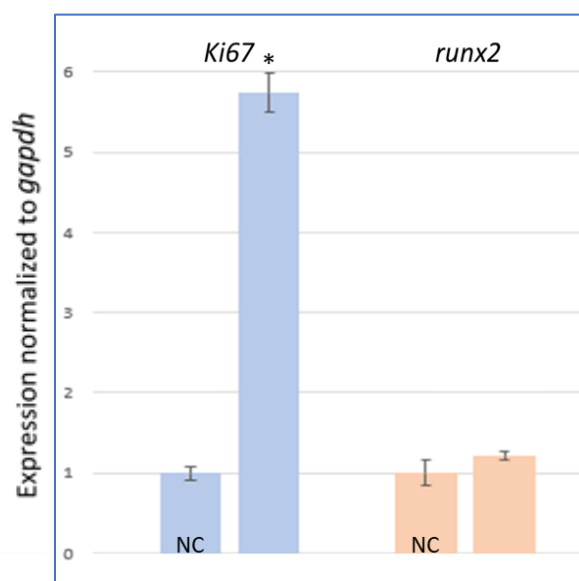


**Figure 3-29.** Increased expression of *Ki67* after SrHNT Exposure for 7 days. Expression was normalized to *gapdh*.  $P < .05^*$ ;  $n=3$ . Error bars represent  $\pm$  standard error. NC denotes the negative control.

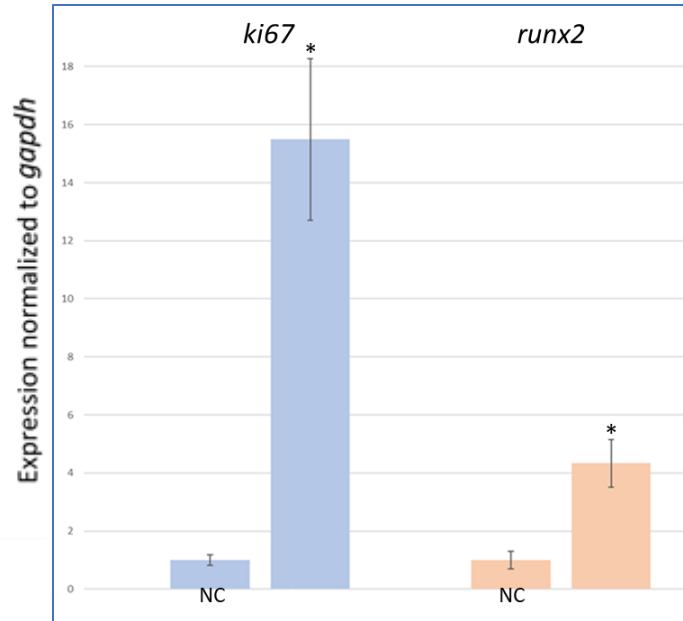


**Figure 3-30.** Increased expression of *Ki67* and *runx2* after SrHNT Exposure for 14 days. Expression was normalized to *gapdh*.  $P < .05^*$ ;  $n=3$ . Error bars represent  $\pm$  standard error. NC denotes the negative control.

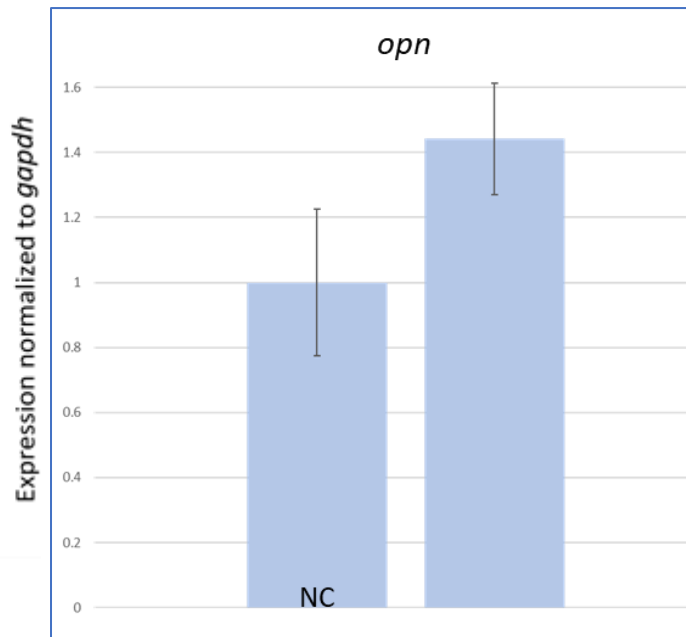


**Figure 3-31.** No significant difference in *osteopontin* were observed after SrHNT exposure for 14 days. Expression was normalized to *gapdh*.  $P < .05^*$ ;  $n=3$ . Error bars represent  $\pm$  standard error. NC denotes the negative control.

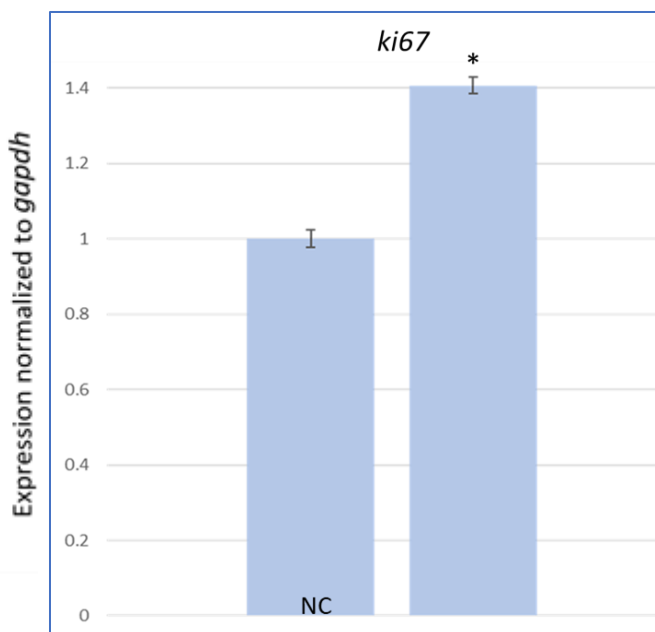


**Figure 3-32.** Increased expression of *Ki67* after GHKCuHNT Exposure for 24 hours. Expression was normalized to *gapdh*.  $P < .05^*$ ;  $n=3$ . Error bars represent  $\pm$  standard error. NC denotes the negative control.

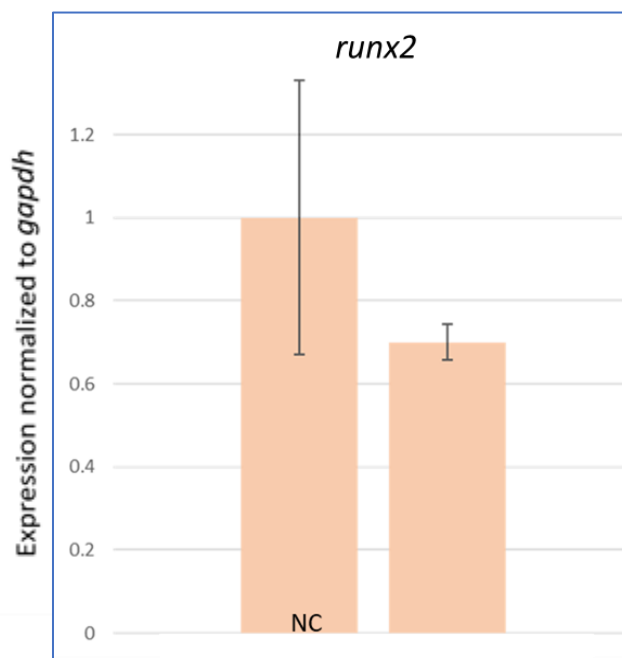


**Figure 3-33.** There was no significant impact on *runx2* after GHKCuHNT exposure for 24 hours. Expression was normalized to *gapdh*.  $P < .05^*$ ;  $n=3$ . Error bars represent  $\pm$  standard error. NC denotes the negative control.

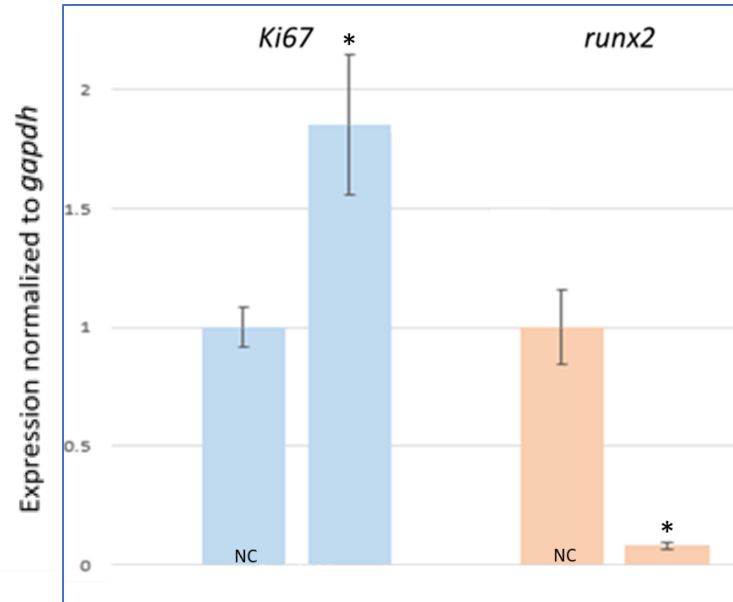


**Figure 3-34.** An increased expression of *ki67* and decreased expression of *runx2* was observed after GHK exposure at 50 micromolar for 7 days. Expression was normalized to *gapdh*.  $P < 0.05^*$ ;  $n=3$ . Error bars represent  $\pm$  standard error. NC denotes the negative control.

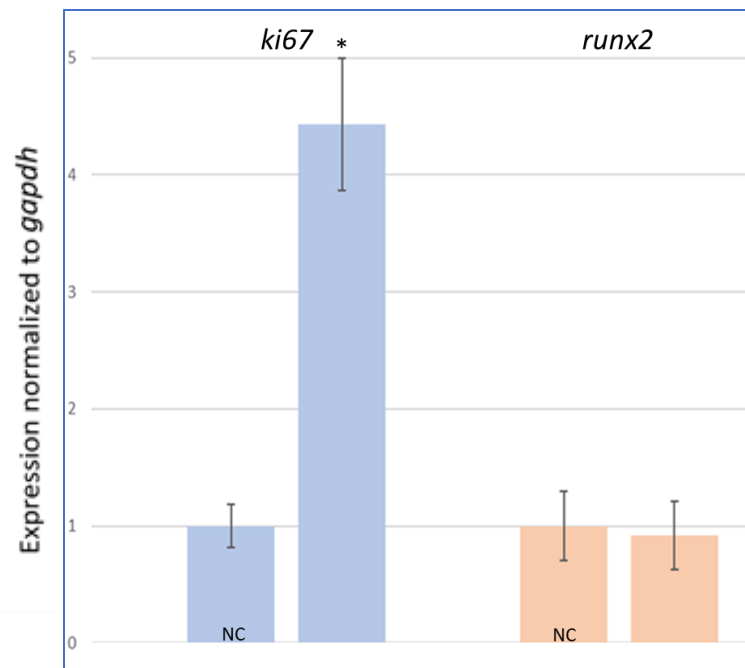


**Figure 3-35.** Increased expression of *ki67* after GHK exposure at 50 micromolar was observed for 14 days.  $P < 0.05^*$ ;  $n=3$ . Expression was normalized to *gapdh*. Error bars represent  $\pm$  standard error. NC denotes the negative control.

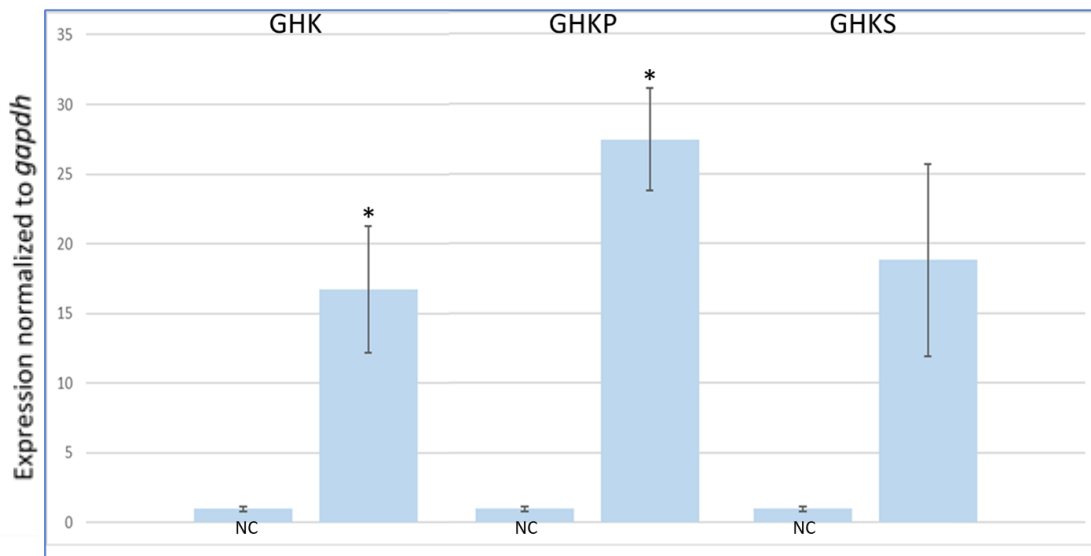


**Figure 3-36.** Increased expression of *ki67* after GHK, GHKP, and GHKS exposure at 50 micromolar for 14 days.  $P < 0.05^*$ ;  $n=3$ . Expression was normalized to *gapdh*. Error bars represent  $\pm$  standard error. NC denotes the negative control.

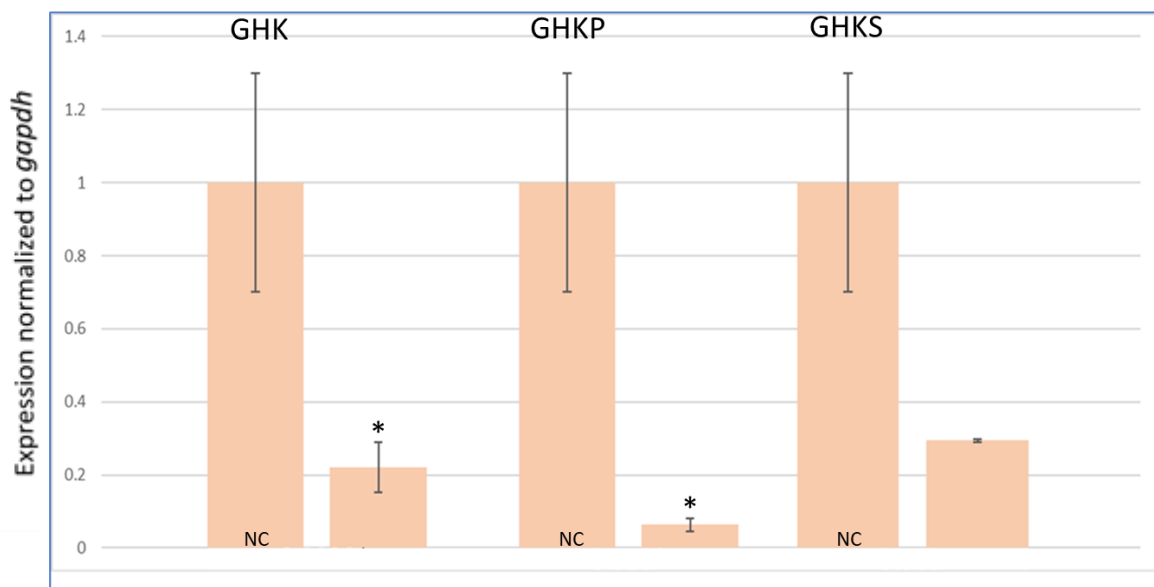


**Figure 3-37.** A. decreased expression of *runx2* was observed after GHK, GHKP, GHKS exposure at 50 micromolar for 14 days.  $P < 0.05^*$ ;  $n=3$ . Expression was normalized to *gapdh*. Error bars represent  $\pm$  standard error. NC denotes the negative control.

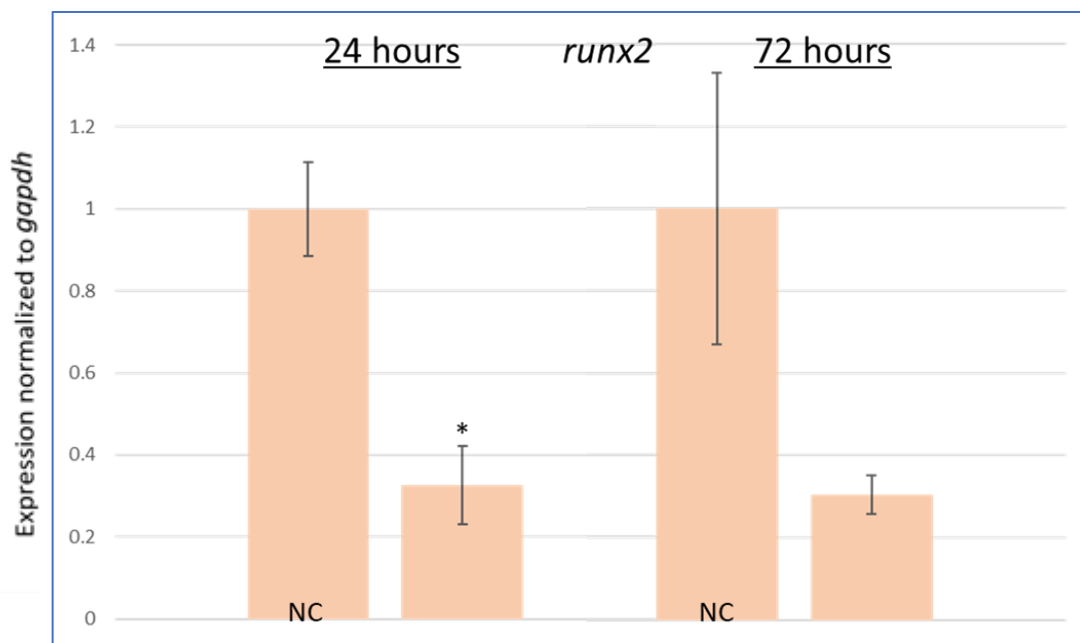


**Figure 3-38.** Decreased expression of *runx2* after exposure to GHKS-CuHNT at 50 micromolar for 24 hours.  $P < 0.05^*$ ;  $n=3$ . Expression was normalized to *gapdh*. NC denotes the negative control.

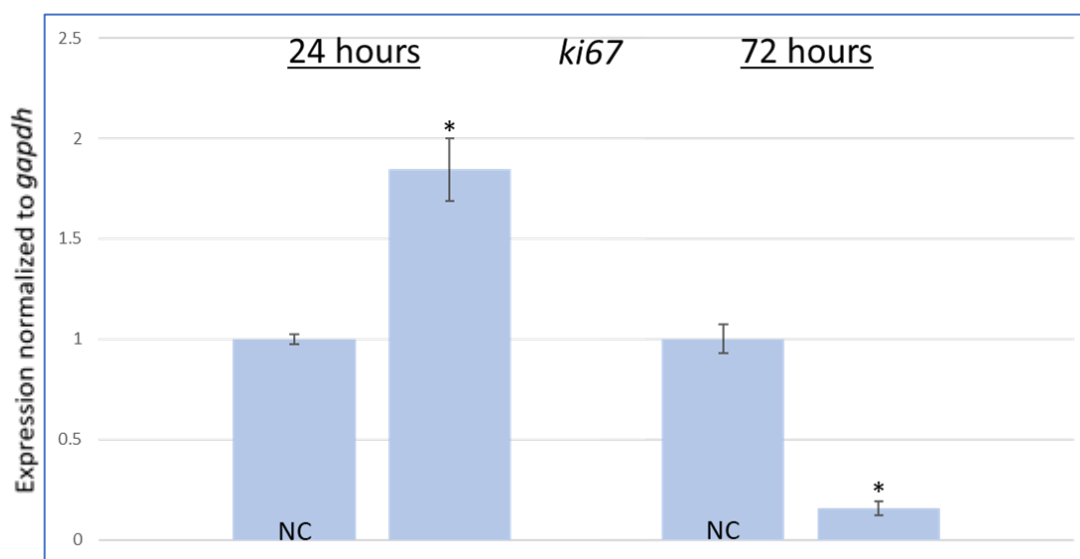


**Figure 3-39.** Increased expression of *ki67* after exposure to GHKS-CuHNT at 50 micromolar.  $P < 0.05^*$ ;  $n=3$ . Expression was normalized to *gapdh*. NC denotes the negative control.

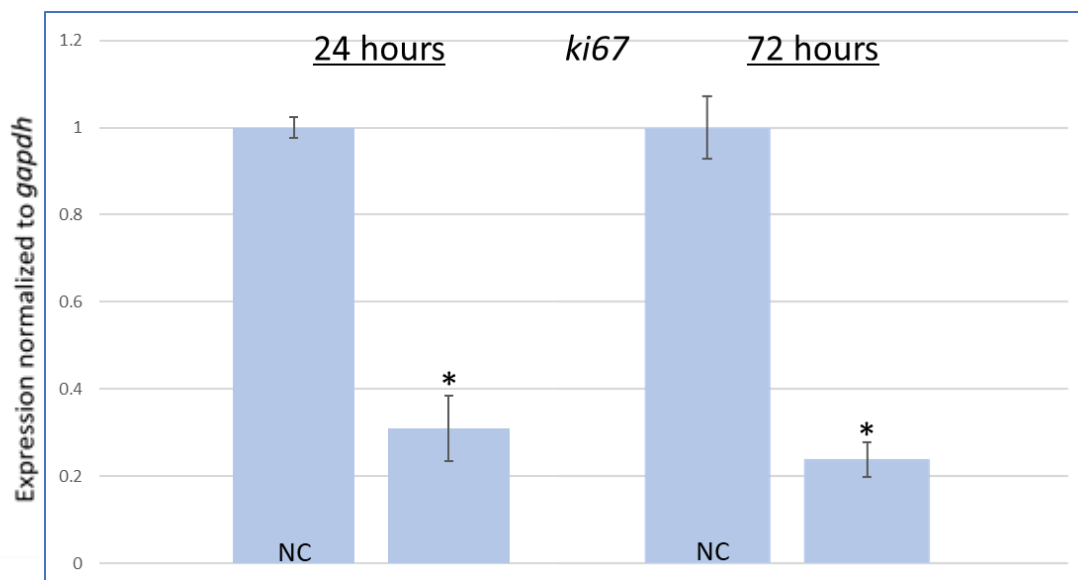


**Figure 3-40.** Increase in expression of *ki67* after exposure to GHKP-CuHNT at 50 micromolar.  $P < 0.05^*$ ;  $n=3$ . Expression was normalized to *gapdh*. NC denotes the negative control.

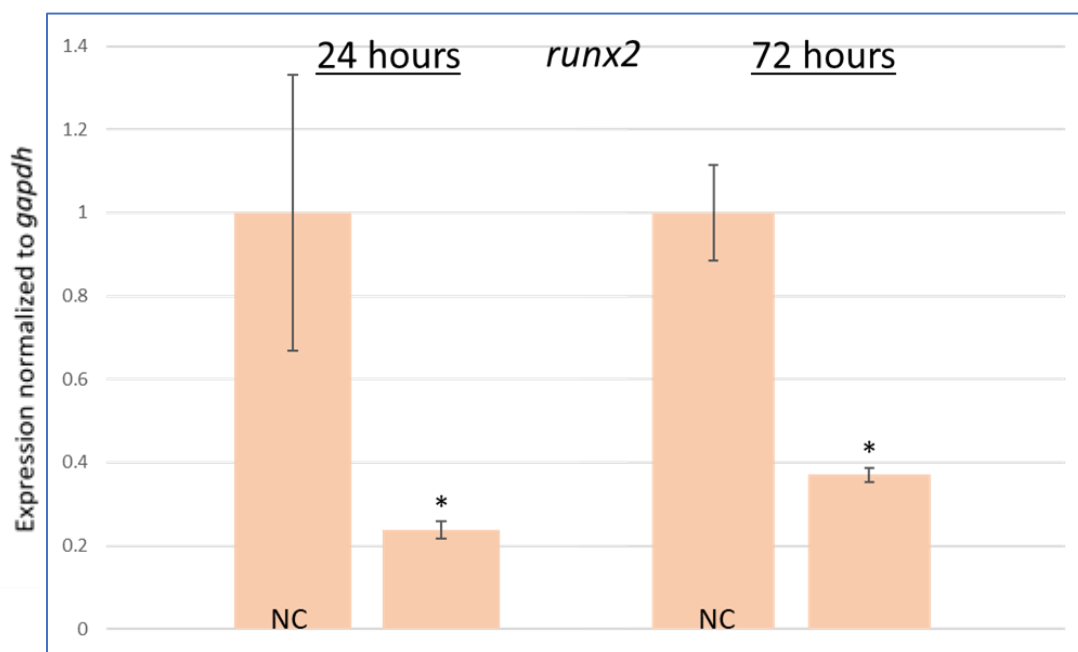


**Figure 3-41.** Increase in expression of *runx2* after exposure to GHKP-CuHNT at 50 micromolar.  $P < 0.05^*$ ;  $n=3$ . Expression was normalized to *gapdh*. NC denotes the negative control.

### 3.4 Discussion and Conclusion

#### 3.4.1 Particle Formation and Analysis

Mass spectroscopy (MS) first confirmed the different-sized peptide formations of the tripeptides incorporated into cell-based studies. The parent peaks on the far right of each MS spectrum confirmed the presence of the anticipated tripeptide. GHK was identified at 341 g/mol, GHK-P at 579 g/mol, and GHK-S at 607 g/mol. This result aligns with the theoretical values listed in **Table 3-2**. GHK was lipidized with steric acid and palmitic acid, thus increasing the molecular weight and overall size of the conjugated tripeptide. This result would yield a higher molecular weight as indicated by the mass spectrum. Palmitic acid is a 16-carbon fatty acid while steric is slightly larger at 18 carbons. Particle formation indicated that the conjugated tripeptides aligned with theoretical values as we would expect GHK-S to have the largest molecular weight.

The tripeptides were formed using 9-fluorenylmethyloxycarbonyl-chloride (Fmoc) method in solid-state synthesis. Fmoc is used as a temporary protecting group of the amino function in solid-phase synthesis of peptide chains, so side-chain derivatives are not formed in the process. Fmoc is removed after a series of washes to extract unbound amino acids before proceeding with synthesis. 2-Chlorotrityl chloride resin is employed to synthesize the C-terminal end, and the carboxyl group of the amino acid derivative attacks the methyl carbon. Chloride is the leaving group, which leads to the linkage of Fmoc-amino acids to the 2-chlorotrityl chloride resin. Generally, peptide synthesis used in the Fmoc process can lead to slight impurities with chlorine or fluorine for GHK, GHKP, and GHKS, leading to the 98% purities levels established after analysis by

EDS in **Figures 3-17 to 3-19**<sup>54</sup>. However, the peptides are added in solution to culture media, and this dilutes the impurities significantly and does not cause adverse functions of the formulated tripeptides.

High-performance liquid chromatography (HPLC) purified the peptide formations once particles were confirmed by mass spectrometry. Purity levels greater than 98% were achieved for GHK, GHK-P, and GHK-S as indicated in **Table 3-2**. EDS then confirmed particle formations by identifying elemental analysis of carboxyl and amine groups existing within the tripeptides. Given these considerations, it was suggested to move forward with cell-based culture studies to analyze how the nanoparticles influence the proliferation of hASCs and their capacity for tissue regeneration with *in vitro* models.

#### 3.4.2 Live/Dead Staining

Following particle formation, a live-dead analysis confirmed the biocompatibility of the tripeptides and mHNTs before moving forward with proliferation, gene expression, and wound analysis assays. Cell culture studies with hASCs over 28 days showed no significant cell viability changes as indicated in **Figures 3-23 to 3-27** after cells were counted on an automated cell counter. Cell viability percentages remained above 90% for SrHNT, GHK, GHKP, GHKS, and GHKCuHNTs over the course of 28 days. Immunofluorescence then qualitatively confirmed the biocompatibility of the nanoparticles over 28 days. The nucleus is stained using a fluorescent tag that binds to A-T rich regions in the nuclear DNA, known as Hoechst 33342 trihydrochloride Trihydrate, producing a deep blue. Acetoxymethyl ester is hydrolyzed by intracellular esterase's in the nucleus, confirmed the presence of live cells. A green or red dye

(propidium iodide) binds with dead cell debris present in the culture dish and cannot bypass intact cellular membranes.

### 3.4.3 Gene Expression

The application of SrHNTs had a significant increase in gene expression after 7 and 14 days for *ki67* and an increase of *runx2* after 14 days, while the late-stage marker *osteopontin* produced no significant increase after 14 days. Expression of *runx2* was expected to increase during the 14-day time frame with the incorporation of SrHNTs due to the prevalence of the ion in the bone formation process, and **Figure 3-30** confirmed our hypothesis. Although an increase in *ki67* represents proliferation taking place with the hASCs, the bone marker, *runx2*, is also differentially expressed and an early marker of bone differentiation, potentially activating downstream targets. The hASCs are proliferating and differentiating after exposure to SrHNTs, as they would at tissue-damaged sites if incorporated as bone implants. The bone formation process is often slow, though, with healing taking several months based often the severity of the injury and healing process through the inflammatory response, soft callus phase, hard callus phase, and the remodeling process<sup>80</sup>. The late-stage bone marker *osteopontin* was not significantly relevant as indicated in **Figure 3-31**, indicating that the hASCs are experiencing early phases of bone differentiation.

Furthermore, the process of gene expression in cell-based cultures is still poorly understood with the incorporation of nanoparticles, such as SrHNTs, that have yet to be used for potential medical implants. However, there are clear indications that SrHNTs can impact the bone formation process to speed recovery time in patients with

diminished bone growth, non-unions, or prolonged areas of trauma. 3D printed bone implants or calcium phosphates screws embedded with SrHNTs can play a role in bone development, especially in patients with osteoporosis, osteomyelitis, or even genetic-based pathologies seen in Alagille syndrome brachydactyly and spondylocostal dysostosis, and Hajdu Cheney syndrome<sup>81</sup>.

After assessing SrHNT effects in culture, gene expression analysis was performed on the CuHNTs complex formed with each tripeptide. Gene expression showed a reduction of *ki67* after only 3 days in culture (**Figures 3-38 to 3-41**), indicating a change from proliferation to differentiation into fibroblasts. The synergistic role of CuHNTs and SrHNTs produced different outcomes in comparison to the tripeptides alone. Both *ki67* and *runx2* were decreased with GHKPCuHNTs and GHKSCuHNTs, suggesting differentiation into a fibroblast morphology. However, other connective tissue pathways could be activated, such as muscle or cartilage, and would need additional studies to confirm.

Experiments incorporating GHK, GHKP, and GHKS indicated that hASCs were not differentiating into the bone lineage but were accelerating the proliferation process (**Figure 3-36 to 3-37**). After 14 days, GHK and GHKP exhibited over 15 times the normal expression of *ki67*. This rapid expression profile indicates hASCs response to the vascular endothelial growth factor pathway (VEGF). This primary response in tissue formation is necessary to stimulate platelet activation, adhesion, and platelet plug formation. The rise in *ki67* promotes hASCs proliferation in open wound systems while also promoting macrophages in adipose tissues<sup>82</sup>. Thus, the incorporation of GHK or

GHKP, under the right conditions, can stimulate VEGF response and immune homing capabilities.

The extended fatty acid chain on GHKP or GHKS can contribute to phospholipid bilayer formation, receptor binding, and extend the half-life of GHK for the stimulation of growth pathways in open wound systems. Additionally, stearic acid binding with fatty acid binding protein E-(FABP)/retinoid acid receptor has already been shown to mediate differentiation of CD11c+ macrophages in obese individuals<sup>83</sup>. Given that stearic acid can bind to FABP, both palmitic acid and stearic acid can bind with this particular receptor on hASCs or immune cells in tissue damaged sites to promote immune homing of macrophages at tissue damaged sites.

### **3.5 Future Studies**

The incorporation of tripeptides with metalized halloysites for tissue regeneration needs additional studies using open wound systems. Gene expression results indicated that GHK and the conjugated forms with fatty acids played a fundamental role in manipulating how hASCs respond in an *in vitro* model. However, widespread RNA-sequencing would be an ideal approach towards further understanding the influence of GHK and mHNTs on differentiating hASCs into other cell lineages such as myogenesis, chondrogenesis, and neurogenesis.

Protein expression analysis is a fundamental next step to build on gene expression results. The analysis of Ki67 and Runx2 through western blot would confirm direct protein management of GHK in hASCs. Once protein expression studies are carried out, this will advance studies into animal models as this is necessary before

moving to human-based studies. Prototypes bandages can be constructed using blow-spun Polylactic acid (PLA) fibers with mHNTs and coated with tripeptides and/or fatty acids for enhancing wound site recovery.

CuHNTs with GHK, GHKP, and GHKS, incorporated into blow-spun or electrospun fibers, and applied to wound healing studies, would provide insight into their role in the healing process. Electrospun or blow spinning methods will allow for equal distribution of our newly formed nanocomposites throughout the fibers, increasing cellular interactions. In addition, applying the nanoparticles to commercially available FDA-approved materials is an ideal application to enhance characteristics on proliferation and biocompatibility. Several preliminary studies have been completed with metalized HNTs, GHK, GHK conjugated to fatty acids, GHK bound with coppered halloysites, and gene expression results indicate a desirable use of them for open wound systems.

## **CHAPTER 4**

### **DETERMINING MIGRATORY PATTERNS AND ARTIFICIAL WOUND ANALYSIS**

#### **4.1 Introduction**

The addition of previously mentioned nanoparticles was added to cultures of hASCs to better understand the impact for wound healing applications. A scratch assay and migratory pattern analysis were performed to quantify if any influence on cell migration was enhanced. A p200 micropipette disrupted the cell monolayer for imitation of artificial wound closure with associated scratch assays. After 24 hours in culture, images were taken to analyze cell density and cell migration into the artificial wound site by the wound closure plugin for ImageJ. The scratch assay's control did not use nanomaterials or GHK derivatives, making it the baseline for comparison between experimental groups. Environmental constraints often decide a stem cell's fate, and the proliferation of cells into the artificial wound site elucidates wound healing capabilities.

A cell invasion assay was used to identify cell migration patterns within a transmembrane chamber. This assay consists of two chambers separated by a porous membrane with cells seeded in the top chamber. In contrast, the bottom chamber contains one of the previously mentioned nanomaterials acting as a chemoattractant.

The cells were incubated in the top chamber and allowed to migrate through the intervening porous membrane chamber at the bottom to assess the chemoattractant characteristics of the nanomaterials. If more hASCs migrate from the top chamber through the filter pores, we can be confident that the nanomaterials stimulate a homing response. Detection of cell invasion is quantified using immunofluorescent staining using Calcein AM solution. Cell dissociation/Calcein AM solution is placed in the bottom chamber to dissociate the filter's migrating cells. Free Calcein fluoresced brightly and was used to quantitate the number of cells passed through the transmembrane chamber.

Nanomaterials often display antimicrobial properties, especially metals, because of the oxidative states of ions in nature and their ability to penetrate the cell walls of prokaryotes<sup>24,25</sup>. Studying how mHNTs or naturally occurring tripeptides secreted in open wound systems is an important aspect to consider to enhance current wound healing applications. Ideally, the tripeptides will not promote the bacterial growth of gram-negative or gram-positive bacteria. We hypothesized that increased cell migration would occur with exposure to the incorporated nanomaterials while also enhancing antimicrobial attributes against *S. aureus* and *E. coli*.

The cell invasion and the scratch assay results will better indicate how hASCs respond and proliferate to the external environment and whether they play a role in homing capabilities. GHK is an ideal molecule to identify a potential role in advancing wound healing and at what concentrations and combinations of other biocompatible molecules influence cell migration.

## 4.2 Materials and Methods

### 4.2.1 Immunofluorescent Live/Dead Staining

The live nucleus was stained blue by using a fluorescent tag that binds to A-T rich regions in the nuclear DNA, known as Hoechst 33342 (2'-[4-ethoxyphenyl]-5-[4-methyl-1-piperazinyl]-2,5'-bi-1H-benzimidazole)(Cat. #A020A). Excitation and emission at 360/460 nanometers. Dead cells were probed with EasyProbes propidium iodide for red at excitation and emission 535/620 or EasyProbes Green at 490/520 (Cat. #A020B). The reading was performed on a Cytation 5 plate reader and cells were counted using the plate reader, and ImageJ software.

### 4.2.2 Alizarin Red Stain

After seeding, cells were stained with a 40 mM Alizarin Red S (ScienCell Cat. #8678a) staining kit at an interval of 7, 14, 21, and 28 days. Cells were stained with Alizarin Red S to determine if the cells were calcium-rich, indicating that the stem cells differentiated towards an osteoblast lineage. A positive control was used for comparison over the 28 day growth period (Gibco Cat. #A1007201). The pH of the Alizarin Red was adjusted to 4.2 before use with the 10% ammonium hydroxide or 10% acetic acid. Media was removed from each well, washed once, and cells were fixed with 500  $\mu$ l of 10% formalin/per well for 20 minutes at room temperature in a 24-well plate. The formalin was then removed, and each well was washed two times with 500  $\mu$ l distilled water. 500  $\mu$ l of Alizarin Red S was added to each well and stained for 30 minutes at room temperature. The final step was to wash each well with water before observing stained cells under an Olympus BX 41 Brightfield microscope.

#### 4.2.3 Scratch Assay

As previously described, cells were grown to 100% confluency on 6 cm tissue culture plates in standard culture media. A fine tip marker was used to mark the bottom of the plate to identify the regions before and after the scratch was performed. A standard p200 pipette tip was used to gently scrape the cell monolayer leaving a distinct zone for cells to proliferate and migrate towards. Images were then taken directly after the scratch assay and 24 hours later to observe cell migration and proliferation patterns. An ImageJ plugin, designed for scratch assay analysis, was used to quantitate cellular response.

#### 4.2.4 Proliferation Assay

A cell proliferation assay kit was used to assess cell growth over a 72-hour period (Biosciences Cat. #A014). A 1X HBSS buffer (12.5 mL) was created by adding 2.5 mL of 5X HBSS buffer with 10 mL of deionized water. 25  $\mu$ L of Cell-Quant™ dye reagent was added to 12.5 mL of 1X HBSS buffer. Cells were plated at 5000 cells per well in a 96-well plate, combined with nanoparticles, and grown for 24, 48, and 72 hours. The growth medium was removed from the cells by gentle aspiration, and 100  $\mu$ L of 1X dye-binding solution was added to the 96 well plates. The microplate was incubated at 37°C for 30 minutes. Excitation and emission were read at 485/530.

#### 4.2.5 Migratory assay

The migratory pattern assay (EMD Millipore Cat. #ECM515) identified the stem cells' ability to migrate towards a chemoattractant through a filter with 8-micron pores. In this case, the chemoattractant was our nanoparticles. Cells were placed at  $5 \times 10^3$  in a

96 well plate chamber plate. The chamber plate was then placed into a feeder tray with serum-free media and the chemoattract. The cells were allowed to grow and migrate through the pores for 24 hours and attach to the underside of the membrane. After 24 hours, the media solution in the top chamber was discarded. The chamber plate was then placed in a warmed cell dissociation solution for 30 minutes at 37°C to detach the cells that migrated through the pores and into the feeder tray. 75 microliters of the cell solution were placed in a new 96 well plate along with 75 microliters of a lysis buffer and green fluorescent dye. Excitation and emission were done at 480/520 on a Cytation 5 plate reader to measure fluorescent intensity.

#### 4.2.6 Picrosirius Red Stain

Cells were grown for 14 and 28 day periods in a 12-well plate and stained for collagen formation using Picrosirius Red (Diagnostic Biosystems Cat. #47248). Media was removed, and the cells were washed with distilled water once. Cells were then fixed in 10% formalin for 20 minutes and washed three times. Five hundred microliters of Picrosirius red were added for one hour. Three additional washes with acetic acid followed. Images were then taken with an Olympus BX41 brightfield microscopy. After images were taken, the staining was quantified using ImageJ software for percent coverage compared to the control group. Standard error was calculated, followed by a one-way ANOVA and Tukey Post-hoc.

#### 4.2.7 Antibacterial Testing

Bacterial cultures were prepared for testing bacterial growth inhibition after exposure to a combination of tripeptides with CuHNTs. This assay will provide data on

how tripeptide/CuHNT combinations might inhibit bacterial growth and their potential for preventing biofilm formation. Muller-Hinton broth test tubes were used to provide testing mediums for the antibacterial capabilities of the nanoparticles at 500 micromolar concentrations.

#### 4.2.7.1 Muller-Hinton Broth

Liquid medium testing was facilitated using Mueller-Hinton broth (Aldrich Cat. #BCBX5997). 5 mL of Muller-Hinton broth was added to each glass test tube and autoclaved. Once the broth cooled overnight, samples were explicitly labeled for each sample (CuHNT, GHK-CuHNT, GHKP-CuHNT, and GHK-CuHNT). *E. coli* and *S. aureus* were used and presenting gram-negative and gram-positive bacteria. Glass culture tubes were inoculated with 50  $\mu$ L of *E. coli* or *S. aureus* after each nanoparticle was added to the broth of each tube. Controls of uninoculated Muller-Hinton broth and inoculated broth were used, along with a positive control using gentamicin. The cultures and controls were incubated at 37°C for 48 hours before adding 5mL glass test tubes. Optical density was calculated over time and up to 72 hours. Each test was done in triplicate, and the results were averaged.

### 4.3 Results

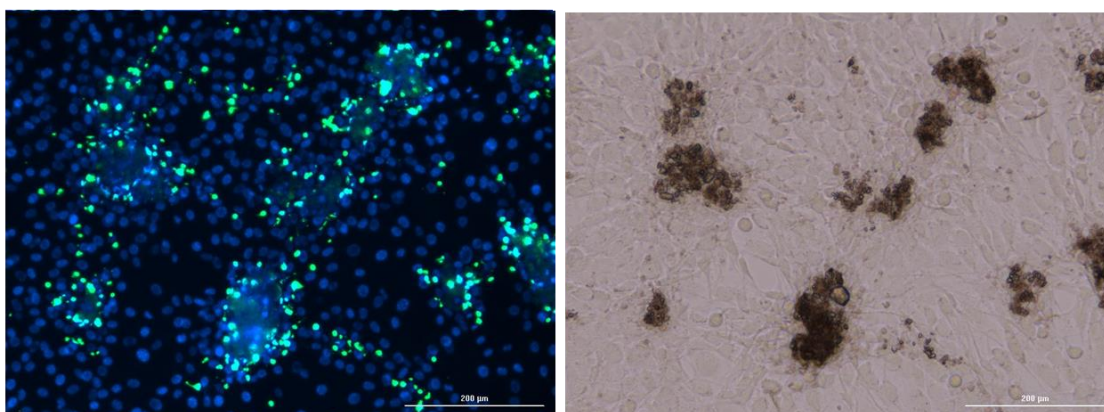
#### 4.3.1 Live/Dead SrHNTs

The fluorescent imaging of hASCs indicated large zones of cellular growth and attachment around SrHNTs. A unique pattern over the 28 days formed trabecular-like structures indicative of bone formation at contact sights of SrHNTs. The hASCs compressed the SrHNTs into these patterns because the SrHNTs were initially dispersed

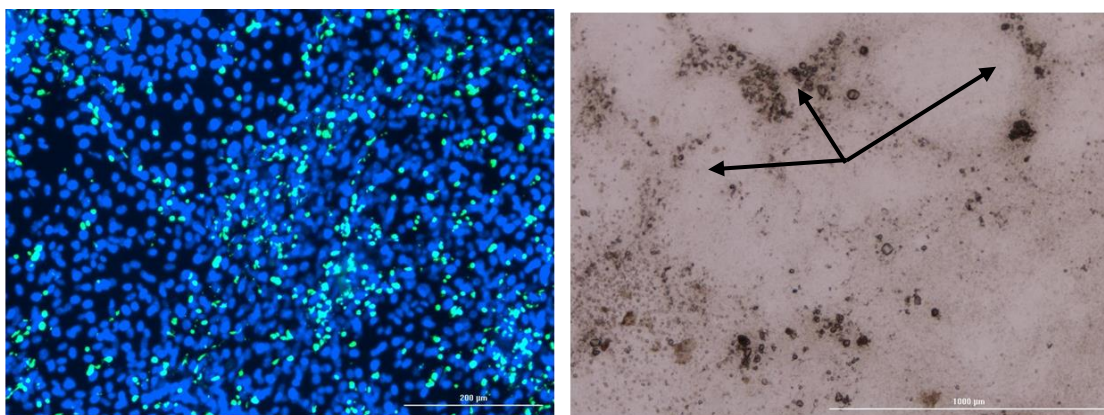
in culture, and over time, they molded the patterns seen in **Figures 4-2** to **Figure 4-4**.

**Figure 4-1** demonstrates only 7 days in culture and a more dispersed pattern in culture.

The structures in **Figure 4-4** can be seen from the naked eye due to the significant growth of cells into cell clusters, and growth would likely continue if the experiment was conducted past 28 days.

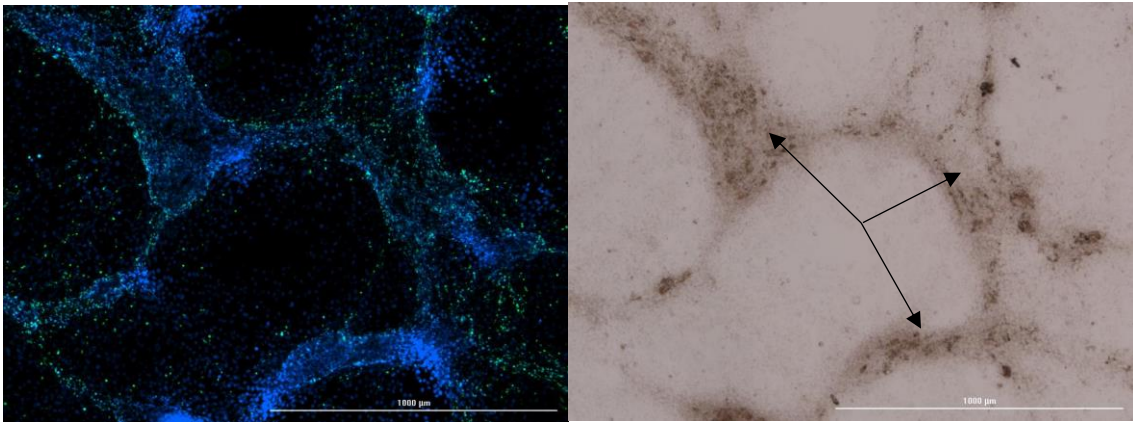


**Figure 4-1.** Left - 7 days after SrHNTs were added to hASCs at a 50 micromolar concentration. Live cells stained in blue. Dead cells are in green. Note. That there was some absorption of the dyes by the HNTs. 10x magnification. Right – cell clustering was observed and apparent internalization of the SrHNTs (dark colored areas)(color brightfield).

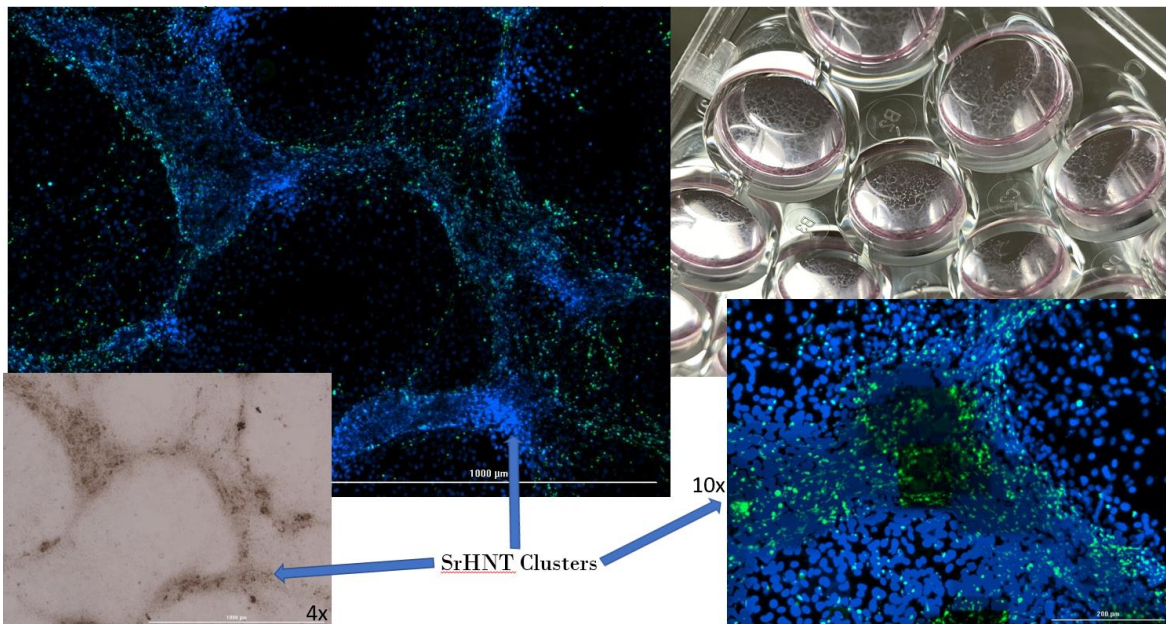


**Figure 4-2.** Left - Live dead stain 14 days after SrHNTs to hASCs were added at 50 micromolar concentration. 10x magnification for immunofluorescence and 4x bright field microscopy images display. SrHNTs were starting to be compacted denoted by the arrows. Live cells are stained in blue. Dead cells were stained green. Similar absorption

of the dyes by HNTs was observed. Right – Cluster of cells and HNTs organized into a ‘trabecular like pattern (color brightfield).



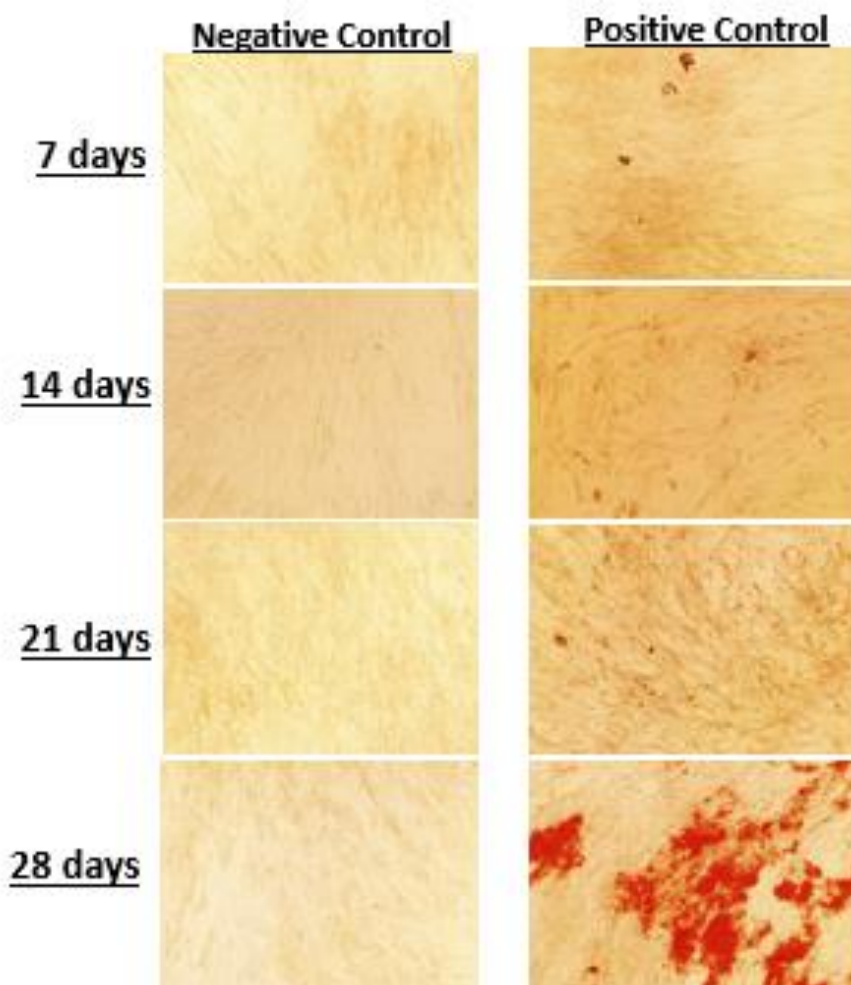
**Figure 4-3.** left - Live dead stain 28 days after SrHNTs to hASCs were added at 50 micromolar concentration. 4x magnification for immunofluorescence and bright field microscopy. Live cells stained in blue. Dead cells in green. Some absorption of dyes by halloysite was observed. Clusters of SrHNTs can be seen and are denoted by arrows. Right – Trabecular like structures are more apparent (color brightfield).



**Figure 4-4.** Cell migration was observed over time with SrHNTs with hASCs after 28 days. The cell pattern manifested as trabecular-like structures (bottom left). Live cells are shown in blue. Dead cells are shown in green. Cell structures can be seen by the naked eye (top right)

#### 4.3.2 Alizarin Red Staining

Alizarin Red assessed the calcium deposits formed for the indication of early bone differentiation processes. The experimental groups were compared to both a negative and positive control group. The negative control group consisted of hASCs grown in cell media with no nanoparticles incorporated. The positive control represented a growth media optimized by Gibco for osteogenic differentiation of mesenchymal stem cells. Calcium deposits were observed in the positive control group, along with SrHNTs at a 50 micromolar concentration after 28 days. Groups using CuHNTs or tripeptides did not exhibit any calcium deposits over the given time frame indicated in **Figure 4-5**.



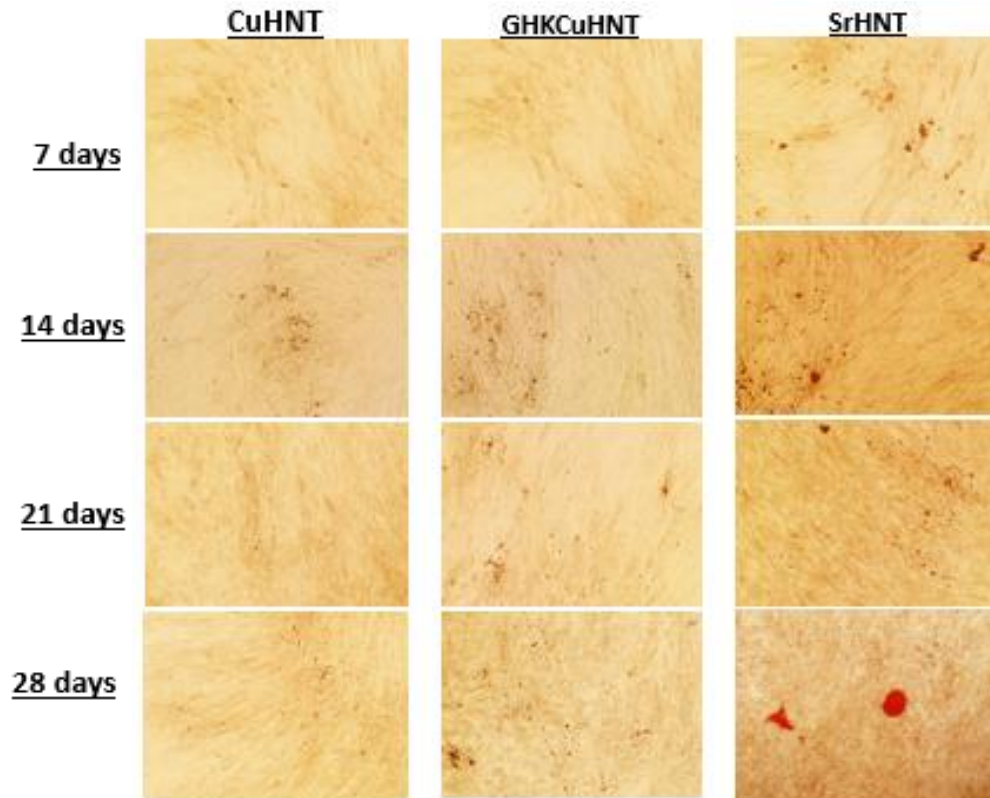


**Figure 4-5.** Alizarin Red staining of each well after days 7, 14, 21, and 28 days exposed to GHKCuHNT, CuHNT, and SrHNT. A negative and positive control were used for comparison. Calcium deposits were only observed in the positive control and SrHNT groups.

#### 4.3.3 Artificial Wound Closure

Artificial wound closure experiments were grown over a 24-hour time frame, given the nature of the assay. Longer durations are not achievable in this setup due to the doubling time of hASCs and the complete closure of the area for all groups. However, the incorporated tripeptides of GHK, GHKP, and GHKCuHNT recorded an increase in wound closure over 24 hours after quantitative analysis by ImageJ software. A noticeable change is also observed qualitatively in **Figure 4-6**.

$$\text{Wound Closure}\% = \left( \frac{A_{t=0} - A_{t=\Delta t}}{A_{t=0}} \right) \times 100\%$$

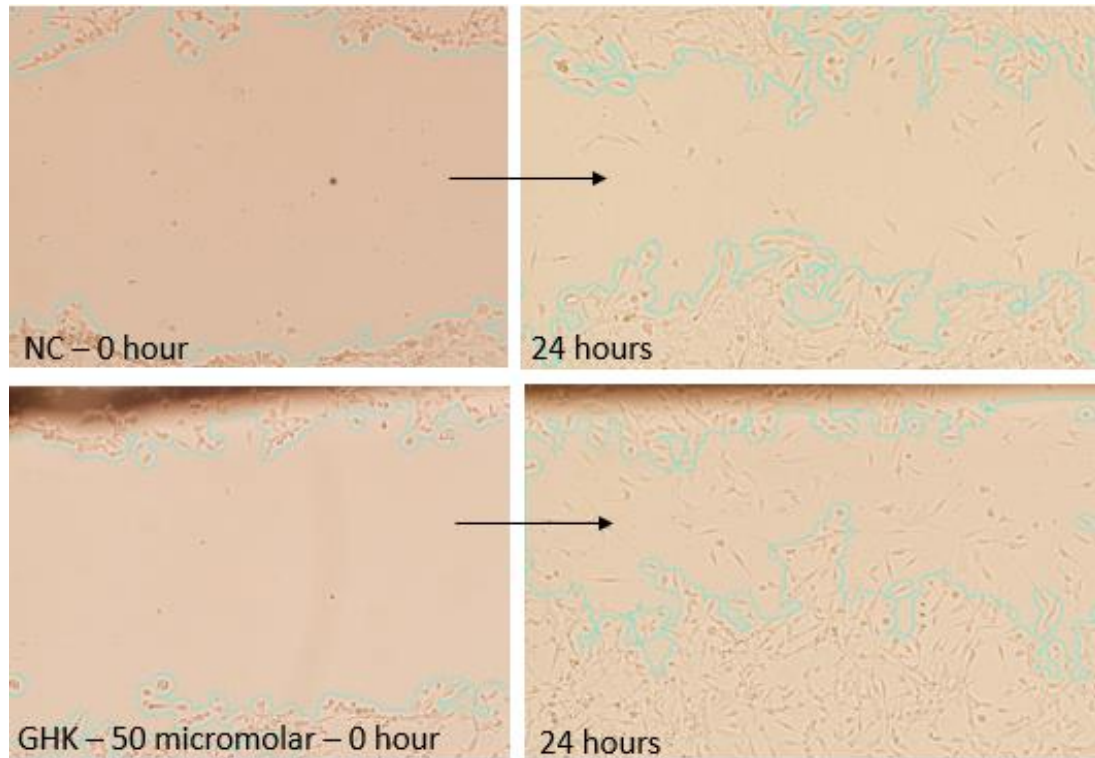


**Figure 4-6.** Scratch assay of controls compared to GHK from time 0 hour to 24 hours. A statistical analysis was carried out with a one-way ANOVA followed by Tukey post-hoc analysis.

**Table 4-1.** Wound closure area percentage after 24 hours. GHK, GHKP, and GHK-CuHNTs showed a significant increase in wound closure percentage using the wound analysis plugin for the ImageJ software.

Treatment →	Negative Control (NC)	GHK	GHK-P	GHK-S	GHK-CuHNT
% wound area→	58.439	43.214	44.11	53.898	33.193
	54.786	42.624	32.651	45.452	28.073
	65.902	41.646	36.686	44.555	30.829
Treatments		Tukey HSD p-value		Tukey HSD inference	
NC vs GHK		0.0056715		** p<0.01	
NC vs GHK-P		0.00101		** p<0.01	
NC vs GHK-S		0.0558139		insignificant	
NC vs GHK-CuHNT		0.0010053		** p<0.01	

#### 4.3.4 Proliferation Assay

The proliferation assay provided additional support for wound closure experiments measured by the fluorescent intensity of DNA binding complexes. **Figure 4-7** reveals a significant rise in fluorescent intensities for the positive control, GHK, and GHKP over 24 hours at 50 micromolar concentration. After 72 hours, only GHKP and the positive control recorded a statistically significant result. Negative controls comprise no nanoparticles while orange bars represent positive controls using a Gibco formulation to promote proliferation of hASCs (**Figure 4-7**). **Figure 4-8** displays a more comprehensive range of 10-40 micromolar concentrations to assess if different concentrations impact the proliferation process. Concentrations below 30 micromolar did not exhibit any significant rise in proliferation over 72 hours.

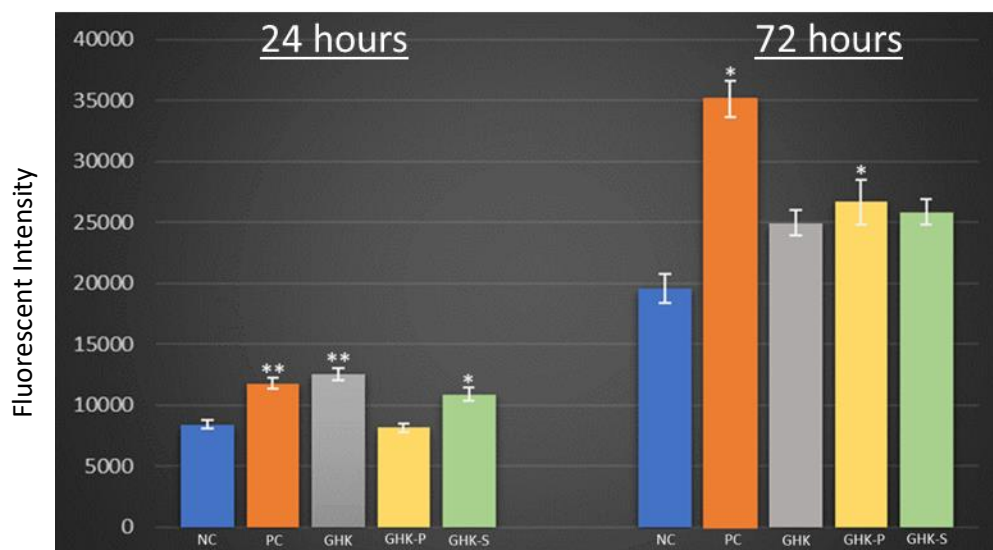


**Figure 4-7.** Tripeptides incorporated at 50 micromolar concentrations. N=3 for all samples;  $P < 0.05^*$ ;  $P < 0.01^{**}$ ; statistical analysis was carried out using a one-way ANOVA followed by Tukey post-hoc. Blue bars indicate negative controls with no nanoparticles. Orange bars represent positive controls using a Gibco formulation to promote proliferation of hASCs.

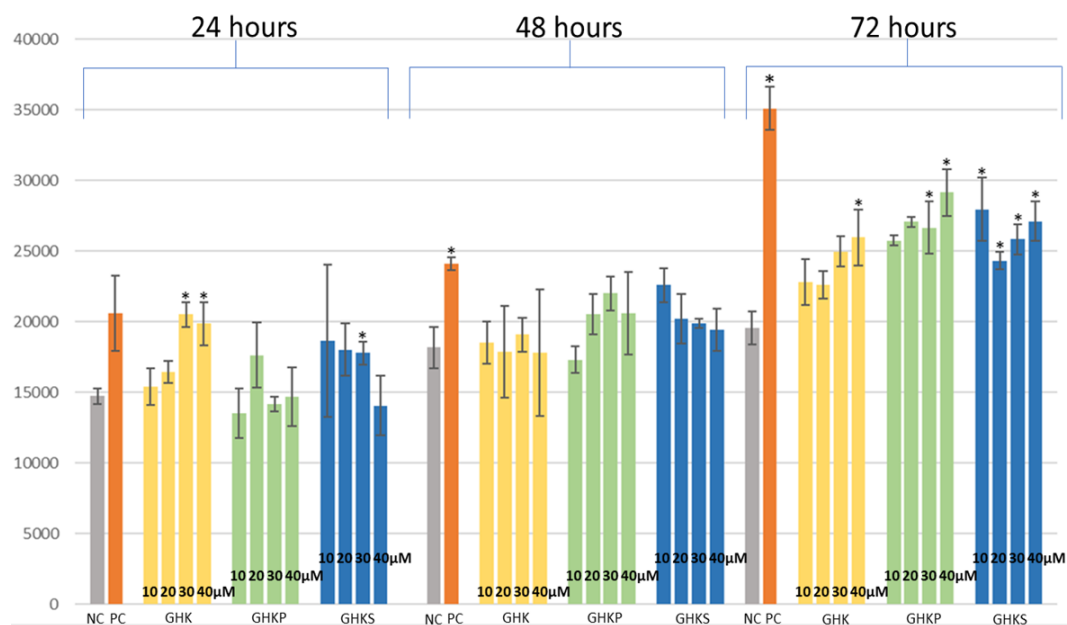


**Figure 4-8.** Proliferating hASCs over 24, 48, and 72 hours. 10, 20, 30, and 40 micromolar concentrations were used for GHK, GHK-P, and GHK-S. Grey bars indicate negative controls with no nanoparticles. Orange bars represent positive controls using a Gibco formulation to promote proliferation of hASCs. N=3 for all samples;  $P < 0.05^*$ ; statistical analysis was carried out with a one-way ANOVA followed by Tukey post-hoc.

#### 4.3.5 Migratory Pattern Assay

The migratory analysis of tripeptides and conjugated nanomaterials are characterized in **Figure 4-9**. GHK was the only chemoattractant showing a rise in cell migration through the chamber pores. A decrease in migration was observed for GHKP, GHKS, GHKPCuHNTs, and GHKSCuHNTs.

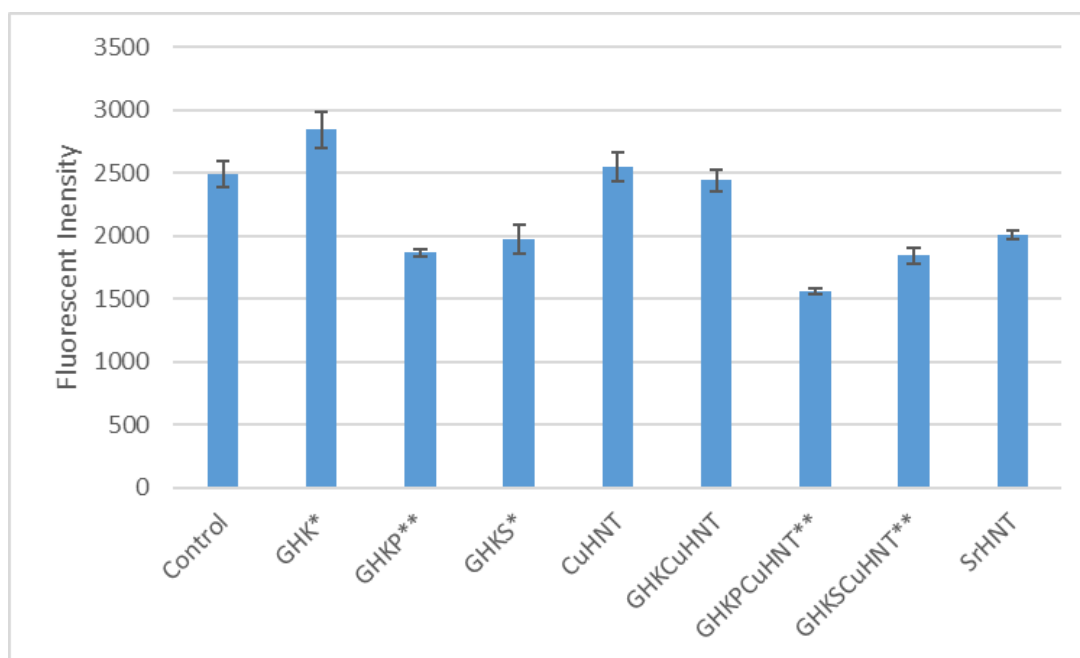


**Figure 4-9.** Migratory assay measured after 24 hours. Nanoparticles were tested as a chemoattractant for cell migration through an 8-micron sized pored chamber. N=3 for all samples; P < 0.05\*; P < 0.01 \*\*; statistical analysis was carried out with a one-way ANOVA followed by Tukey post-hoc. Fluorescent intensity at 580, emission at 620.

#### 4.3.6 Picrosirius Red Staining

The Picrosirius Red stain produced bright red bands for all experimental groups of GHK, GHKP, GHKS, and GHKCuHNTs. Controls produced a low amount of collagen production and staining over the 28-day growth period in the tissue culture plates. The images were additionally quantified with ImageJ software for percent coverage of the

red-stained areas in **Figure 4-11**. The quantified results indicated a significant increase in the percent coverage of all experimental groups.

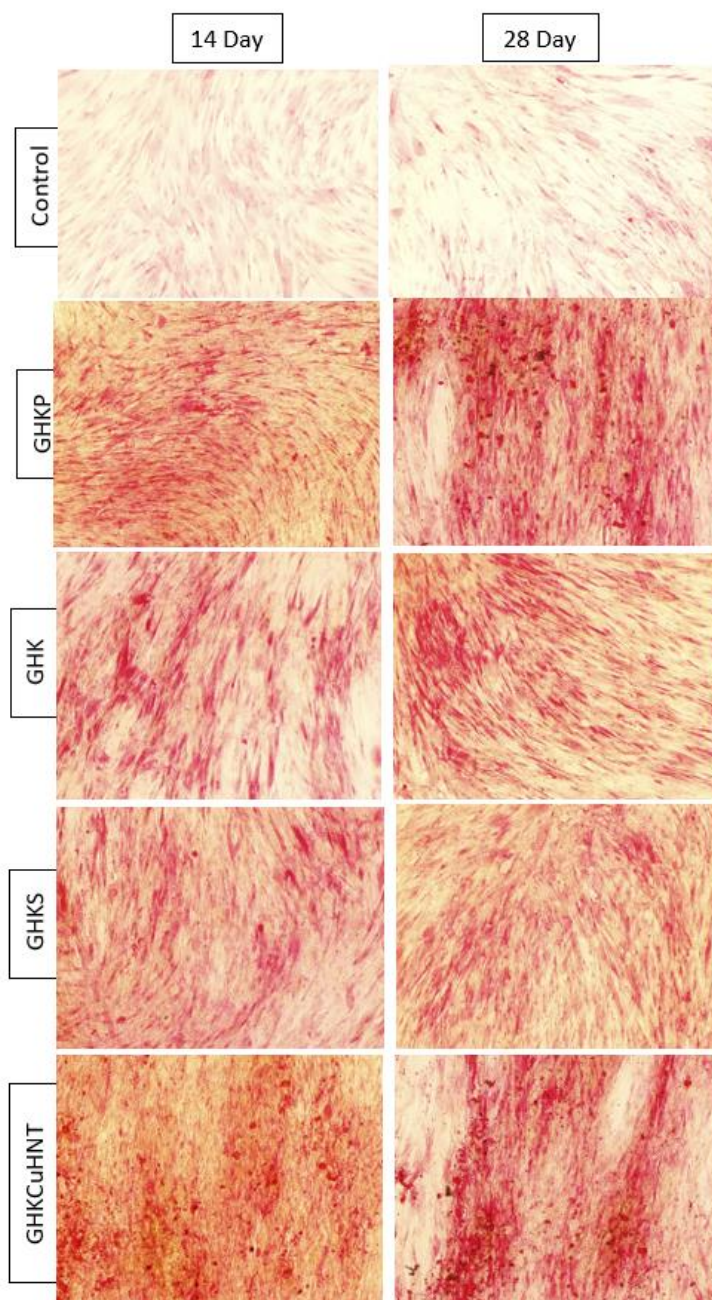


**Figure 4-10.** Picrosirius red stain of hASCs microencapsulated at  $8.0 \times 10^8$  and grown over 28 days. Cell clusters formed and large deposits of collagen were distributed throughout the culture plates. Collagen fibers are stained in red. Control groups represented tissue culture plates that did not have nanoparticles incorporated.

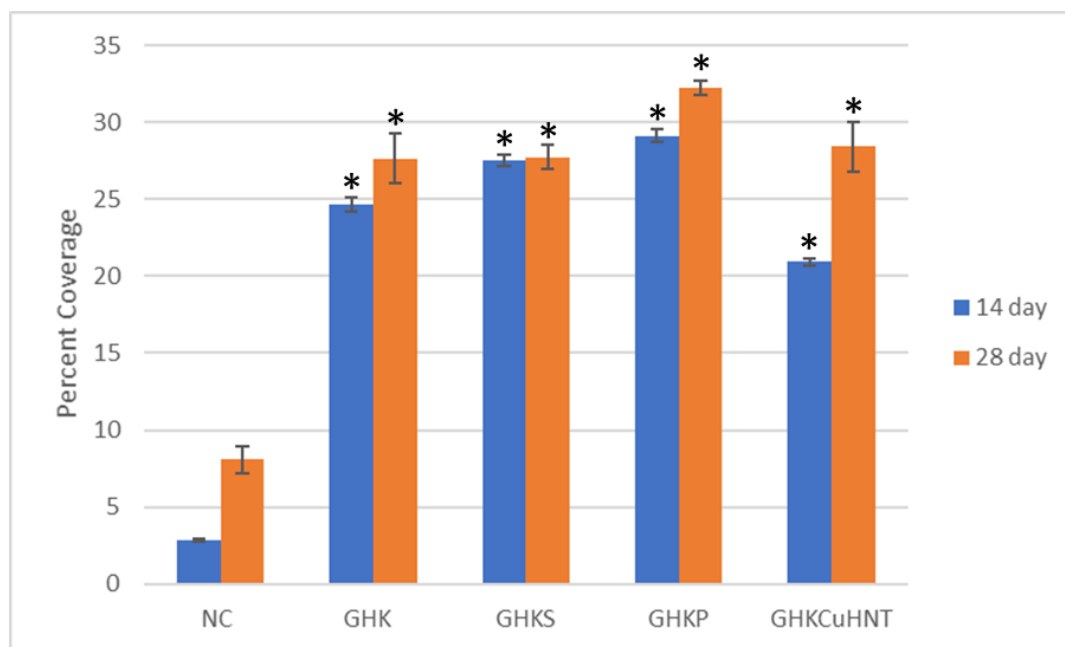


**Figure 4-11.** Percent coverage of Picrosirius Red stain analyzed by ImageJ software. N=3 for all samples;  $P < 0.01$  \*\*; statistical analysis was carried out with a one-way ANOVA followed by Tukey post-hoc. Error bars represent  $\pm$  standard error.

#### 4.3.7 Antibacterial Testing

Antimicrobial properties were assessed using gram-positive and negative bacteria. The bacterial growth was quantified for absorbance at 630 nanometers. After 72 hours, the control group became saturated, so the experiment concluded at this time point. A decrease in growth is shown at 48 and 72 hours for *E. coli* and *S. Aureus* for each nanocomposite indicated in **Figures 4-12** and **4-13**.

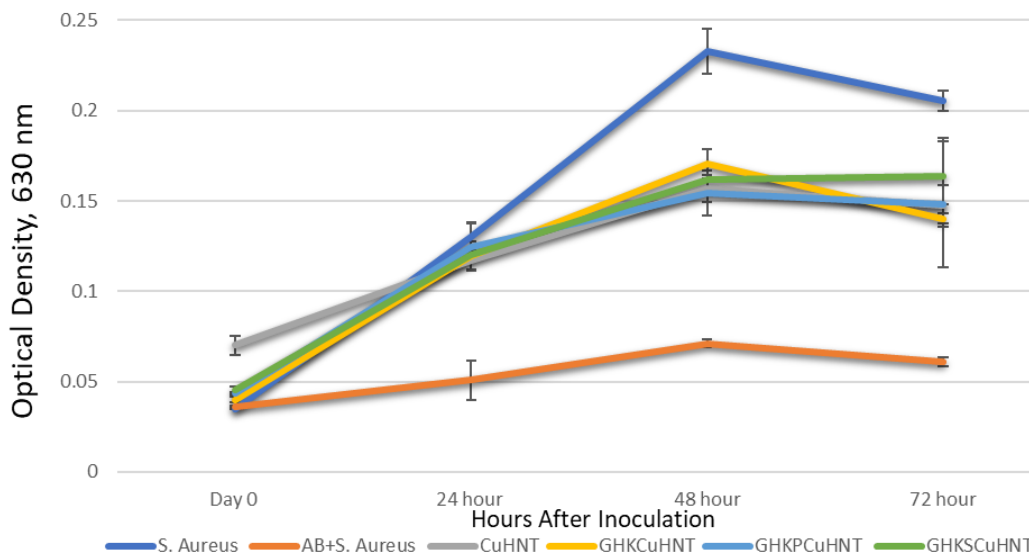


**Figure 4-12** CuHNTs and tripeptides incorporated at 500 micromolar in Mueller-Hinton broth for 72 hours with *S. aureus*. Optical density readings were taken at 0, 24, 48, and 72 hours. Optical density was taken at 630nm wavelength. Error bars represent  $\pm$  standard deviation. (n=3)

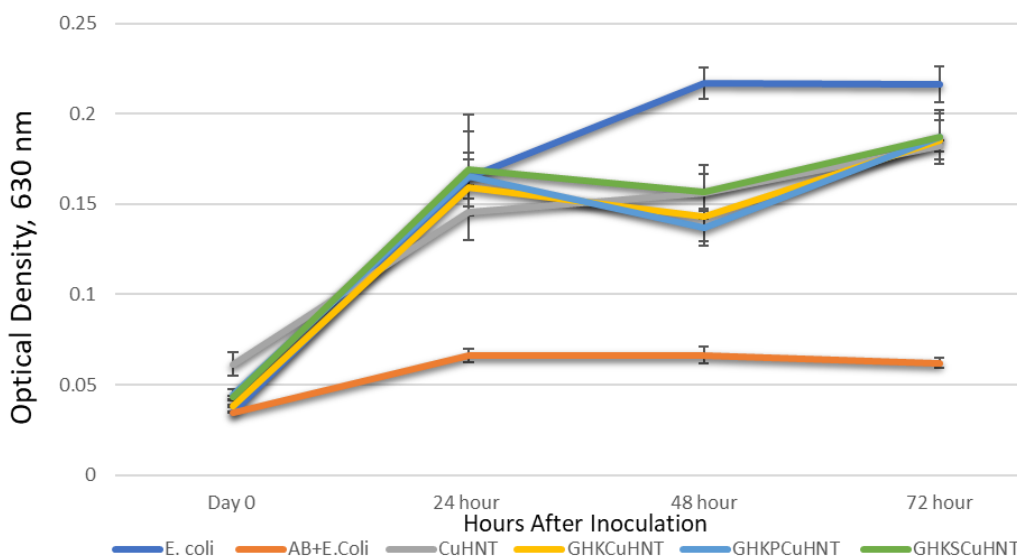


**Figure 4-13.** CuHNTs and tripeptides incorporated at 500 micromolar in Mueller-Hinton broth for 72 hours with *E. coli*. Optical density readings were taken at 0, 24, 48, and 72 hours. Optical density was taken at 630nm wavelength. Error bars represent  $\pm$  standard deviation. (n=3)

## 4.4 Discussion and Conclusion

### 4.4.1 Live/Dead Assay

SrHNTs grown over 28 days displayed a trabecular-like bone formation in culture indicated in **Figures 4-2 to 4-4**. The SrHNTs were dispersed evenly in culture initially, only to be tightly compacted and formed a unique network for the cells to attach and proliferate. The qualitative indication of cell migration patterns packed together supports the hypothesis for the ability of SrHNTs to enhance osteogenic lineages and the previous finding of increased gene expression of *runx2* after 14 days.

### 4.4.2 Alizarin Red Staining

The Alizarin Red stained cells for calcium deposits grown in a 24-well plate over 28 days, including control cells. No calcium deposits were observed in negative control samples containing only hASCs and culture media. Slight staining of calcium was observed in the positive control optimized for bone differentiation in 7-day samples and steadily increased over the growth period. Direct exposure of SrHNTs showed staining of calcium around the SrHNT clusters, suggesting differentiation of hASCs into a preosteoblast lineage in these given areas that directly contact the nanoparticles. Tripeptides and/or CuHNTs did not exhibit any calcium deposits designated by no observable calcium deposits in red. Research suggests that differentiation into the lineage of osteocytes typically shows calcium deposits after 28 days or longer. The formation of bone is typically a more protracted process than other tissue types due to the dense nature of the material. However, our hypothesis supports the use of

exploiting SrHNTs for bone induction capabilities, while indicating CuHNTs are better suited for fibroblast formation after no calcium deposits were observed.

#### 4.4.3 Scratch Assay

After cells were grown to 100% confluency, a p200 tip created an artificial wound across the monolayer surface. The damaged layer across the medial line of the plate represents a similar cellular response at tissue-damaged sites. The disrupted cellular network responded to the external environmental pressures acting on them as they would in the body. Over 24 hours, the artificial open wound system accelerated growth was observed and quantitatively assessed with ImageJ software for wound closure percentage. The wound closure percentage was calculated by taking the total area at time zero, subtracting the change in the area after 24 hours, and then dividing the initial area multiplied by 100 to give the final values displayed in **Table 4-1**. The addition of GHK, GHKP, and GHK-CuHNTs supported the hypothesis by significantly decreasing wound closure over the 24-hour time frame.

#### 4.4.4 Proliferation Assay

Cell proliferation was analyzed over 72 hours using a fluorescent protein that binds directly to the DNA as the cells go through cell division processes. **Figures 4-7** and **4-8** display that tripeptide concentrations influence the accelerated growth in the first 72 hours of exposure. Concentrations between 10-50 micromolar were used with a steady incline in proliferation as concentrations increased over time. 50 micromolar concentrations were an ideal mark to use based on live-dead staining and other assays previously performed. Adjusting tripeptide concentrations in culture is still a necessary

component of future studies to optimize cell growth for open wound systems and stimulate growth factor response systems. However, the assay findings supported the hypothesis that tripeptides stimulate hASCs proliferation for potential wound healing capabilities.

#### 4.4.5 Cell Migration Pattern Assay

The migratory assay identified GHK as a natural chemoattract with hASCs over 24 hours. This was an expected outcome of the procedure due to the synergistic activities known for GHK at tissue damage sites. To our knowledge, this is the first report of GHK acting as chemoattract for hASCs *in vitro*. GHK readily dissolves in solution, allowing the hASCs to respond as if an injury occurs through the transmembrane domain. The lipidized GHK molecules did not produce the same desirable effects, though. However, GHKP and GHKS are only partially soluble in solution due to the fatty acid chain, so GHKP and GHKS molecules tend to sink in solution over time and thus cannot interact with the cell monolayer of the transmembrane domain. This observation is an inherent flaw of the migratory assay if the molecules in use are not completely dissolvable in a particular solution used. In this case, serum-free media was used, so we know that the hASCs are not responding to anything else in the media. We exhibited the same problems with SrHNTs and CuHNTs particles. They are not soluble in water either and will rest at the bottom of the underlying chamber, and no cellular interactions can occur.

#### 4.4.6 Picrosirius Red

Collagen formation is crucial for any wound closure to properly heal over time during maturation and remodeling phases. Collagen is the most abundant protein in the

body and exists in virtually all extracellular matrixes. Picrosirius red is a robust, anionic dye that can associate along cationic collagen fibers to enhance their natural detection under light<sup>84</sup>. The insertion of GHK, GHKP, GHKS, and GHKCuHNTs produced vibrant red bands in culture over a 28-day growth period. The controls produced light staining, indicating a low rate of collagen or fibroblast formation. The images were additionally evaluated for percent coverage using ImageJ software for quantitative analysis. Incorporation of each nanomaterial indicated a significant coverage area of collagen production, as indicated in **Figure 4-11** compared to control groups. This result supports our hypothesis because the introduction of tripeptides and GHKCuHNTs produced large amounts of collagen over time, promoting the differentiation of hASCs into fibroblasts based on qualitative and quantitative data analysis.

#### 4.4.7 Antibacterial Testing

The assessment of antimicrobial capabilities for the nanocomposites was evaluated by both *E. coli* and *S. aureus*, gram-negative and gram-positive, respectively. The bacterial growth in the control group leveled off after 72 hours, indicating the broth had become completely saturated. The assay indicated a decrease in bacterial growth over the 72-hour time frame using a 500 micromolar concentration for each nanomaterial indicated in **Figures 4-12** and **4-13**. However, the level of growth compared to the positive control group, using a gentamycin tablet, exhibited far better antibacterial resistance. However, the broth was much clearer near the bottom of the test tube where the nanocomposites resided. The nanocomposites remained insoluble in broth, and the bacteria may have grown above this area to maintain some bacterial

growth. Different concentrations of nanocomposites could be explored to gain a more desirable impact with the nanocomposites, however. There were no significant differences between CuHNTs, GHKCuHNTs, GHKPCuHNTs, and GHKSCuHNTs in bacterial resistance for *E. coli* and *S. aureus*. It is important to note that there was no increase in antimicrobial activity after incorporating each nanomaterial, leading to their use in a bandage for wound healing and infection protection.

#### **4.5 Future Studies**

To expand on artificial wound analysis and migratory patterns, an *in vivo* animal model involving male Sprague-Dawley rats would be a better system to evaluate the effectiveness of metalized halloysites and GHK bound halloysites for regenerative tissue applications. Rats provide an ideal mammal model to expand *in vitro* capabilities due to the relative low cost compared to larger mammals (rabbits, monkeys, etc.), adequate dorsal area for wound creation, and similar wound healing mechanisms seen in humans. The use of metalized halloysites has already shown their cytocompatibility and antimicrobial attributes in human cell culture experiments, so testing our hypothesis and technology with male Sprague-Dawley rats to evaluate the efficacy of GHK bound halloysites is the natural next step. GHK is a naturally occurring biological molecule known to aid in angiogenesis, prevent pain/inflammation, and possess anti-cancer properties. GHK is an ideal molecule to combine with our metalized and drug-doped halloysite to regenerate tissue faster, eliminate infection, and prevent pain/inflammation. Diabetic and ischemic wound patients, amputees, and life-threatening burn/trauma victims can all benefit from our patented and multifunctional

bandage technology. Assessing host immune response during the complexities of wound healing in rats is a necessary step to evaluate the effectiveness of GHK bound halloysites for regenerative medicine.

Halloysites would first be coated with metal ions and mixed in solution to bind GHK, GHK-Palmitic acid, or GHK-Steric acid. Electro-spun or blow-spun PLA bandages coated with our Halloysites nanoparticles would then be assembled. Once the bandage is constructed, 5 groups of rats would be used, with 6 in each group at a statistical power of 90% and 0.8 effect size based on GPower calculations. The four experimental groups would be compared with a control group using traditional gauze and antibiotics. An additional 10% attrition rate is also generally applied in animal studies for a total of 33 rats to be used for the experimental design.

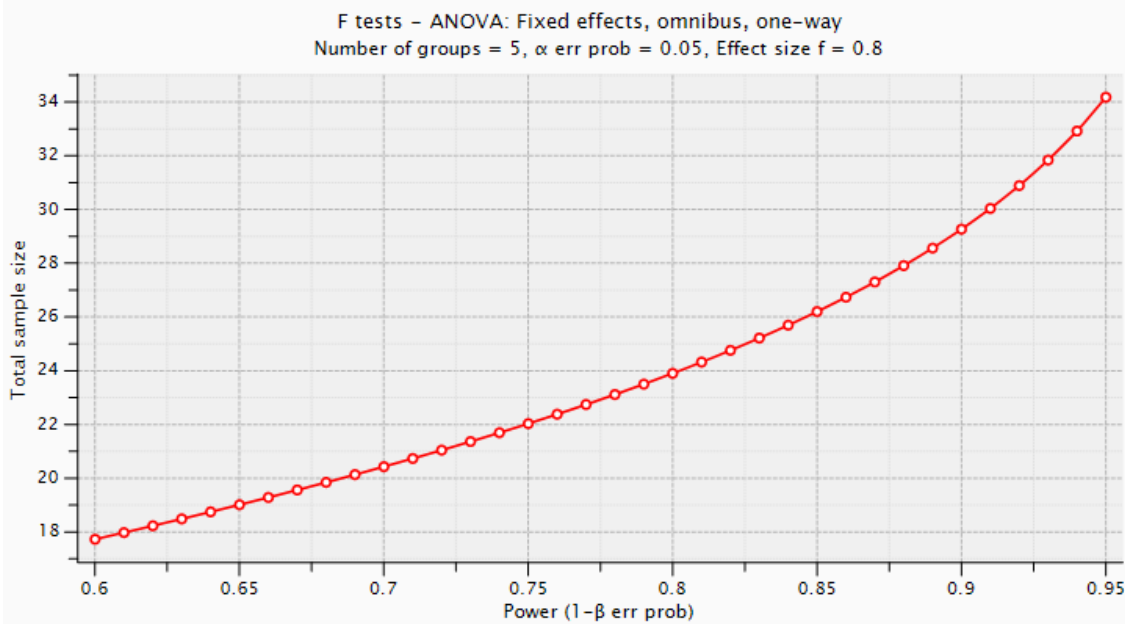


**Figure 4-14.** GPower calculations based off a one-way ANOVA for ethical use of nanoparticles combined into FDA approved materials.

## CHAPTER 5

### INVESTIGATING 3D MATRIX FOR TISSUE FORMATION

#### 5.1 Introduction

Alginate-based biomaterials have widely been applied to repair both soft and hard tissues, including skin and bone, partly because alginate is a naturally occurring, cost-effective alternative derived from brown algae known as *Sargassum angustifolium*<sup>85,86</sup>. Similarly, injectable-based alginate systems, using Akermanite, a bioceramic composed of magnesium instead of aluminum found in halloysites, facilitated wound closure over 21 days in mice<sup>87</sup>. Given these considerations, hydrogels were chemically crosslinked with 4% w/v sodium alginate with calcium chloride and embedded with CuHNTs for *in vitro* models.

Alginate hydrogel microspheres were also used to encapsulate hASCs and exposed to GHK based nanoparticles previously described. Reverse crosslinking occurs when the sodium ions get replaced by calcium ions forming a gel polymer of calcium alginate. GHK, GHK-P, GHK-S, and GHK-CuHNTs were added to the 4% sodium alginate solution before crosslinking. Controls with no tripeptides or metalized HNTs were used for comparative analysis. Cells were encapsulated by mixing a trypsinized cell suspension in DMEM at a density of  $8 \times 10^5$  cells per mL in the alginate solution. Dropwise

microspheres were added to a 75 micromolar concentrated calcium solution for 15 minutes before being added to culture plates and stored at 37°C and 5% CO<sub>2</sub>. Picrosirius Red stain was used to stain extracellular matrix proteins, and the stained hydrogels were imaged under a light microscope, SEM, and immunofluorescent staining.

Alginate microspheres provide an ideal 3D environment to address the physical pressures to which cells respond and increase their ability to stimulate the desired cell response. We hypothesized that introducing GHK nanocomposites into the alginate microspheres would increase cell proliferation and differentiation by providing enhanced cellular support for the activation of wound healing pathways, such as VEGF. This pilot study should enhance our understanding of how GHK nanocomposites and hASCs may be used in either hydrogel applications or 3D bioprinting for tissue regeneration.

## 5.2 Materials and Methods

### 5.2.1 Cell Microencapsulation

Human ASCs were trypsinized, suspended in media, and spun down at 1500 rpms for 8 minutes before encapsulation. Cells were then transferred to medical-grade sodium alginate (Aldrich Cat. #SHBL1627) dissolved in PBS at a concentration of 40 mg/ml at a concentration of  $8 \times 10^5$  cells/ml and cross-linked in a calcium solution containing glucose and HEPES. Calcium cross-linking solution: 75 mM CaCl<sub>2</sub>, (Fisher Cat. #AD5053) 90 mM glucose, sodium pyruvate, and 10 mM HEPES in ultrapure water; pH was 7.3. After combining equal volumes of the cell suspension and 4 % alginate (w/v), the alginate–cell suspension is transferred to a sterile syringe. The syringe is equipped

with an inner diameter of 0.175 mm. Alginate microbeads were allowed to cross-link for 15 minutes. After washing with PBS to remove the excess calcium ions, the microbeads were suspended in cell culture media containing DMEM, 15% FBS, and 1% pen/strep.

#### 5.2.2 4K high resolution digital Imaging

Imaging of the hydrogels took place on a VHX 700 digital microscope (Keyence) at 2500x to visualize pores and cross-linking of the hydrogels. The VHK system combines a 4K CMOS image sensor and illumination technique to rival SEM imaging at micron levels.

#### 5.2.3 Immunofluorescent live/dead staining

The live nucleus was stained blue by using a fluorescent tag that binds to A-T rich regions in the nuclear DNA, known as Hoechst 33342 (2'-[4-ethoxyphenyl]-5-[4-methyl-1-piperazinyl]-2,5'-bi-1H-benzimidazole). Excitation and emission at 360/460 nanometers. Dead cells were probed with EasyProbes propidium iodide for red at excitation and emission 535/620 or EasyProbes Green at 490/520. The reading was performed on a Cytation 5 plate reader.

#### 5.2.4 Picrosirius Red staining

Cells were grown for 7, 14, 21, and 28 day periods to test for collagen formation by picrosirius red staining. Media was removed and the cells were washed with distilled water once. Cells were then fixed in 10% formalin for 20 minutes and washed three times. 500 microliters of Picrosirius Red was added for one hour. Three additional washes with acetic acid followed. Images were taken with colored brightfield microscopy. After images were taken, the staining was quantified using ImageJ software

for percent coverage compared to the control group. Standard error was calculated followed by a one-way ANOVA and Tukey Post-hoc.

## 5.3 Results

### 5.3.1 Hydrogel Characterization

The hydrogels were created using sodium alginate and calcium chloride hydrogels. **Figures 5-1** and **5-2** display the hydrogel crosslinks as well as the micropores created in the hydrogel system for nutrient migration into the porous gels. **Figure 5-3** displays the topography of the gel to further characterize the crosslinking of the gel on the surface and how valleys or peaks interact with the surroundings for nutrient absorption. The pink hue of the gel is a result of media absorbed into the gel. Characterizing the hydrogels provides evidence of the 3D matrix formed to support the growth of encapsulated hASCs.

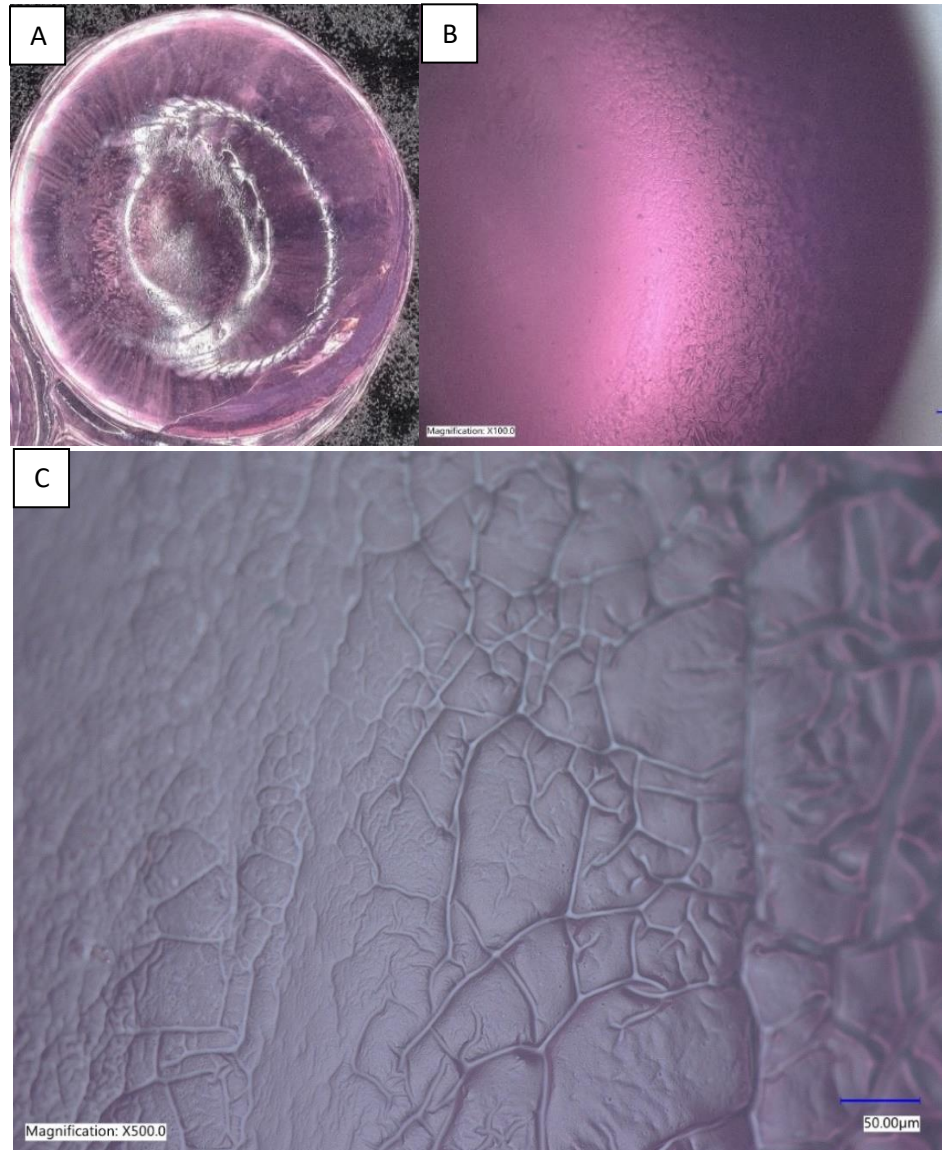


**Figure 5-1.** (A) color brightfield of hydrogels approximately five millimeters in size at 20x after 24 hours. Pink color in part due to absorbed media. (B) 100x magnification of hydrogel (C) 500x magnification displaying crosslinking connections within hydrogel construct.

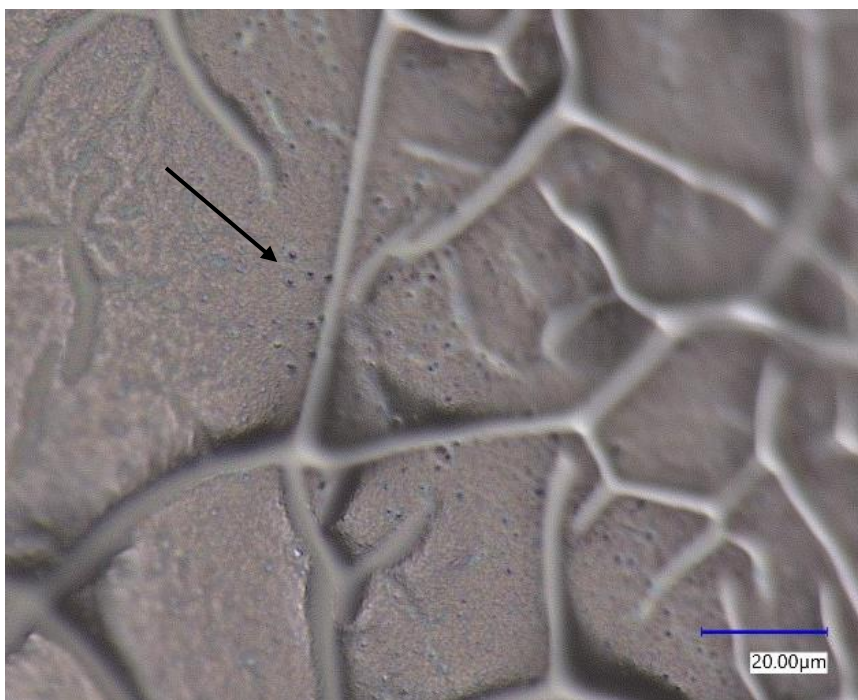


**Figure 5-2.** 2500X magnification displaying pores and crosslinking. The arrow indicates micropores. A 7000 VHX Keyence digital microscope was used to focus on the micropores and crosslinking of alginate and calcium.

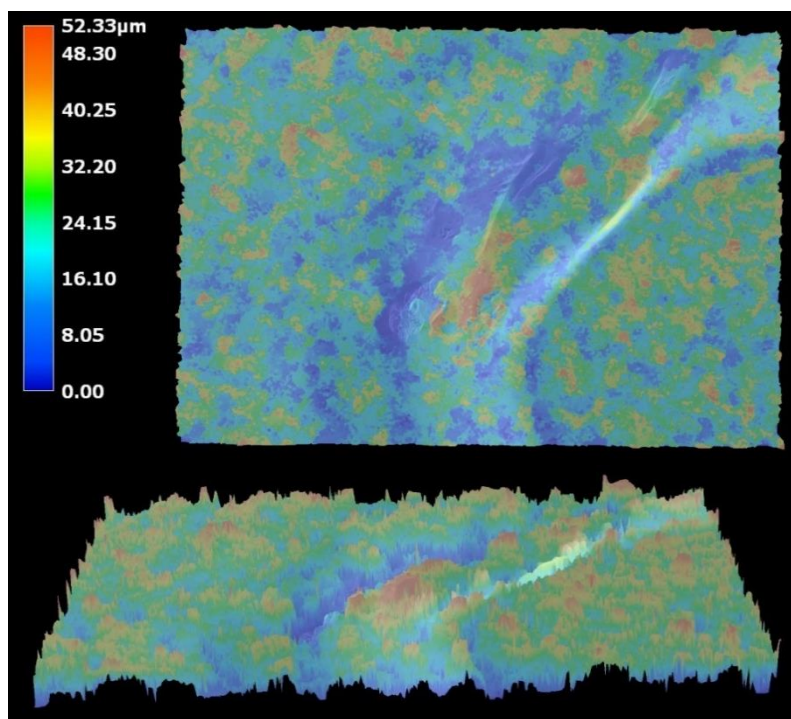


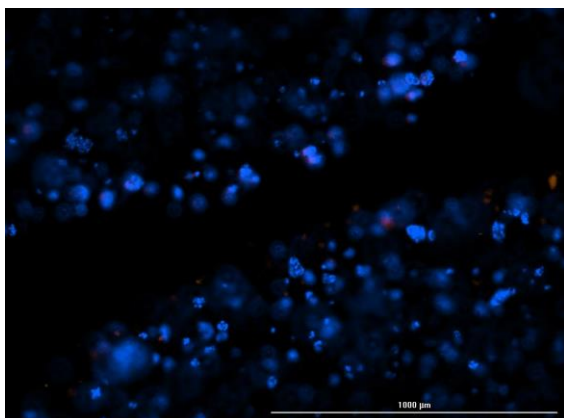
**Figure 5-3.** Topography of hydrogels displaying valleys and peaks. 3D images were z-stacked using a 7000 VHX Keyence digital microscope. The color bar indicates the uneven surface and the presence of crosslinking over the surface.

### 5.3.2 Live/Dead Assay

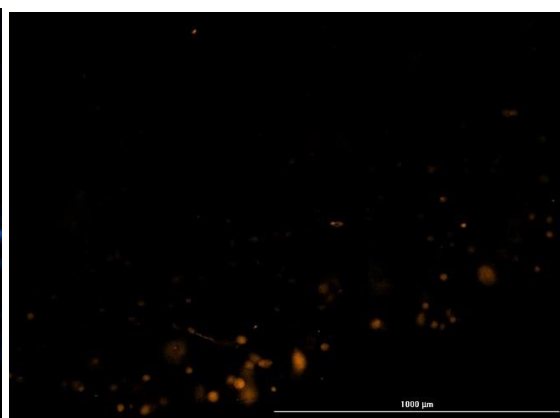
The microencapsulated hydrogel provided a 3D environment for cellular growth and possible differentiation. Clusters can be visualized by a bright blue fluorescent image that stained the nuclei, much like tissue culture plate experiments, from readings performed on a Cytation 5 plate reader at 10x magnification in **Figures 5-4 to 5-7**. The embedded hASCs were difficult to focus on throughout the hydrogel because the cell clusters were randomly distributed in the 3D network at varying depths. However, the pilot study provided additional evidence of the novel nanoparticles GHKCuHNT formed to be used in future studies to understand alginate hydrogels' capabilities for encapsulating hASCs and how they respond to different biomaterials.

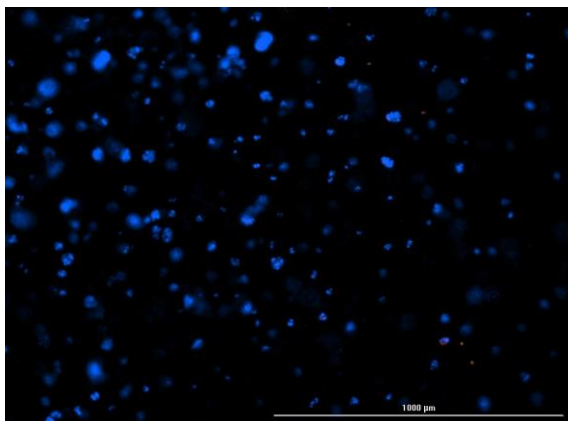
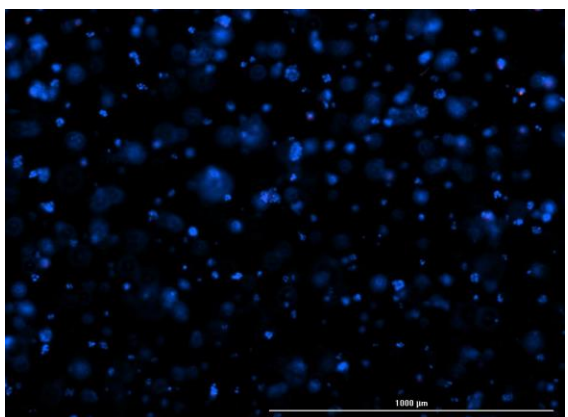
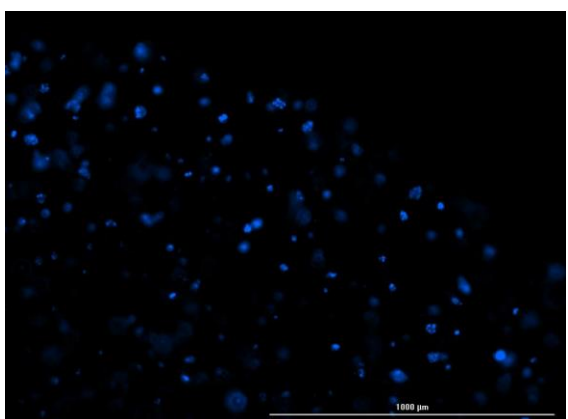
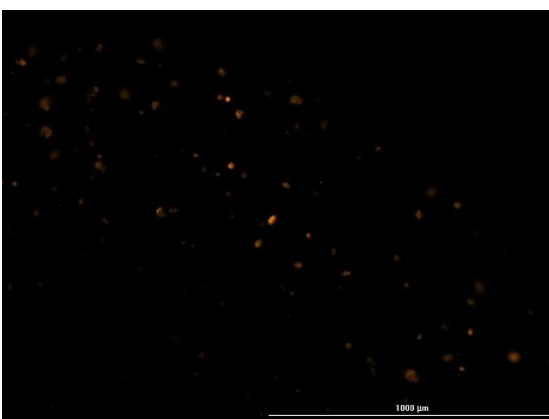
#### **Day 7 – microencapsulation of hASCs in 4% alginate hydrogels**

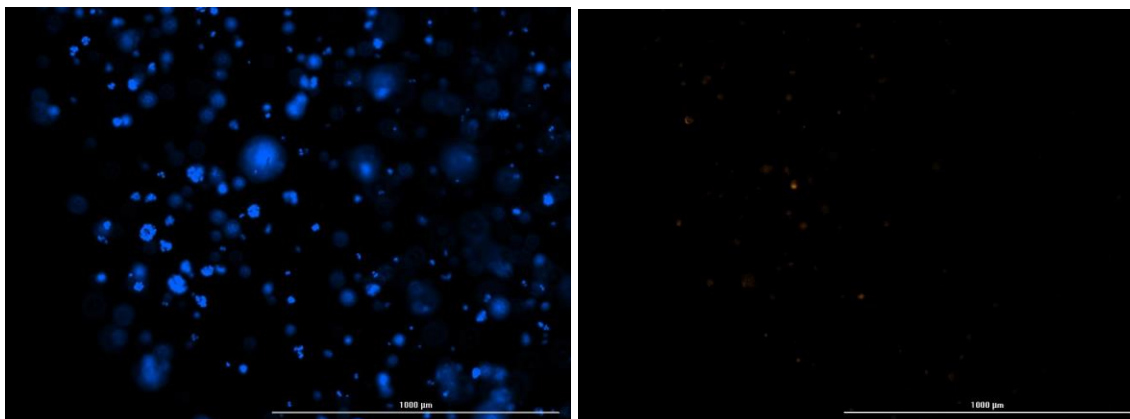
**Negative control live stain**



**Negative control dead stain**

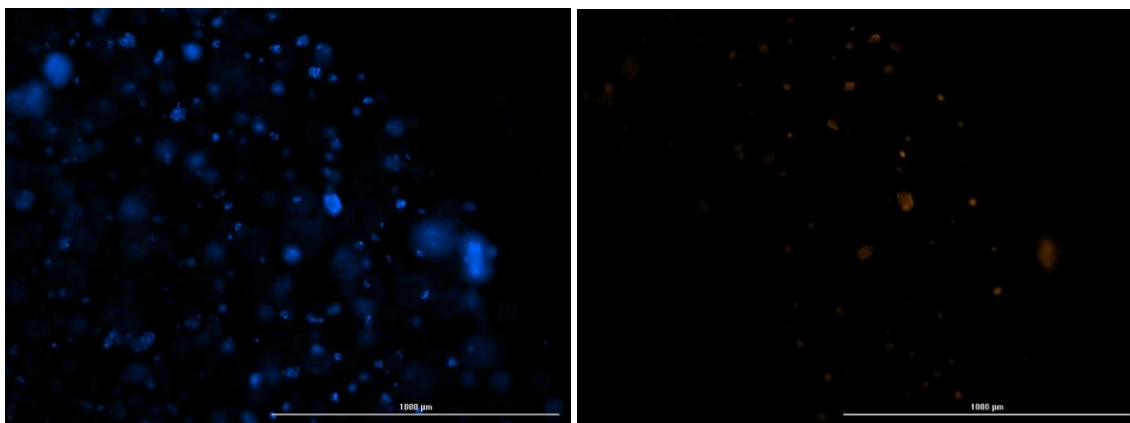


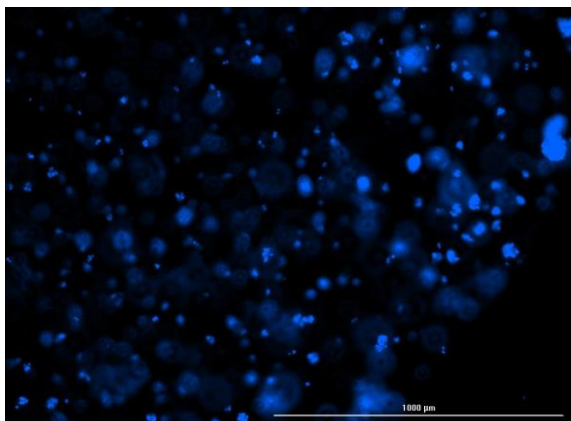
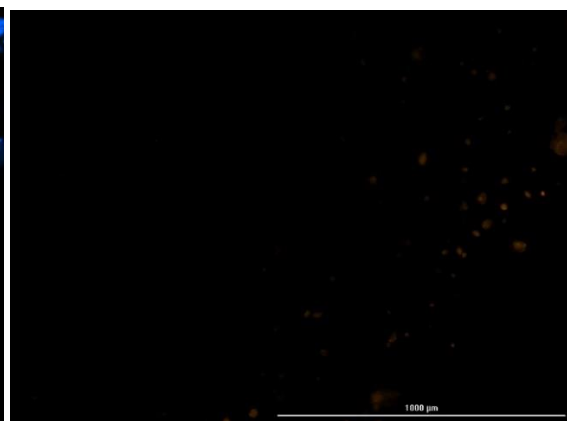
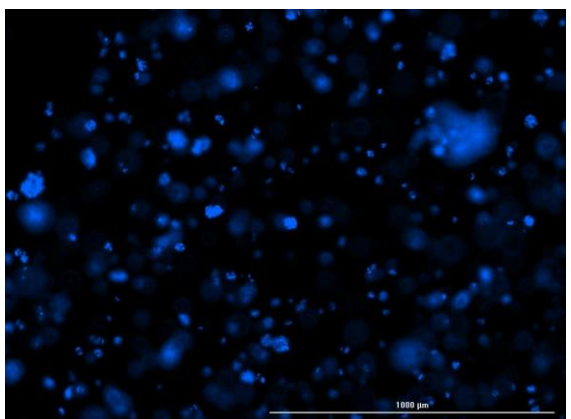
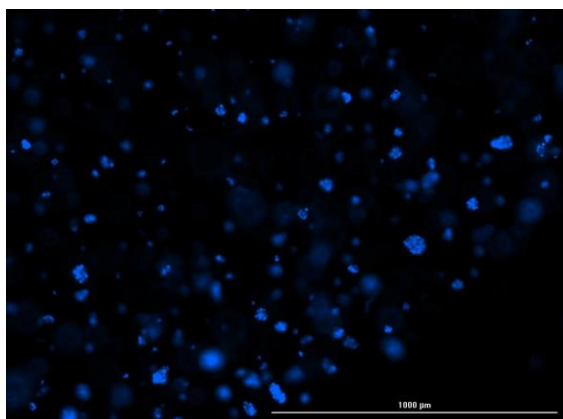
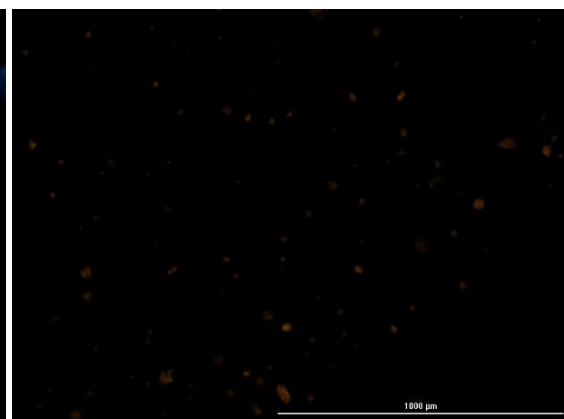
**GHK 50 micromolar live stain****GHK 50 micromolar dead stain****GHK-P 50 micromolar live stain****GHK-P 50 micromolar dead stain****GHK-S 50 micromolar live stain****GHK-S 50 micromolar dead stain**

**GHKCuHNT 50 micromolar live stain****GHKCuHNT 50 micromolar dead stain**

**Figure 5-4.** Live dead Stain of microencapsulated hASCs over the course of 7 days. Live cells are stained blue. Dead cells are stained orange/red. Large cell clusters formed within the hydrogel system with no compromise in cell viability. The reading was performed on a Cytation 5 plate reader.

**Day 14 – microencapsulation of hASCs in 4% alginate hydrogels**

**Negative Control live stain****Negative control dead stain**

**GHK 50 micromolar live stain****GHK 50 micromolar dead stain****GHK-P 50 micromolar live stain****GHK-P 50 micromolar dead stain****GHK-S 50 micromolar live stain****GHK-S 50 micromolar dead stain**

GHKCuHNT 50 micromolar live stain

GHKCuHNT 50 micromolar dead stain

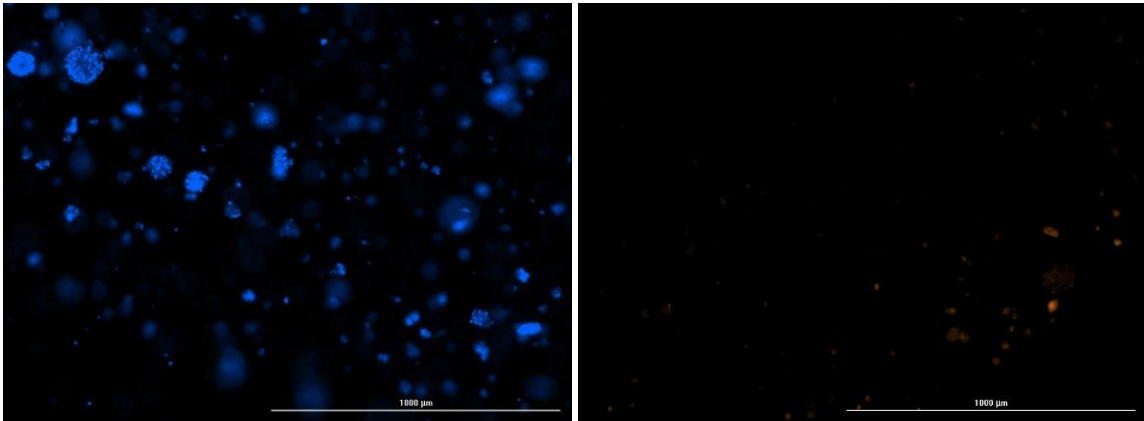
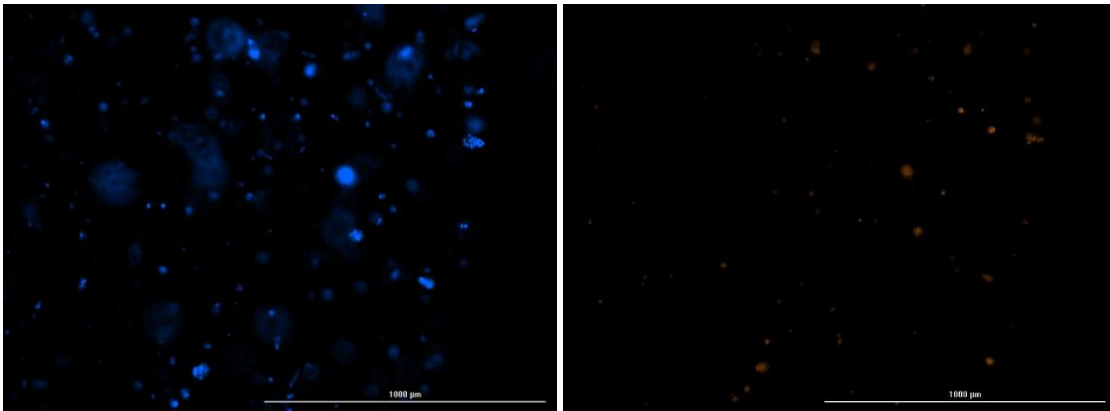


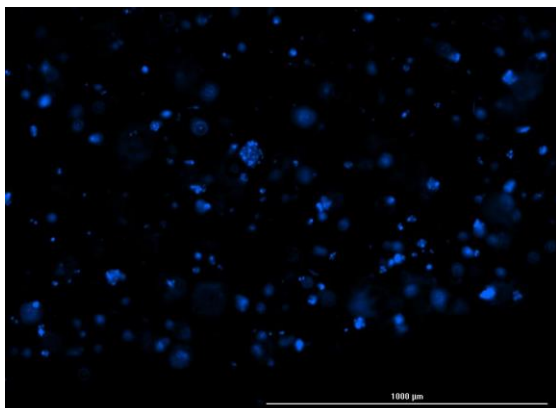
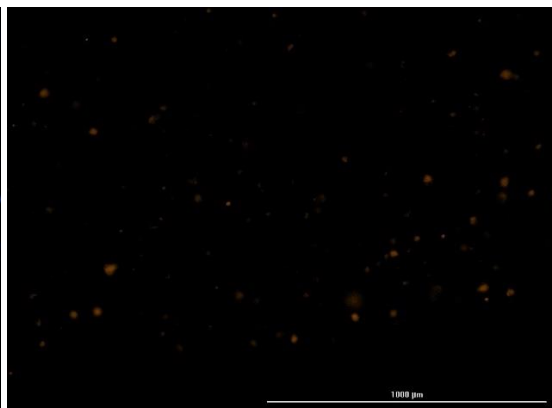
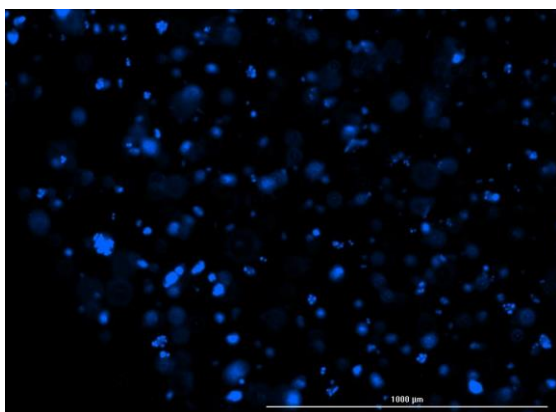
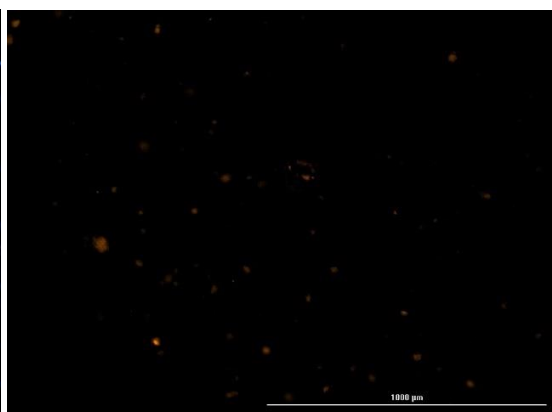
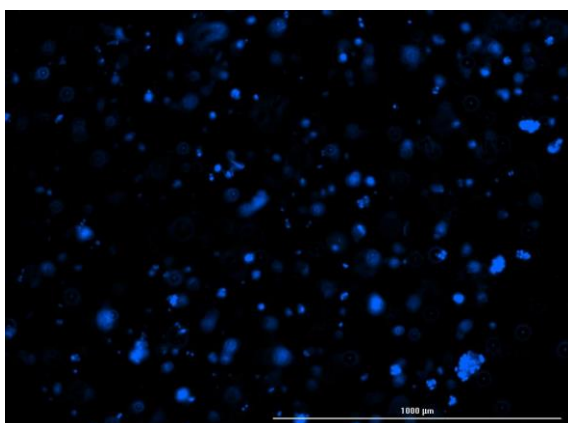
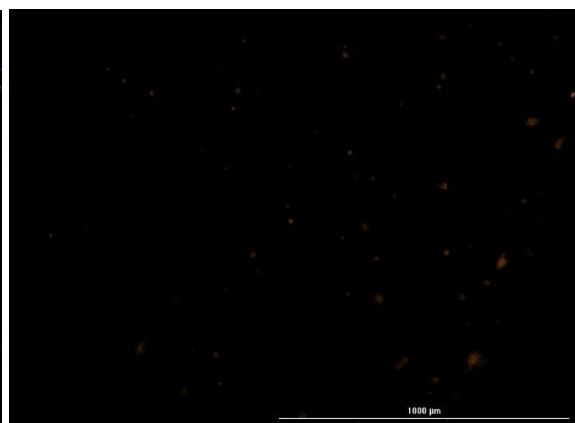
**Figure 5-5.** Live dead Stain of microencapsulated hASCs over the course of 14 days. Live cells are stained blue. Dead cells are stained orange/red. Large cell clusters formed within the hydrogel system with no compromise in cell viability. The reading was performed on a Cytation 5 plate reader.

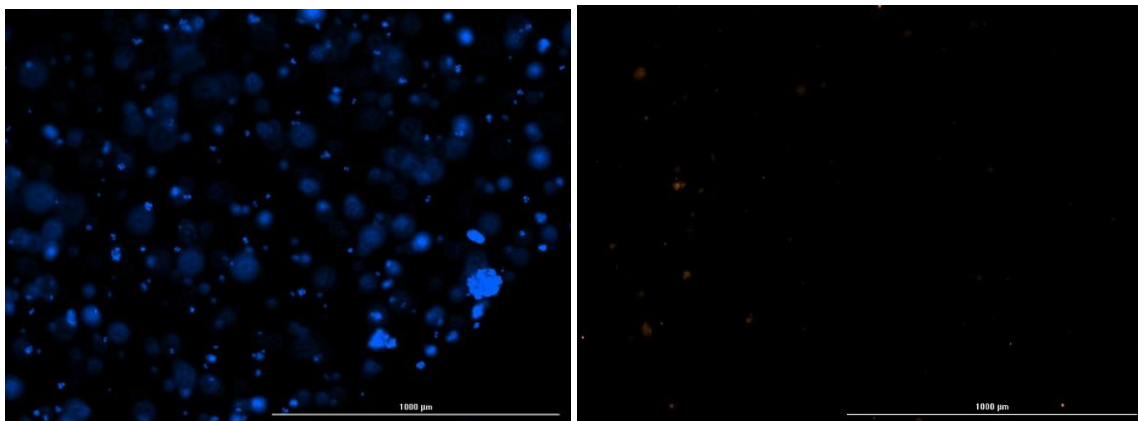
**Day 21 – microencapsulation of hASCs in 4% alginate hydrogels**

Negative Control live stain

Negative Control dead stain

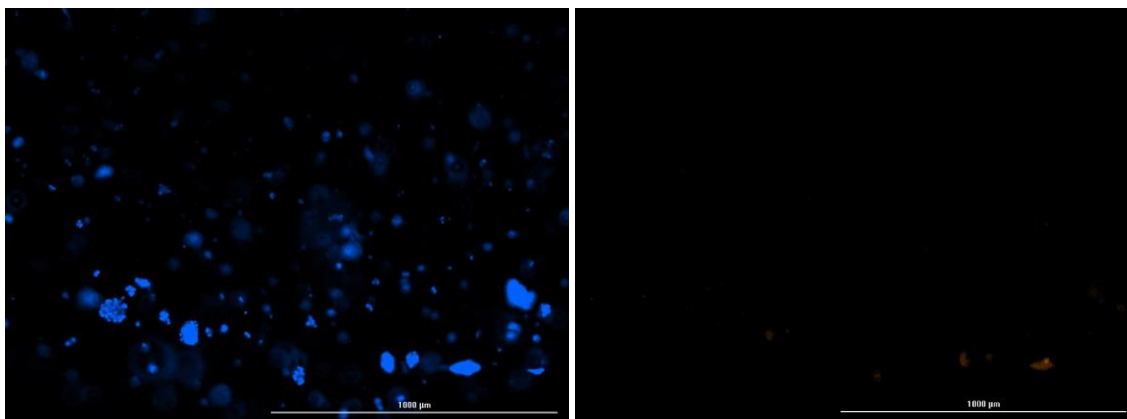


**GHK 50 micromolar live stain****GHK 50 micromolar dead stain****GHKP 50 micromolar live stain****GHKP 50 micromolar dead stain****GHKS 50 micromolar live stain****GHKS 50 micromolar dead stain**

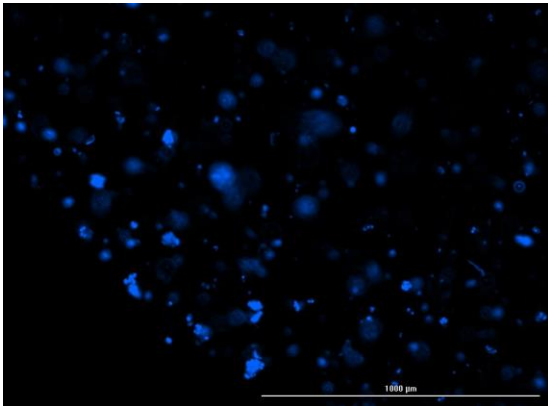
**GHKCuHNT 50 micromolar live stain****GHKCuHNT 50 micromolar dead stain**

**Figure 5-6.** Live dead Stain of microencapsulated hASCs over the course of 21 days. Live cells are stained blue. Dead cells are stained orange/red. Large cell clusters formed within the hydrogel system with no compromise in cell viability. The reading was performed on a Cytation 5 plate reader.

**Day 28 – microencapsulation of hASCs in 4% alginate hydrogels**

**Negative Control live stain****Negative Control dead stain**

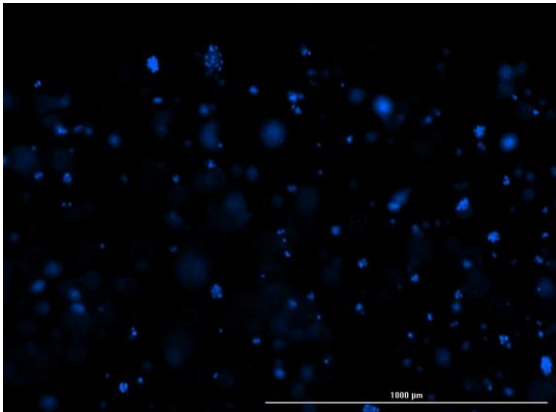
**GHK 50 micromolar live stain**



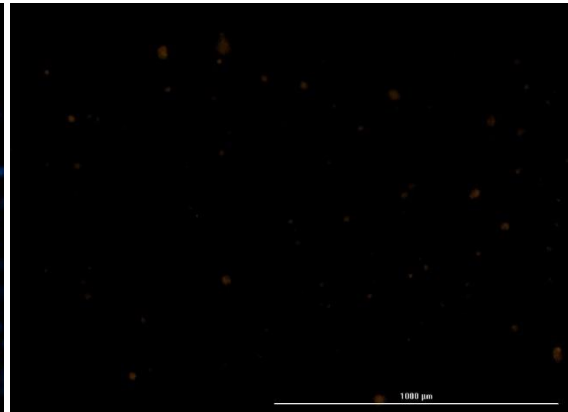
**GHK 50 micromolar dead stain**



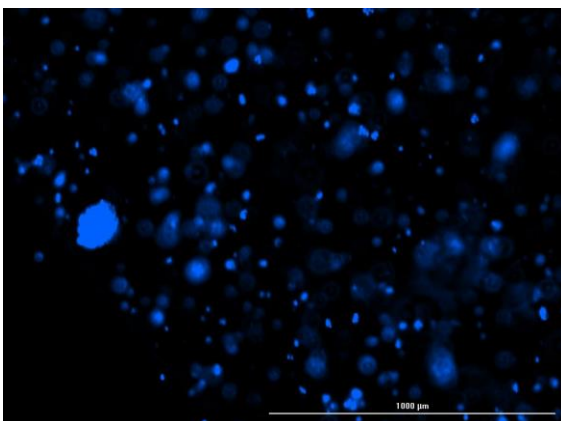
**GHKP 50 micromolar live stain**



**GHKP 50 micromolar dead stain**



**GHKS 50 micromolar live stain**



**GHKS 50 micromolar dead stain**



GHKCuHNT 50 micromolar live stain

GHKCuHNT 50 micromolar dead stain

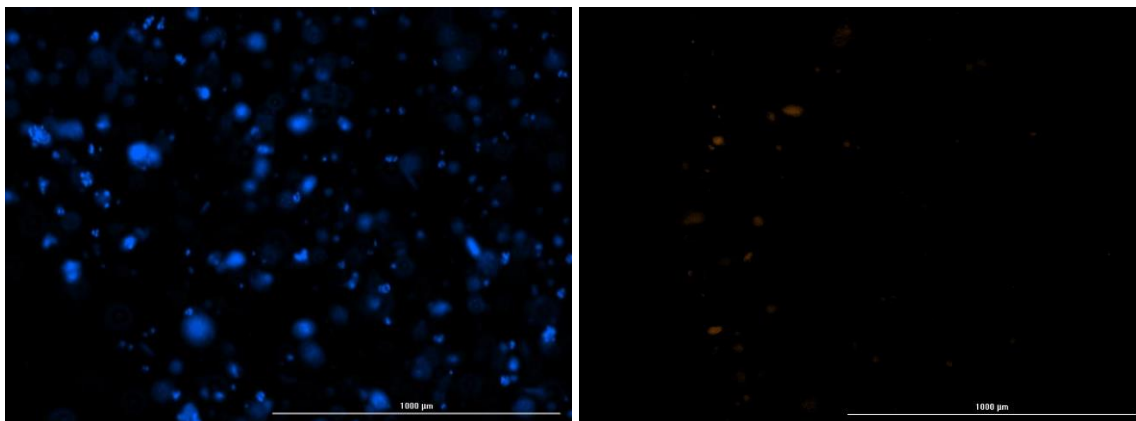


**Figure 5-7.** Live dead Stain of microencapsulated hASCs over the course of 28 days. Live cells are stained blue. Dead cells are stained orange/red. Large cell clusters formed within the hydrogel system with no compromise in cell viability. The reading was performed on a Cytation 5 plate reader

### 5.3.3 Picrosirius Red Staining

Picrosirius Red stain was used to identify possible collagen deposits existing within the alginate hydrogels. The first 7 days of the staining procedure did not show any collagen deposits for the control group. Furthermore, after 14 days, the alginate microenvironment provided cellular support for the formation of collagen deposits in the control groups. However, the incorporation of the tripeptides sped the collagen formation process after 7 days as displayed in deep red staining displayed in **Figure 5-8**. The collagen deposits were later quantified for percent coverage as displayed in **Figure 5-9**, and the results indicated a significant rise in staining and collagen deposits over 28 days compared to control groups. The encapsulated hASCs provided further evidence of fibroblast morphology and how the insertion of nanomaterials can speed up this process.

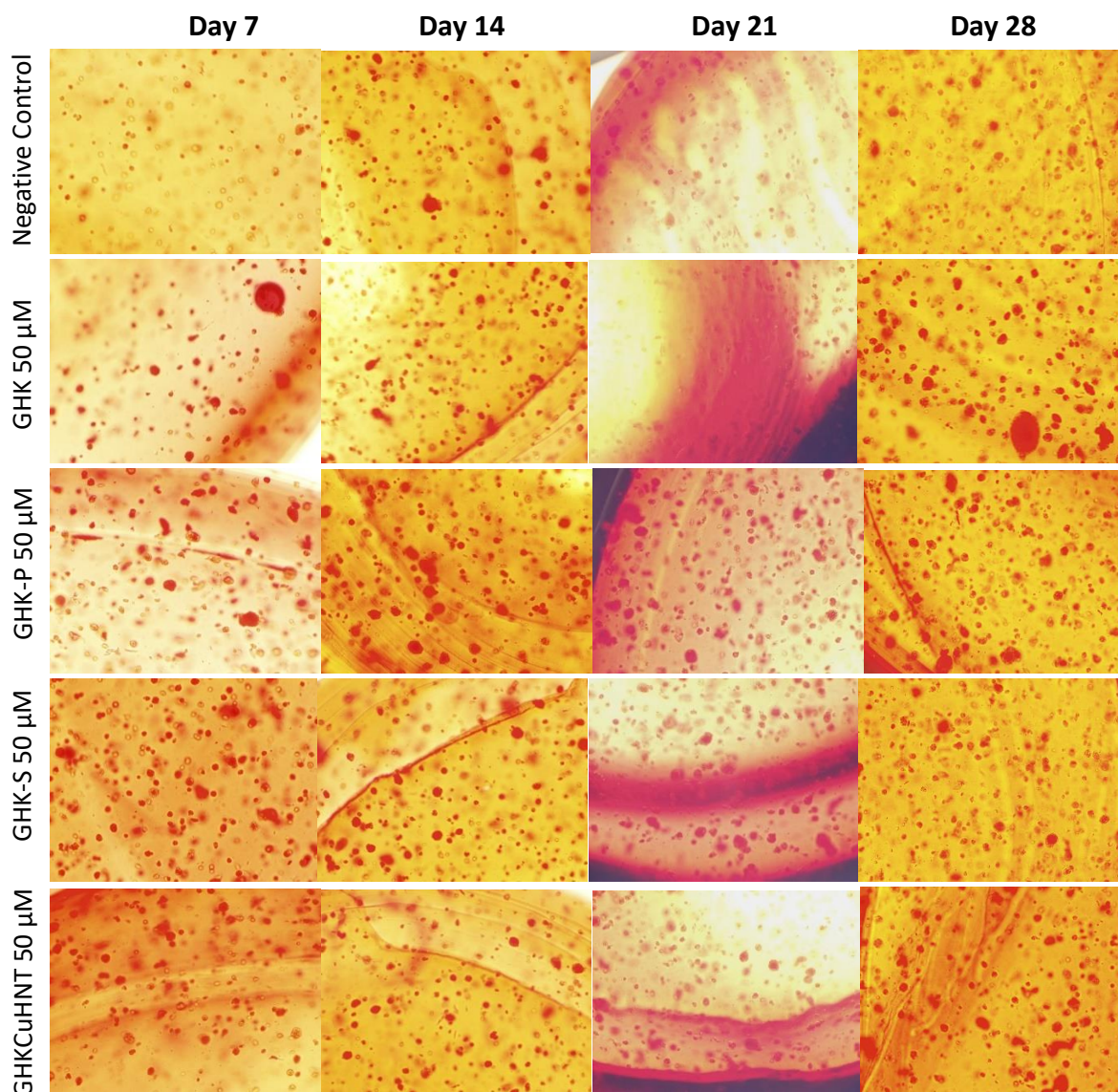


**Figure 5-8.** Picosirius red stain of hASCs microencapsulated at  $8.0 \times 10^8$  and grown over 28 days. Cell clusters are formed and large deposits of collagen are distributed throughout the hydrogels and are stained in red. Photos were taken on an Olympus IX51 at 20x magnification.

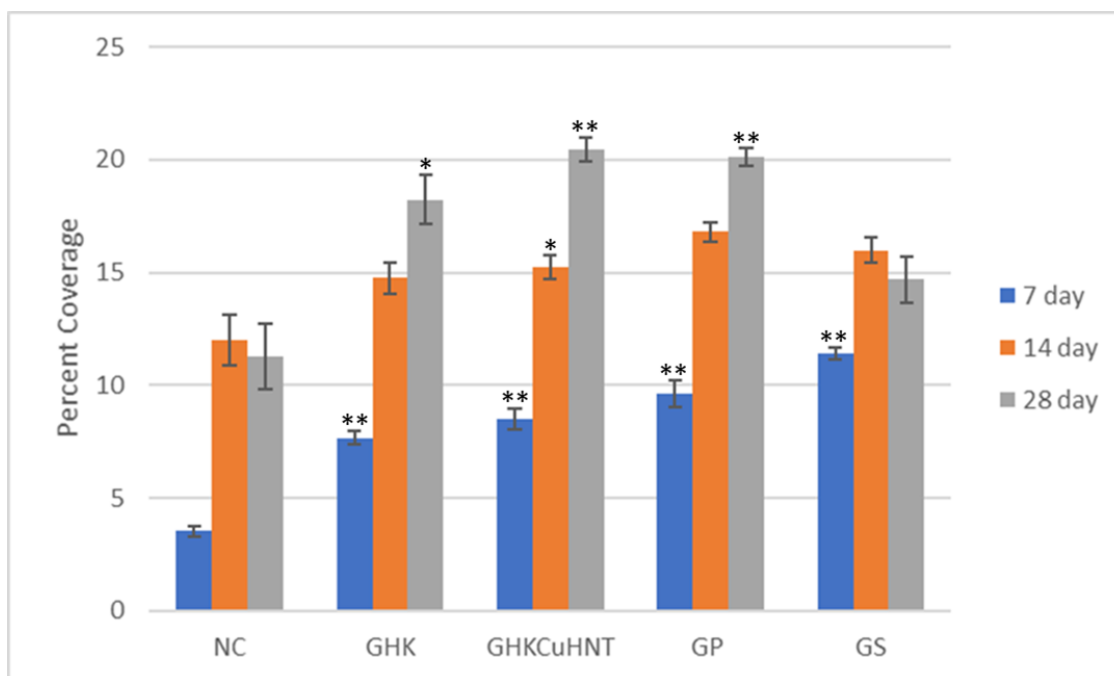


**Figure 5-9.** Percent coverage of Picrosirius Red stain analyzed by ImageJ software. N=3 for all samples; P < 0.05\*; P < 0.01 \*\*; statistical analysis was carried out with a one-way ANOVA followed by Tukey post-hoc. NC denotes the negative control.

## 5.4 Discussion and Conclusion

### 5.4.1 4K high resolution digital Imaging

The topography was analyzed with a 7000 VHX Keyence digital microscope displaying valleys and peaks over the surface of the hydrogels and indicated micropores and channels created throughout the hydrogel matrix (**Figure 5-1 to 5-3**). The integrity of the gels was well maintained over the 28 days, with no noticeable breakdown of the gel in cell culture media during this time frame. Gels were created approximately 5 mm in diameter shown in **Figure 5-1(A)**. The crosslinking of alginate and calcium was also distinctly displayed in **Figure 5-2** to further confirm hydrogel formation.

#### 5.4.2 Live/Dead

The hydrogels used in this pilot study were created using natural polymer alginate over 28 days that demonstrated significant cell microencapsulation potential with hASCs and novel incorporated nanoparticles. Live/dead analysis indicated large cell clusters forming within the gel constructs painted by the bright blue fluorescent staining and minimal cell death shown in red/orange. The clusters can partly maintain their integrity from micropores created through the crosslinking channels of calcium chloride and sodium alginate seen in **Figures 5.1 and 5.2**. The hASCs were able to expand within the hydrogels and limited to clusters given the nature of microencapsulation environments, but this did not inhibit cell viability over time.

#### 5.4.3 Picrosirius Red Staining

Staining for type 1 collagen production was accomplished through Picrosirius red and built upon the initial tissue culture plate studies. As in the culture plate studies, the control group exhibited minor staining, and the stain was again quantitatively confirmed through ImageJ analysis by percent coverage of the area. The displayed clusters within the microencapsulated environment showed large amounts of type 1 collagen formation with the incorporated tripeptides and GHKCuHNT nanocomposite. The large collagen formation indicated the differentiation of the hASCs used into a fibroblast morphology from the large red stained clusters accompanied by the live/dead staining. The GHKCuHNTs produced the most significant collagen production based on the calculated percent coverage over 28 days. The alginate hydrogels and incorporated

nanomaterials supported our hypothesis for collagen formation and differentiation of hASCs into a fibroblast morphology.

### **5.5 Future Studies**

Suppose we can discover the role of external cues dictating molecular activities. In that case, hASCs combined into alginate hydrogels remain an ideal candidate for degenerative bone conditions or areas of extreme trauma. For instance, osteoporosis affects postmenopausal women where bones weaken significantly over time. This process gives rise to different breaks, fractures, and complications due to infection experienced at an older age. Encapsulated hASCs can be utilized and implanted in patients to stimulate the formation of new, healthy bone tissue or vascularization. The pilot studies encompassing the GHKCuHNTs are an ideal source to combine with tissue-damaged areas to produce healthy collagen tissues. There are also growth factors secreted by hASCs, like FGF-2 and VEGF, that stimulate angiogenesis and directly relate to tissue formation around the body. Exploring growth factor secretion profiles of exosomes would be ideal in future studies to demonstrate how cells are attempting to communicate with each other in these microencapsulated environments. FGF-2 and VEGF secreted factors direct stem cell movement, acting as signaling molecules for immune cells in wound healing, so considering these factors existing in the extracellular matrix is essential to note in future studies. Understanding how the environment impacts hASCs and their ability to aid tissue repair will alleviate bone-related pathologies or advanced trauma areas and so needs further study.

The use of hASCs, in combination with bioactive nanoparticles, provides an ideal platform for future clinical studies involving wound care treatment of all varieties. Development of nano-based carriers using GHK, combined with metalized halloysites, will aid in cell attachment, growth secretion profiles, and antimicrobial properties. With this knowledge, we can apply GHKCuHNT particles in FDA-approved materials for nano-enhanced bandages, especially those suffering from severe burns. Severe pain, sepsis, scarring, and death are often associated with widespread burns, and the typical treatment regimens for the larger area come from donor meshed split-thickness skin grafts<sup>58</sup>. However, donor grafts or patient-derived grafts are not ideal when potentially better options do not require grafting. Applying large-scaled hydrogels with encapsulated hASCs to cover burn wounds would provide many immediate advantages. The gels would act as a protective layer from the outside environment while lubricating the area. Applying coatings over the hydrogels or embed GHK or mHNTs with hASCs would stimulate proliferation and secretion profiles of vital growth factors for accelerating skin repair. Think of the gel as a temporary skin that can effortlessly be removed, allowing for the underlying tissue growth to be assessed on demand.

Like many other cells, hASCs respond to their physical and chemical environment, so adding bioactive molecules improves the wound healing process. At the same time, metal ions protect against infection by disrupting pathogenic membranes. There are many other small molecules, like GHK, that need exploration to increase how we treat trauma sites, burn victims, and eliminate infections outside of the clinic. Tripeptides are vital components of the extracellular tissue formation process that

enhance recovery sites and act as chemoattractants for immune cells. Therefore, creating advanced tissue mimicking platforms is an ideal approach for wound care. Identifying alternative healing methods is of ongoing interest in regenerative medicine, and discovering a biomaterial's influence has enormous potential to treat many different pathologies in future clinical studies.

## BIBLIOGRAPHY

1. Eastridge B, Mabry R, Seguin P. Death on the battlefield (2001-2011): Implications for the future of combat casualty care. Published online 2012. DOI:10.1097/TA.0b013e3182755dcc
2. Khan F, Yousuf K, Bagwani A. Vascular injuries of the extremities are a major challenge in a third world country. Published online 2015. DOI:10.1186/s13032-015-0027-0
3. Gimble J, Katz A, Bunnell B. Adipose-derived stem cells for regenerative medicine. Published online 2007. DOI:10.1161/01.RES.0000265074.83288.09
4. Ana P, Tavares O. Osteogenesis of adipose-derived stem cells. Published online 2013. DOI: 10.4248/BR201302003
5. Chorianopoulos N, Skandamis P, Nychas G. Adipose-derived stem Cells (ASCs) for tissue engineering. Published online 2012. DOI:10.5772/51895
6. Bunnell B, Flaatt M, Gagliardi C, Patel B, Ripoll C. Adipose-derived stem cells: Isolation, expansion and differentiation. Methods. Published online 2008. DOI:10.1016/j.ymeth.2008.03.006
7. Dominici M, Le Blanc K, Mueller I. Minimal criteria for defining multipotent mesenchymal stromal cells. Published online 2006. DOI:10.1080/14653240600855905
8. Rachel C, Emily H, Matthew W, Loba E. Bone marrow regeneration promoted by biophysically sorted osteoprogenitors from mesenchymal stromal cells. Published online 2015. DOI: 10.5966/sctm.2014-0154
9. Burrow K, Hoyland J, Richardson S. Human adipose-derived stem cells exhibit enhanced proliferative capacity and retain multipotency longer than donor-matched bone marrow mesenchymal stem cells during expansion in vitro. Published online 2017. DOI:10.1155/2017/2541275

10. Iyyanki T, Hubenak J, Liu J, Chang E, Beahm E, Zhang Q. Harvesting technique affects adipose-derived stem cell yield. Published online 2015. DOI:10.1093/asj/sju055
11. Hutchings G, Janowicz K, Moncrieff L. The proliferation and differentiation of adipose-derived stem cells in neovascularization and angiogenesis. Published online 2020. DOI:10.3390/ijms21113790
12. Sandel D, Liu M, Ogbonnaya N, Newman J. Biochimie Notch3 is involved in adipogenesis of human adipose-derived stromal/stem cells. Published online 2018. DOI: 10.1016/j.biochi.2018.04.020
13. Patel N, Whitehead A, Newman J, Caldorera-Moore M. Poly(ethylene glycol) hydrogels with tailorable surface and mechanical properties for tissue engineering applications. Published online 2017. DOI:10.1021/acsbiomaterials.6b00233
14. Metzger C, Anand Narayanan S. The role of osteocytes in inflammatory bone loss. Published online 2019. DOI:10.3389/fendo.2019.00285
15. He F, Chang C, Liu B. Copper (II) ions activate ligand-independent receptor tyrosine kinase (RTK) signaling pathway. Published online 2019. DOI:10.1155/2019/4158415
16. Stratton S, Shelke N, Hoshino K, Rudraiah S, Kumbar S. Bioactive polymeric scaffolds for tissue engineering. Published online 2016. DOI:10.1016/j.bioactmat.2016.11.001
17. Moshaverinia A, Xu X, Chen C. Application of stem cells derived from the periodontal ligament and gingival tissue sources for tendon tissue regeneration. Published online 2014. DOI:10.1016/j.biomaterials.
18. Liu Y, Li Z, Li J, et al. Stiffness-mediated mesenchymal stem cell fate decision in 3D-bioprinted hydrogels. Published online 2020. DOI:10.1093/burnst/tkaa029
19. Massaro M, Lazzara G, Milioto S, Noto R, Riela S. Covalently modified halloysite clay nanotubes: synthesis, properties, biological and medical applications. Published online 2017. DOI:10.1039/c7tb00316a

20. Luo Y, Mills D. The Effect of halloysite addition on the material properties of chitosan-halloysite hydrogel composites. Published online 2019. DOI:10.3390/gels5030040
21. Jammalamadaka U, Tappa K, Weisman J, Nicholson J, Mills D. Effect of barium-coated halloysite nanotube addition on the cytocompatibility, mechanical and contrast properties of poly(Methyl methacrylate) cement. Published online 2017. DOI:10.2147/NSA.S131412
22. Ou Q, Huang K, Fu C. Nanosilver-incorporated halloysite nanotubes/gelatin methacrylate hybrid hydrogel with osteoimmunomodulatory and antibacterial activity for bone regeneration. Published online 2019. DOI:10.1016/j.cej.2019.123019
23. Duan L, Zhao Q, Liu J, Zhang Y. Antibacterial behavior of halloysite nanotubes decorated with copper nanoparticles in a novel mixed matrix membrane for water purification. Published online 2015. DOI:10.1039/c5ew00140d
24. Marchesan S, Qu Y, Waddington LJ. Self-assembly of ciprofloxacin and a tripeptide into an antimicrobial nanostructured hydrogel. Published online 2013. DOI:10.1016/j.biomaterials.2013.01.096
25. Mathews S, Hans M, Mücklich F, Solioz M. Contact killing of bacteria on copper is suppressed if bacterial-metal contact is prevented and is induced on iron by copper ions. Published online 2013. DOI:10.1128/AEM.03608-12
26. Andersen T, Auk-Emblem P, Dornish M. 3D cell culture in alginate hydrogels. Published online 2015. DOI:10.3390/microarrays4020133
27. Kim H, Bae C, Kook Y, Koh W, Lee K, Park M. Mesenchymal stem cell 3D encapsulation technologies for biomimetic microenvironment in tissue regeneration. Published online 2019. DOI:10.1186/s13287-018-1130-8
28. Stratton S, Shelke N, Hoshino K, Rudraiah S, Kumbar SG. Bioactive polymeric scaffolds for tissue engineering. Published online 2016. DOI:10.1016/j.bioactmat.2016.11.001
29. Horiguchi I, Sakai Y. Alginate encapsulation of pluripotent stem cells using a coaxial nozzle. Published online 2015. DOI:10.3791/52835

30. Lutolf M. Designing materials to direct stem cell fate. Published online 2011. DOI:10.1038/nature08602.Designing
31. Xavier J, Thakur T, Desai P. Bioactive nanoengineered hydrogels for bone tissue engineering: A growth-factor-free approach. Published online 2015. DOI:10.1021/nn507488s
32. Leonhardt E, Kang N, Hamad M, Wooley K, Elsbahy M. Absorbable hemostatic hydrogels comprising composites of sacrificial templates and honeycomb-like nanofibrous mats of chitosan. Published online 2019. DOI:10.1038/s41467-019-10290-1
33. Higuchi A, Ling Q, Chang Y, Hsu S, Umezawa A. Physical cues of biomaterials guide stem cell differentiation fate. Published online 2013. DOI:10.1021/cr300426x
34. Wen J, Vincent L, Fuhrmann A. Interplay of matrix stiffness and protein tethering in stem cell differentiation. Published online 2014. DOI:10.1038/nmat4051
35. Gilbert P, Havenstrite K, Magnusson K, A Sacco, Lutolf M. Substrate elasticity regulates skeletal muscle stem cell self-renewal in culture. Published online 2011. DOI:10.1126/science.1191035.Substrate
36. Silva J, Burger B, Rodrigues H. Wound healing and omega-6 fatty acids: from inflammation to repair. Published online 2018. DOI:10.1155/2018/2503950
37. Janis J, Harrison B. Wound healing: part I. Published online 2016. DOI:10.1097/PRS.0000000000002773
38. Fathke C, Wilson L, Isik F. Contribution of bone marrow-derived cells to skin: collagen deposition and wound repair. Published online 2004. DOI: 10.1634/stemcells.22-5-812
39. Rodrigues M, Kosaric N, Bonham C, Gurtner G. Wound healing: A cellular perspective. Published online 2019. DOI:10.1152/physrev.00067.2017
40. Grover S, Mackman N. Tissue Factor: An essential mediator of hemostasis and trigger of thrombosis. Published online 2018. DOI:10.1161/ATVBAHA.117.309846

41. Flaumenhaft R, Sharda A. Platelet Secretion. Published online 2019. DOI:10.1016/B978-0-12-813456-6.00019-9
42. Yun S, Sim E, Goh R, Park J, Han J. Platelet activation: The mechanisms and potential biomarkers. Published online 2016. DOI:10.1155/2016/9060143
43. Offermanns S. Activation of platelet function through G protein-coupled receptors. Published online 2006. DOI:10.1161/01.RES.0000251742.71301.16
44. Foster C, Prosser D, Agans J. Molecular identification and characterization of the platelet ADP receptor targeted by thienopyridine antithrombotic drugs. Published online 2001. DOI:10.1172/JCI12242
45. Pickart L, Vasquez-Soltero J, Margolina A. GHK peptide as a natural modulator of multiple cellular pathways in skin regeneration. Published online 2015. DOI:10.1155/2015/648108
46. Lintner K, Peschard O. Biologically active peptides: From a laboratory bench curiosity to a functional skin care product. Published online 2000. DOI:10.1046/j.1467-2494.2000.00010.x
47. Wang X, Liu B, Xu Q. GHK-Cu-liposomes accelerate scald wound healing in mice by promoting cell proliferation and angiogenesis. Published online 2017. DOI:10.1111/wrr.12520
48. Pickart L, Margolina A. Regenerative and protective actions of the GHK-Cu peptide in the light of the new gene data. Published online 2018. DOI:10.3390/ijms19071987
49. Zoughaib M, Luong D, Garifullin R, Gatina D, Fedosimova S, Abdullin T. Enhanced angiogenic effects of RGD, GHK peptides and copper (II) compositions in synthetic cryogel ECM model. Published online 2021. DOI:10.1016/j.msec.2020.111660
50. Van Rooijen M, Mensink R. Palmitic acid versus stearic acid: Effects of interesterification and intakes on cardiometabolic risk markers-a systematic review. Published online 2020. DOI:10.3390/nu12030615
51. Lee J, Lee C, Kim I. Preparation and evaluation of palmitic acid-conjugated exendin-4 with delayed absorption and prolonged circulation for longer hypoglycemia. Published online 2012. DOI:10.1016/j.ijpharm.2011.12.050

52. Irby D, Du C, Li F. Lipid-drug conjugate for enhancing drug delivery. Published online 2017. DOI:10.1021/acs.molpharmaceut.6b01027
53. Williams E, Harris P, Jamaluddin M, Loomes K, Hay D, Brimble M. Solid-phase thiol-ene lipidation of peptides for the synthesis of a potent CGRP receptor antagonist. Published online 2018. DOI:10.1002/anie.201805208
54. Pires D, Bemquerer M, Nascimento C. Some mechanistic aspects on Fmoc solid phase peptide synthesis. Published online 2014. DOI:10.1007/s10989-013-93668
55. Zhang L, Bulaj G. Converting peptides into drug leads by lipidation. Published online 2012. DOI:10.2174/092986712799945003
56. Yang G, Sau C, Lai W, Cichon J, Li W. Protein lipidation: Occurrence, mechanisms, biological functions, and enabling technologies. Published online 2018. DOI: 10.1021/acs.chemrev.6b00750
57. Yousefi-Salakdeh E, Johansson J, Strömberg R. A method for S- and O-palmitoylation of peptides: Synthesis of pulmonary surfactant protein-C models. Published online 1999. DOI:10.1042/0264-6021:3430557
58. Jeschke M, van Baar M, Logsetty S. Burn injury. Published online 2020. DOI:10.1038/s41572-020-0145-5
59. Kheirabadi B, Scherer M, Estep J, Dubick M, Holcomb J. Determination of efficacy of new hemostatic dressings in a model of extremity arterial hemorrhage in swine. Published online 2009. DOI:10.1097/TA.0b013e3181ac0c99
60. Cripps M, Cornelius C, Nakonezny P. In vitro effects of a kaolin-coated hemostatic dressing on anticoagulated blood. Published online 2018. DOI:10.1097/TA.0000000000001999
61. Trabattoni D, Montorsi P, Bartorelli A. A new kaolin-based hemostatic bandage compared with manual compression for bleeding control after percutaneous coronary procedures. Published online 2011. DOI:10.1007/s00330-011-2117-3
62. Satish S, Tharmavaram M, Rawtani D. Halloysite nanotubes as a nature's boon for biomedical applications. Published online 2019. DOI:10.1177/1849543519863625

63. Keyes BE, Liu S, Asare A. Repair in Aged Skin. Published online 2017. DOI:10.1016/j.cell.2016.10.052.Impaired
64. Basuki K. Principles of bone biology. Vol 53. Published online 2019. DOI:www.journal.uta45jakarta.ac.id
65. Su P, Tian Y, Yang C. Mesenchymal stem cell migration during bone formation and bone diseases therapy. Published online 2018. DOI:10.3390/ijms19082343
66. Schlickewei C, Kleinertz H, Thiesen D. Current and future concepts for the treatment of impaired fracture healing. Published online 2019. DOI:10.3390/ijms20225805
67. Yang F, Yang D, Tu J, Wang L. Strontium enhances osteogenic differentiation of mesenchymal stem cells and in vivo bone formation by activating Wnt/catenin signaling. Published online 2011. DOI:10.1002/stem.646
68. Schlesinger P, Blair H, Stolz D. Cellular and extracellular matrix of bone, with principles of synthesis and dependency of mineral deposition on cell membrane transport. Published online 2020. DOI:10.1152/ajpcell.00120.2019
69. Kawane T, Qin X, Jiang Q. Runx2 is required for the proliferation of osteoblast progenitors and induces proliferation by regulating Fgfr2 and Fgfr3. Published online 2018. DOI:10.1038/s41598-018-31853-0
70. Komori T. Regulation of proliferation, differentiation and functions of osteoblasts by runx2. Published online 2019. DOI:10.3390/ijms20071694
71. Bi H, Chen X, Gao S. Key triggers of osteoclast-related diseases and available strategies for targeted therapies. Published online 2017. DOI:10.3389/fmed.2017.00234
72. Blair H, Larrouture Q. Osteoblast differentiation and bone matrix formation. Published online 2017. DOI:10.1089/ten.teb.2016.0454
73. Wang R, Green J, Wang Z. Bone morphogenetic protein (BMP) signaling in development and human diseases. Published online 2014. DOI:10.1016/j.gendis.2014.07.005
74. Jain A, Pundir S, Sharma A. Bone morphogenetic proteins: the anomalous molecules. Published online 2013. DOI:10.4103/0972-124X.119275

75. Kollias H, McDermott J. Transforming growth factor- $\beta$  and myostatin signaling in skeletal muscle. Published online 2008. DOI:10.1152/japplphysiol.01091.2007
76. Winnier G, Blessing M, Labosky P, Hogan B. Bone morphogenetic protein-4 is required for mesoderm formation and patterning in the mouse. Published online DOI:10.1101/gad.9.17.2105
77. Monzen K, Hiroi Y, Kudoh S. Smads, TAK1, and their common target ATF-2 play a critical role in cardiomyocyte differentiation. Published online 2001. DOI:10.1083/jcb.153.4.687
78. Heu R, Shahbazmohamadi S, Yorston J, Capeder P. Target Material Selection for Sputter Coating of SEM Samples. Published online 2019. DOI:10.1017/s1551929519000610
79. Staaks D, Olynick D, Rangelow I, Altoe M. Polymer-metal coating for high contrast SEM cross sections at the deep nanoscale. Published online 2018. DOI:10.1039/c8nr06669h
80. Geris L, Gerisch A, Sloten J. Angiogenesis in bone fracture healing: A bioregulatory model. Published online 2008. DOI:10.1016/j.jtbi.2007.11.008
81. Canalis E, Zanotti S. Hajdu-Cheney syndrome: a review. Published online 2014. DOI:10.1186/s13023-014-0200-y
82. Zheng C, Yang Q, Cao J. Local proliferation initiates macrophage accumulation in adipose tissue during obesity. Published online 2016. DOI:10.1038/cddis.2016.54
83. Zeng J, Zhang Y, Hao J. Stearic acid induces CD11c expression in proinflammatory macrophages via epidermal fatty acid binding protein. *J Immunol*. Published online 2018. DOI:10.4049/jimmunol.1701416
84. Lattouf R, Younes R, Lutomski D. Picosirius Red Staining: A Useful Tool to Appraise Collagen Networks in Normal and Pathological Tissues. Published online 2014. DOI:10.1369/0022155414545787
85. Neves M, Moroni L, Barrias C. Modulating alginate hydrogels for improved biological performance as cellular 3D microenvironments. Published online 2020. DOI:10.3389/fbioe.2020.00665

86. Borazjani N, Tabarsa M, You S, Rezaei M. Effects of extraction methods on molecular characteristics, antioxidant properties and immunomodulation of alginates from *Sargassum angustifolium*. Published online 2017.  
DOI:10.1016/j.ijbiomac.2017.03.128
  
87. Han Y, Li Y, Zeng Q. Injectable bioactive akermanite/alginate composite hydrogels for: In situ skin tissue engineering. Published online 2017.  
DOI:10.1039/c7tb00571g